Spatially offset Raman spectroscopy: from instrumentation to applications in monitoring bone regeneration.

Submitted March 2021, in partial fulfillment of
the conditions for the award of the degree **PhD in Physics.**

Max Jordan Dooley

4271771

Supervised by Prof Ioan Notingher

School of Physics and
Astronomy University of
Nottingham

I hereby declare that this Thesis is all my own work, except as indicated in the text:

Signature: Max Dooley

Date 27 / 03 / 2021

I hereby declare that I have all necessary rights and consents to publicly distribute this dissertation via the University of Nottingham's e-dissertation archive.

Abstract

Spatially offset Raman spectroscopy (SORS) is a method for measuring Raman signal from much deeper within a sample than is achievable with traditional Raman spectroscopy, and relies on the diffuse scattering of photons within turbid materials. This makes SORS a promising tool in the field of medical imaging.

A SORS device was built, based around a digital micro mirror device. This allowed for the detection offset to be selected in software and gave the SORS device a huge flexibility. The instrument was then applied to the study of bone regeneration.

Using phantom samples, we investigated the feasibility of using SORS as a tool for monitoring non-invasively the mineralization of bone tissue engineering scaffold *in vivo*. The phantom samples consisted of 3D-printed scaffolds of poly-caprolactone (PCL) and hydroxyapatite (HA) blends, with varying concentrations of HA, to mimic the mineralisation process. The scaffolds were covered by a 4 mm layer of skin to simulate real *in vivo* measurement conditions. At a concentration of HA approximately 1/3 that of bone (~0.6 g/cm^3), the characteristic Raman band of HA (960 cm^{-1}) was detectable when the PCL:HA layer was located at 14 mm depth within the scaffold (i.e. 8 mm below the skin surface), and concentrations of ~10% of bone were detectable at 4 mm depth.

We then investigated the feasibility of using SORS to monitor changes in collagen concentration at levels similar to those expected to occur *in vivo* during bone regeneration (0 – 0.84 g/cm^3). A partial least squares (PLS) regression model was developed to quantify collagen concentration in plugs consisting of mixtures of collagen and hydroxyapatite (predictive power of ±0.16 g/cm^3). The PLS model was then applied to SORS spectra acquired from rat cadavers after implanting the collagen:hydroxyapatite plugs in drilled skull defects. The PLS model successfully predicted the profile of collagen concentration, but with an increased predictive error of ±0.30 g/cm^3. These results demonstrate the potential of SORS to quantify collagen concentrations in the range relevant to those occurring during new bone formation.

List of publications

- **Dooley, M**., Prasopthum, A., Liao, Z., Sinjab, F., McLaren, J., Rose, F.R., Yang, J. and Notingher, I.
  Spatially offset Raman spectroscopy for monitoring mineralization of bone tissue engineering scaffolds: feasibility study based on phantom samples.
  Biomedical optics express, *10*(4), pp.1678-1690. 2019.

- Sinjab, F., Elsheikha, H.M., **Dooley, M**. and Notingher, I.
  Induction and measurement of the early stage of a host-parasite interaction using a combined optical trapping and Raman microspectroscopy system. *Journal of Biophotonics*, *13*(2), p.e201960065. 2020.

- **Dooley, M.,** McLaren, J., Rose, F.R. and Notingher, I.
  Investigating the feasibility of spatially offset Raman spectroscopy for in-vivo monitoring of bone healing in rat calvarial defect models. *Journal of Biophotonics*, *13*(10), p.e202000190. 2020.

Acknowledgements

Firstly, I would like to thank my supervisor, without whose support I would not have been able to finish my PhD. Furthermore, without his guidance and trust, I believe that I would not have been able to become as independent a researcher as I have. His guidance has been useful, not only in the realms of physics, but also in teaching me the underlying principles that make one a good scientist.

Thanks must go to the biophotonics group at Nottingham in general, including Faris and Zhiyu, for teaching me the basics of Raman spectroscopy, and Nathan and Chris, for being there to discuss science when I had ideas that I could not quite form into coherent constructs. The group has been a great thing to be part of and I am very grateful to have such good friends.

Of course, no acknowledgement, would be complete without me thanking my wonderful girlfriend, Tasha, who has supported me through the last four years. She has always been willing to help me, both in terms of supporting the writing, and in being willing to traipse across the world with me to conferences to support my presentations. She is always willing to listen and show interest in my ideas.

Finally, thanks should go to my parents who have always been there to encourage my interest in science from a very young age and continue to encourage me even now. Both have spent an inordinate amount of physical and emotional energy in helping me get my thesis completed and I could not be more grateful for their unwavering belief that I would get it done, eventually.

Contents

vi

1 Chapter 1

Introduction

1.1 Aims

The main aim is to develop a Raman spectroscopy technique that will allow for monitoring of the molecular processes of bone regeneration. This will be achieved by spatial offset Raman spectroscopy (SORS) utilising a digital micro-mirror device (DMD) array to change dynamically the geometry of the detection patterns. Through this flexible approach to SORS I will show that diffuse Raman spectroscopy can be developed into a powerful tool for monitoring biological systems such as bone growth and healing.

1.2 Context

1.2.1 Bone damage: An introduction

Imaging of bone damage and monitoring of healing is a huge global medical challenge. Bone fractures occur at a rate of 3.6% of the population per year (1) and can have a huge range of causes from sports injuries (2), road traffic accidents (3), osteoporosis (2), (4), and many other factors (2), (5), (6). This leads to a large amount of research being devoted to the subject from a large number of fields; from osteopaths investigating the causes of bone degradation (7), (8) and surgeons focused on direct patient intervention (9), (10), to engineers looking for biomechanical solutions such as 3D scaffolds to replace bone grafts (11), (12).

Beyond direct interaction with bone fracture patients, there is a large body of research being directed towards investigating both healthy and damaged bone, and bone growth patterns. Damage to bone with different shapes such as a skull plate or the main stretch of a femur can follow different healing patterns (13) and as such, a number of different models have been created for different bone healing pathways focusing on the factors within bone growth. Some damage is small enough and can heal fully without intervention (10) while some types of larger damage can be fixed with external assistance such as a cast (14). In situations where the damage is so great that it

has generated a defect in the bone so large it will not heal on its own, the defect is called a critical defect (15).

The exact size of a critical defect is dependent on the size of the bone (16), the age of the person (17), and other medical conditions such as the presence of osteoporosis (18). Depending on the bone containing the defect it can lead to structural weakness or a complete lack of healing altogether (15) (16).

1.2.2 Determinants of bone strength and successful bone-growth

In understanding bone growth and health, it is important to understand the different factors that influence bone strength. Healthy bone is roughly 65% mineral, most of which is hydroxyapatite (19). the remainder of the structure of bone is made up of soft tissue, predominantly collagen. A key factor that affects strength in any bone is the degree of mineralization (19). Follet *et al* found a strong correlation between the apparent Young's modulus (a measure of the strength of bone) and the degree of mineralisation (R^2 = 0.44, $p < 0.003$) and maximal strength and degree of mineralisation (R-squared = 0.41, $p < 0.003$) in cancellous bone (Figure 1.1) (19).
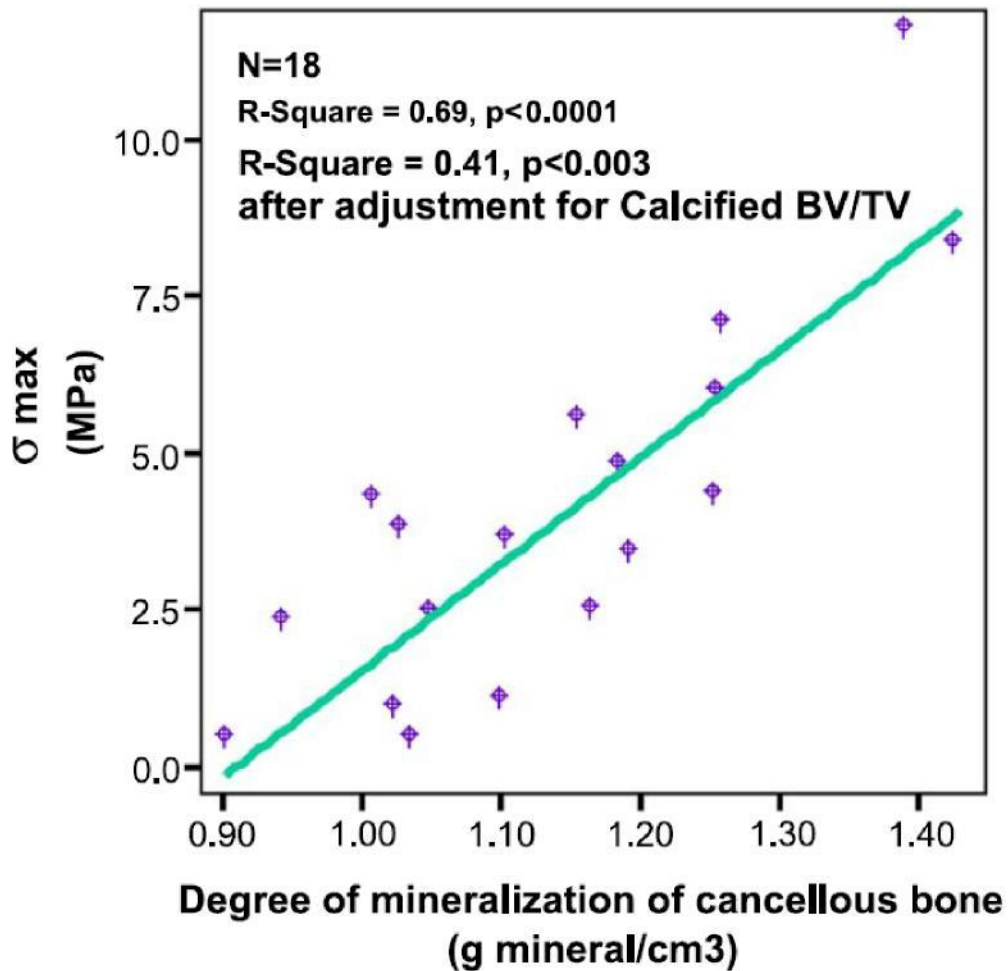
Figure 1.1 The strength of bone against the degree of mineralisation of cancellous bone (19). The compressive test was performed in the main trabecular direction by a 5000-N load cell.

Bone density and bone mineralization are highly correlated as mineral makes up the most massive part of bone. For this reason, it is not surprising that bone density is also highly correlated with bone strength (20). These two properties are so highly connected that the measurement of one can act as a proxy for the measurement of the other. In a porcine bone study (21) bone with a density that was 1.7 g/cm^3 was found to be > 75% organic based while in bone that had reached a density of 2.0 g/cm^3 or greater the collagen was found to be 35% as is expected for mature bone. This indicates that after the first growth of collagen in the early stages of bone defect healing the amount of collagen drops as the mineral density increases, this phase of bone growth is known as remodeling (21).

Different types of bone have different strength that do not always follow the pattern of increasing mineralisation leading to increasing strength. The orientation of collagen fibers

also has a large effect on bone strength, along with other variables. While comparing plexiform and osteonal bone, Martin *et al* found that even though the mineralisation did not vary significantly between the two bone types, plexiform was significantly stronger (22). The authors found that the longitudinal structure index (LSI), or the amount of collagen fibers that were aligned with the long axis of the bone, was the best single predictor of strength between the bone types. For any given bone type, LSI and increases in mineralisation still gave a strong correlation with bone strength. For this reason, the detection of collagen formation and the structure of the extracellular matrix are also highly important in monitoring the health and strength of newly formed bone.

1.2.3   Current state of bone imaging

1.2.3.1   XRAY imaging.

Traditional x-ray imaging is used to image the mineral components of the bone. Beyond this, x-rays also have a well-demonstrated danger both to the patient and the clinical practitioner due to the fact that x-rays are ionizing radiation. Prolonged exposure to x-rays can lead to cellular death and increases the risk factor for certain cancers.
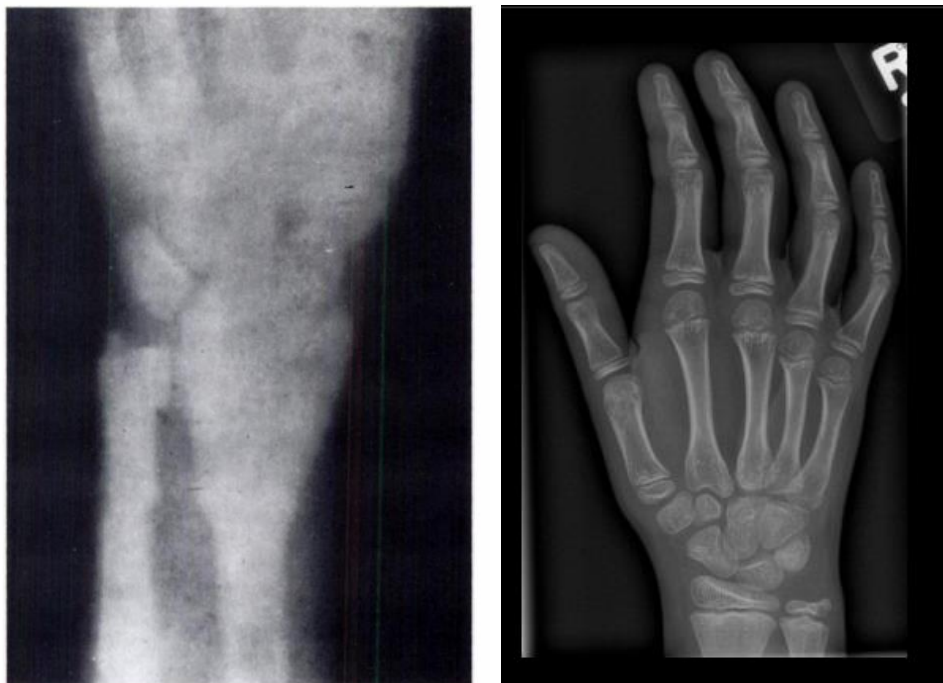

Figure 1.2 left, the first x-ray image acquired in America (23). Right, a modern x-ray image [Case courtesy of Kellie Grant, Radiopaedia.org, rID: 40336]

X-ray imaging in its simplest form uses the attenuation of photons of energy 20 Kev to 140 Kev (24) (25) through the body. Due to the low attenuation coefficients of soft

materials in the human body, such as adipose tissue or skin, x-rays pass through these parts with minimal interaction. When x-rays hit bone however, the attenuation coefficient is much higher, and the light is scattered and absorbed more. Given the straight path of non-scattered light this means a photo-reactive plate behind the sample will detect x-rays where there is soft tissue and greatly reduced or no x-rays where there is bone or other lesions of high attenuation. Figure 1.2 presents two x-ray images, with each showing a much greater amount attenuation of the signal in the areas where there is bone rather than soft tissue. The x-ray image on the left, which is the first instance of an x-ray image in America, took minutes to complete and there is clear evidence of movement causing blurring. The modern x-ray image shows that where the x-rays pass through more dense bone, such as the edge of the finger bones, there is more attenuation.

A limitation of this form of imaging is that, in terms of attenuation of signal, there is no difference between a thick area of low attenuation and thin areas of high attenuation. With only a single direction of the x-rays, there is little to no depth information within the signal generated. This limits the interpretative power of the method.

Contrast x-ray imaging can be used to target some parts of the human body, such as barium swallow (26), or intravenous urogram (27). Both involve taking in some form a material that attenuates the x-rays more strongly than normal soft tissue. The areas in which the contrast agents accumulate are then highlighted in comparison to the rest of the body. It is important to note that it is the contrast agents themselves that are imaged in this case and not the soft tissue the material has accumulated in.

As mentioned, x-ray radiation has a large health risk to those who use them regularly. Ionising radiation can lead to complications in the human body, the most common being cancer risk. A number of studies have shown increased cancer risks associated with x-ray screening. A 2006 study showed x-ray exposure associated with lung cancer screening cased a potentially fatal cancer rate of 0.11 per thousand (28), and a study on prenatal x-ray screening showed an 80% increase in the risk of childhood cancers (29). The risk to staff carrying out the procedure is also high with stringent safety protocols in place in medical faculties across the world (30).

The combination of these problems limits the usefulness for x-ray imaging as a method for time-course studies into bone growth and healing. Repeated exposure to x-rays increases the dose and therefore the risk to the patient or animal in which the bone healing is occurring. It also has limited ability to differentiate between soft tissues which make up as much as 35% of healthy bone (21).

1.2.3.2 Computed tomography scan (CT scan)

To overcome some of the pitfalls of conventional x-ray imaging and turn a 2D imaging technique into a 3D technique computed tomography (CT) was developed. A larger number of x-ray images are taken from different angles which allows a computer to build up a three-dimensional image of mass, manipulated and rendered using standard tomographic imaging algorithms. Figure 1.3 shows three different slices of the same wrist structure created using a CT scan. Compared to the two-dimensional views in Section 1.2.3.1 we can see much more information is valuable to the clinician.

Figure 1.3 A CT scan of a wrist, A is axial view, B is the coronal plane, and C is the sagittal plane (31).

With this increased information comes a cost as CT increases the number of exposures to x-ray radiation. A standard chest x-ray image requires 0.05-0.24 mSv, whereas a chest CT scan exposes the patient to 4.0-18 mSv (32). This significantly increases the risks to the patient due to exposure, though the dose is still low enough for the process to be considered safe.

CT scans are often used at the end of a study to determine the success of a given protocol. The use of micro-CT to measure the distribution of mineral deposits in excised bone defects has been shown to be an invaluable tool to post-study data acquisition (33) (34). The advantage of using CT at this stage in the study is that there is no longer living tissue that can be damaged by the radiation exposure.

The increase in radiation exposure reduces the usefulness of CT for ongoing time-course studies in living models. The increased risk of CT combined with the multiple measurements needed to monitor growth across the course of a study would lead to a dangerous level of exposure. In the case of a time course study with one measurement a week for 10 weeks the exposure could reach 180 mSv. 100 mSv is considered the lowest level at which an increase in cancer is evident (35). This shows that while CT scans can be powerful tools for determining the 3D nature of hard materials in the body, they have limitations within the realm of long-term studies. Despite the strength of CT scans as a method for monitoring hard minerals the method is much more limited with regards to soft tissue.

1.2.3.3 Dual-energy x-ray absorptiometry (DXA)
Dual-energy x-ray absorptiometry (DXA) is a variant of x-ray imaging that extends the information acquired by using two x-ray beams with different energies (36). The different x-ray wavelengths have different absorption coefficients in the materials. It is most used in bone density measurements where the ratio of absorption also changes between different materials (37). With the known values for bone and soft tissue it is possible to subtract the absorption from the soft tissue surrounding the bone. By isolating the bone attenuation, a calculation can be made, based on the size of the

bone and the light attenuated, and a value for the density of the bone material determined (36).
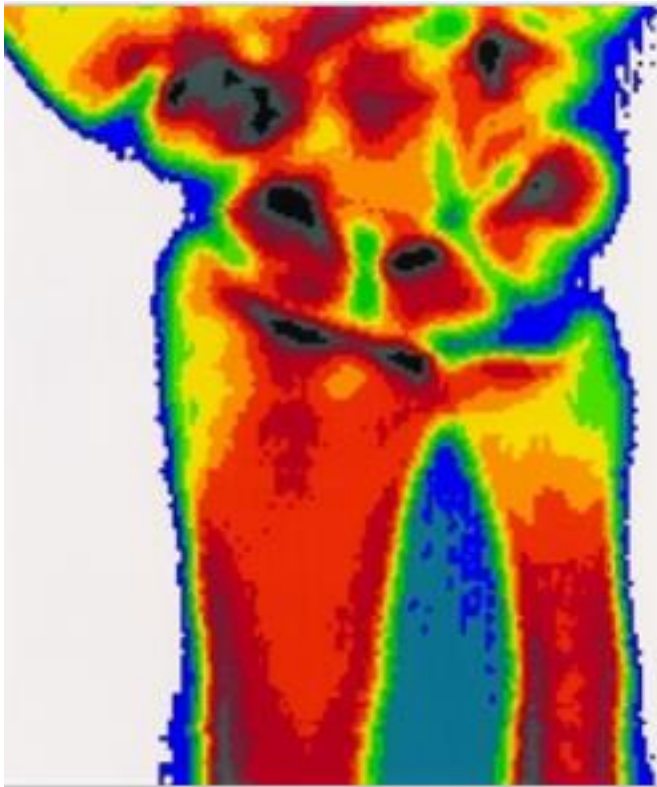
Figure 1.4 A DXA scan of a normal right wrist with a heat map denoting density with blue being the lowest density and black being the highest (38).

DXA creates a two-dimensional map of the body much as in x-ray imaging. The two-dimensional nature of the image means that the thickness of the bone needs to be estimated based on its width and other spatial factors. Attenuation is dependent on two factors, thickness, and mineral density. The fact that DXA estimates material thickness based on spatial clues from the image means that there in inherent error in the prediction of mineral density. Spatial clues can be the values such as the width of the bone which can be used to infer a thickness based on knowledge of average bone size and shape. This relies on the images bone being within the normal limits of shape, which given that DXA may be used in a medical situation on pathological bone this is not always a good assumption. This limitation reduces the accuracy of DXA, particularly in situations with bones that do not conform to the patterns that is used to predict their thickness.

The benefit of DXA over other x-ray-based techniques is the reduced exposure with the range from 0.001-0.035 mSv compared to a chest x-ray which is greater than 0.05 mSv (39). The reduced exposure means that DXA may have some capacity to measure the growth of bone minerals within a defect. The use of DXA would not however be optimal for early detection of a defect that was enclosed, such as a hole that has been bored out of a bone, since the two-dimensional nature of the scan does not allow for the distribution of the growth *within* the defect to me mapped effectively. Figure 1.4 shows two dimensional images similar to those in Figure 1.2 showing good contrast between the soft tissue and mineral as well as clear contrast between more and less dense bone structures.

1.2.3.4 *Magnetic resonance imaging*

Magnetic resonance imaging (MRI) is a non-invasive 3D imaging technique that has been used to image bone as well as other soft tissues (40). The basis of MRI involves the application of a field gradient and strong magnetic fields across the imaged material and detecting of the flipping spins of nuclei in the material. The relaxation time of the flip is used as a means of differentiating materials. MRI in medical usage focuses of the flip of the hydrogen nuclei (40). Water contained in the cells of the human body as well as any fat or protein contains a large quantity of hydrogen, so the imaging typically maps the soft tissues of the human body much more effectively than x-ray imaging or any of its derivatives. MRI has been shown to be able to predict strongly the density of bone by measuring proton density (40). Figure 1.5 shows a clear contrast between mineralised bone and the surrounding soft tissue.
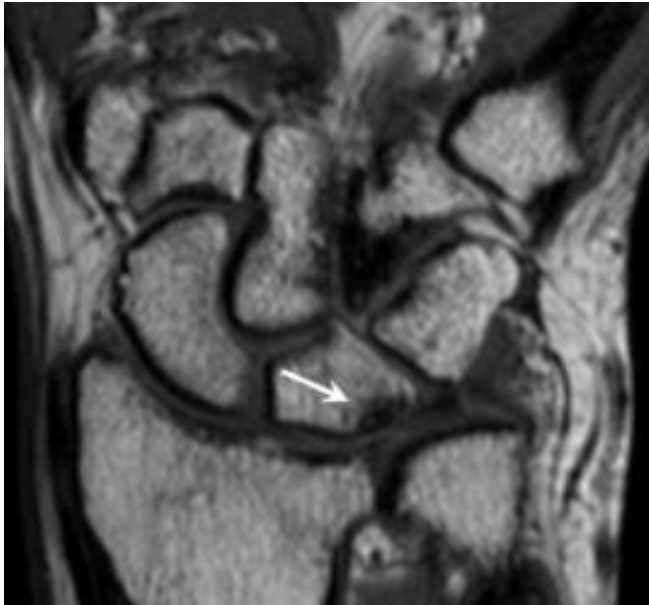
Figure 1.5 An MRI image of a wrist was taken to investigate ulnocarpal impaction syndrome. The arrow pointing to the damaged part of the bone (41)

The use of magnetic fields and radio waves has a major advantage over x-ray imaging in that there is no dangerous ionising radiation (41). For the vast majority of patients or test subjects this is much safer than x-ray imaging and there is not an upper bound of the number of 'exposures' that would be safe. In some cases, such as with metal structures in bone defects, the high magnetic fields will preclude the use of MRI. Since metal inserts are common in studies investigating critical defect (to hold the bone in place during the early stages of bone healing) MRI may have limited use in these studies. Measurements can take in excess of an hour to complete so there is a considerable constraint on the throughput that a single MRI machine can manage. In the case of an animal model this means sedation and increases the cost as well as potential danger to the animal. In a large study with tens of participants requiring daily or highly frequent imaging this slow imaging time can limit the throughput of the study. CT is much faster, with scans acquired within minutes.

1.2.3.5   Limitations of current techniques

As described above, current methods for bone imaging are powerful and well developed. The main focus of progress in these areas has been towards improving patient safety and expanding possible medical applications. While in most of these areas they fulfil their roles well, x-ray imaging methods are limited in application due to risk of high exposure to patient and operator, and MRI is expensive and slower, though

much safer. Diffuse Raman spectroscopy offers the capacity to obtain fast, time dependent molecular information which is a step-change above current technology (diffuse Raman spectroscopy can be undertaken in one or two minutes).

Spatially offset Raman spectroscopy (SORS) as part of the field of diffuse Raman spectroscopy gives the opportunity to create a mode of detection using photon scattering Raman spectroscopy to build three dimensional chemical maps of localised areas without using ionising radiation. This solution has the potential to be safer than x-ray based imaging due to the lack of ionising radiation, faster than MRI, and richer in molecular information.

Currently the major disadvantage of Raman spectroscopy is the very low signal strength and therefore signal to noise achievable. Raman signal is generated at a rate of $10^{-7}:1$ for every photon-molecule interaction. It is the goal of this thesis to improve significantly the signal to noise of SORS. It is also unclear as to how structural information such as absolute bone mineral density can be retrieve from SORS data.

1.3   Research protocols in bone healing research

1.3.1   Time course studies

1.3.1.1   Bone healing pathways

The bone healing process is a relatively slow biological process that takes months to reach its conclusion in large animals such as humans (42). A number of models of bone healing exist depending on the type of bone and amount of damage that has been caused (22). These show that bone growth happens in stages with different processes being central to each stage. There will therefore be different chemical signals that may be detectable at different stages. A simple model of bone healing in flat bones such as the skull is the four-phase model shown schematically in Figure 1.6. Phase one is inflammation around the damaged area, phase two and three are growth and hardening of soft tissue such as the collagen extracellular matrix. Phase four is the mineralisation and remodelling of the extracellular matrix (22) to form mineralised bone.
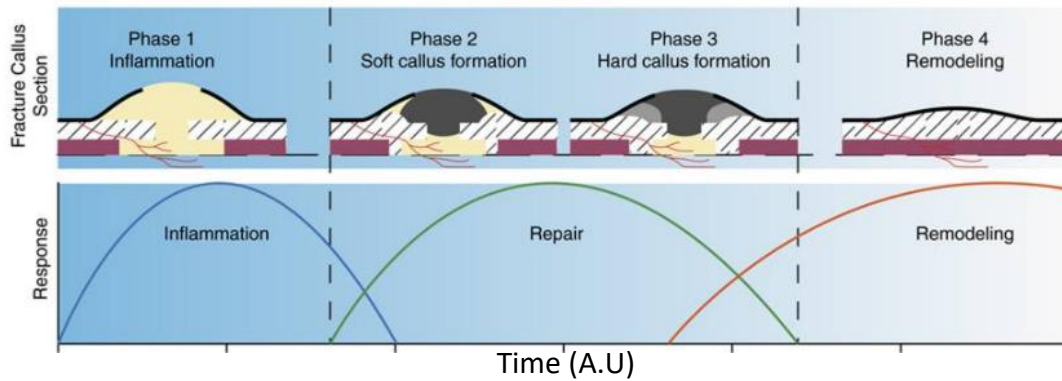
Figure 1.6 (top) A graphical representation of bone healing in the four-phase model. (bottom) shows the process that is happening during these phases. The x axis for both is time (22)

The main pathway of bone formation that is of interest to us is endochondral ossification, which is the pathway that happens in long bones. The first step is the formation of a cartilaginous region. This region is surrounded by bone. The cartilaginous region is then vascularised, and osteoblasts migrate into the tissue. The next step is mineralisation. Randomly oriented woven bone is laid down (this is also the process after bone is damaged). Slower growing lamellar bone replaces this bone. This bone is stronger and contains the osteons made of collagen fibres. Osteoblasts are responsible for much of the nucleation of the hydroxyapatite (HA) crystals and are situated on the surface where the mineralisation occurs, whereas the continued growth of the crystals is mediated by the extracellular matrix. Osteoblasts become trapped within the bone as the bone continues to grow and new layers of bone are laid down. After this, 90 – 95% of these cells differentiate to osteocytes. These new cells control important signalling pathways for absorption and other processes. Figure 1.7 shows the edge of mineralised bone as new bone is formed on top.
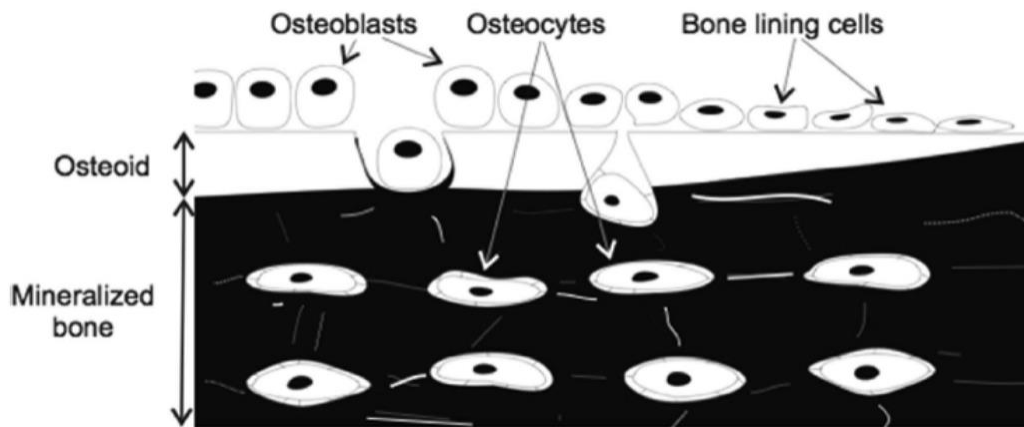
Figure 1.7 The top layer of cells are the osteoblasts formed on the top layer of the cartilage layers. Deeper in the mineralised bone the osteocytes are shown connected to each other. This shows how the osteoblasts end up inside the mineralised bone as bone growth propagates around them, first with the protein matrix, then the mineralisation of the matrix to follow.

The importance of these bone healing pathways is that they have clear phases where they will exhibit distinct chemical compositions, particularly before and after the mineralisation phase. This is the growth phase that is most easily detected by x-ray-based methods. This focus on mineralisation has its limitations, however. Mineralisation is not the only factor in bone strength and loss of, or damage to, the extracellular matrix can be just as important (43). These growth patterns show that early bone healing is based on the proliferation of soft tissue. Variations in concentrations of these soft materials are hard to be detected by x-ray imaging, particularly when surrounded by healthy bone. The early growth of these materials is crucial for bone health and the ability to detect it would lead to the ability to monitor early stages of bone healing to help detect earlier failures. The nature of bone growth shows that the ability to take repeated measurement of bone healing across a time course while monitoring a number of different materials would be hugely beneficial to the medical community.

1.3.1.2   *Imaging techniques as applied to bone growth and healing studies.*
Longitudinal studies that capture stage by stage bone grown and mineralisation are limited by current technology. A useful application of SORS would be to allow for monitoring healing processes at a molecular level, which would be hugely beneficial. Because of this several methods for investigating bone healing have arisen. In situations

where the experiment is expensive on a per-animal basis, such as with larger animal models (44) or in situations with complicated implants/grafts (45), it is common for the success of the study to be known only when the study is complete, and the animal can be killed. This is done to give the defect the best possible chance to heal to maximise the value of each component of the experiment and to not waste lives of animals needlessly. The problem with this method of study is that an animal must be kept for the full duration of a study even if the implant has failed from day one. While it often helps to separate interventions into successful/unsuccessful, it leaves much of the molecular processes of each time step of the healing process unexplored.

A second type of experimental set-up tries to remedy this shortcoming by stopping the experiment at a few different time points. These time points are often selected to span several critical stages of both growth and healing. This is more often done in small animal models where a larger batch size allows for more flexibility. In one study (46) for example a batch of 12 animals was used. Instead of all the animals being killed at the end, they can be killed in groups at different stages of expected growth. This gives a snapshot of different stages of healing and can produce a far more rounded understanding of the body's interactions with a certain intervention. This method still suffers from the need to kill the animal to measure the result. This snapshot model has the difficulty that you cannot show that the animals that ended the study after one week are representative of the bone growth in the remaining sample (44).

There have been some studies that utilise x-ray imaging for taking images at multiple stages throughout an experiment. This method addresses some of the shortcomings of the previous two methods and allows the researchers to monitor the healing progress of the defect to some extent, but with some caveats. As discussed earlier, x-ray imaging is only an image of the attenuation of x-rays in one plane. This means it is hard to differentiate between and change in mineralisation around the defect and healing causing increased density within the bone. There is also the limitation in that the growth of the extracellular matrix will have little effect on attenuation (47) of the defect, particularly in the case where a ceramic or other highly attenuating artificial scaffold was used. At the high photon energies used in x-ray imaging the HA minerals dominate the attenuation coefficient of a given volume of bone. This limits the use of

14

such techniques when it comes to measuring the soft tissue such as collagen, which will have its signal swamped by changes in concentration of HA. Extracellular matrix growth is the first major stage of bone healing, as it is this matrix through which the osteoblasts proliferate (48), and monitoring this would give early warning to the medical staff that a scaffold might be being rejected. There is also the problem that multiple x-ray exposure is not healthy, for the staff or subjects of the study.

1.3.1.3   Types of bone healing studies

There are several primary ways that bone healing intervention research is carried out. The first is as a study comparing outcomes in patients that have already been treated. These types of studies focus on methodologies that have already been cleared for use in humans and can help access which of the current methods lead to the best outcomes (49). Certain inventions are favoured more for specific conditions or by particular doctors which may have a systematic effect on the outcomes. This method of analysis is also limited to interventions that are already accepted practice amongst clinicians.

Animal studies are also performed where defects are deliberately created in order to monitor the direct effect of an intervention. In these cases, it is commonplace to compare the intervention case to a standard case, either using bone grafts (44) or an empty defect, comparing gold standard intervention or no intervention for reference. One clear problem with this approach is that, even with a good reference sample, it can be hard to separate bone growth that has been stimulated by the intervention as opposed to bone growth or healing that would have occurred within the defect naturally, the large variation in an individual's ability to heal even identical defects causing problems in comparing between animals. This means that being able to monitor growth within a defect as it happens is vital, rather than attempting to make inferences based of comparisons between samples from different time points. The osteoinductive, osteogenic, and osteoconductive properties cannot be easily separated for a given intervention when placed inside a healing defect (50). The surrounding bone contains all the cells and hormone needed, along with the signalling from the surrounding soft tissue which leads to an osteoinductive environment which can mask the osteoinductive signal, or lack thereof, of the implant.

To avoid this confounding of signal the implant can be tested not in a bone defect, but in a muscle pocket (51) or subcutaneously (52). This method of investigation focuses primarily on the osteoinductive signalling of an implant (53). For that reason, it is often performed on samples that have been populated with live cells from cultures or hormones to stimulate bone growth (54). Due to the lack of surrounding bone, there is no in-growth from the edge of the defect nor migration of precursor cells to initiate bone growth. This means that all mineralisation can be attributed to the osteoinductive properties of the implant. The levels of mineralisation are often much lower than when implanted in bone (52) so correct calibration is required to understand the relative effectiveness of different interventions. These implants can be excised at the end of the study without requiring animal sacrifice, and depending on the relative size of the implant and the animal, multiple implants can be made across a single specimen (51). As this method is more akin to an abnormal growth than true bone healing, time-course, or exploratory experiments into the nature of bone healing are not normally conducted in this manner, with the focus primarily on whether combinations of structures/chemical combinations can themselves induce bone growth.

1.3.2 The current state of bone healing research methodologies

There is a prevalence of time-course studies on both critical and non-critical defects in current research into bone healing, aiming to understand the temporal changes in bone during the whole process of bone healing. The majority of medical trials are in animals and these trials focus on the healing of a defect of a single size or shape, usually comparing some form of intervention to a standard. This standard can be either no intervention at all (10), a bone graft (55), or some other interventions such a printed scaffold (44). The defect is most often created at the start of a study often with a drill to ensure each animal model contains the same defect. The healing process requires living animals so ethical approval can be complicated.

1.3.2.1 Bone Graft

Bone grafts can be separated into two main categories, autograft, and allograft.

Autografts are bone grafts taken from the patient receiving the graft. The current gold standard in a clinical setting is an iliac crest bone graft (ICBG) (56). This requires a

surgical intervention to remove the graft from the iliac crest at the top of the hip bone as well as the surgical intervention to implant the graft. This can lead to morbidity within the iliac crest (56) in addition to other complications usually caused by surgical intervention. Success with this intervention has been 87-100% in mechanically stable environments (56). Another form of autograft is cortical bone graft. While the surgical intervention for this is somewhat simpler it runs its own risks (57). Cortical bone is much denser than that from the iliac crest which means it has reduced vascularity, which slows recovery. Autograft procedures are the only procedures that are osteogenic, osteoinductive, and osteoconductive. Osteogenic is the ability of an implant to generate new bone, and is limited to live cell transplants, such as autografts. An implant that is osteoinductive induces bone growth from already present bone growth mechanisms such precursor cells in the healthy bone surrounding a defect. On its own, an osteoinductive implant will not grow bone material. Osteoconductive materials offer technical support for bone growth and allow bone to grow through but do not act on the mechanisms of bone growth directly.

Allografts are grafts that are taken from another source other than the patient receiving the graft (58). This is often from cadavers, which leads to several complications. The first complication is the possibility of infection and this raises issues of pre-processing and storage. Bones can be fresh, frozen or freeze dried. A fresh graft is taken directly from a cadaver, processed to remove cells then implanted into the defect. This is rarely done due to the risk of disease transmission and immune response from the recipient. Frozen and freeze-dried grafts can be used more often, the storage process reduces the osteoinductive capabilities of the graft as many of the cells/hormones that would be present in living grafts have died or degraded. As such only the osteoconductive properties of the bone is preserved.

In research, both autograft and allograft procedures are conducted, often as a standard against which more innovative methodologies are compared (59) (60). These are methods with well understood biological responses and a track record in recovery for the patient. From a monitoring standpoint they can create some unique challenges. Mineral and soft tissue concentrations and distributions will be like that of a healed site from the start. While this is part of what makes these interventions so successful it

means monitoring the health of the graft from mineral density alone. This can limit the usefulness of traditional bone monitoring methods such as x-ray imaging which are dependent on attenuation.

1.3.2.2   Woven Collagen Fleece

Collagen fleece is a material that is produced from fibrous strands of collagen. It is porous and lightweight. When it is used, it is common to compare the fleece alone, against a number of fleeces doped with different growth surfactants, which are selected to increase the rate of healing, or, in the case of a critical defect, to help the defect to heal fully (61). The use of the collagen fleece is motivated by several factors. Firstly, the fleece is porous so can absorb a large amount of growth surfactant before being placed into the defect. The fleece is also malleable, particularly when wet and it easily conforms to the inside of the defect (61) (62). Finally, collagen fleece is broken down by the body so there is no lasting structure left behind once healing is completed.

1.3.2.3   Synthetic Structures

Many other materials have been tested in hopes of finding a structurally sound material that can replace bone grafts in large defects. Amongst these materials are plastics, ceramics, and hydrogels. Each of these have their benefits.

Plastics are pliable, resistant to the body's conditions and easily sterilised with heat or disinfectant without affecting the structure of the scaffold. In recent years, the explosion of additive manufacturing has made the goal of a truly bespoke scaffold designed for a defect an attainable future. 3D printing of materials such as polycaprolactone(PCL) gives the ability to quickly prototype different porosities and structural parameters of the defect before it is added to the defect model (63) (64). The printing method also allows for different materials to be added into the plastic directly, depending on their ability to mix in a plastic feed hopper. Materials such as hydroxyapatite (HA) can be printed directly into the lattice structure of the scaffold in varying concentrations (65).

Ceramics have been posited as a substitute for bone grafts due to their biocompatibility, often they are produced from calcium phosphates, a group which contains the bone mineral HA (66). They are also osteo-conductive, meaning bone can grow through them which gives them the ability, in theory, to support bone growth into

the defect. They are often also easily broken down by the body which can be both a benefit and a hindrance depending on the speed that his happens. Buckland *et al* (67) compared three common types of ceramic bone graft substitutes: dense calcium sulphate (DCaS), ultraporous tricalcium phosphate (beta-TCP), and porous silicated calcium phosphate (Si-CaP). DCaS was reabsorbed so quickly that it offered no real support for new bone growth. Both beta-TCP and Si-CaP supported bone growth, but the longer-term stability of Si-CaP gave it a greater supportive role to the proliferation of new bone material. This study showed that the rate at which the body absorbs the material of the scaffold is a key factor. Too slow and the defect will be left with the synthetic structure still inside, which can lead to structural weaknesses, and further complications depending on the material used (68). Fast absorption rates, however, cause two problems. The first is that bone growth is a relatively slow process, with studies even on small animals lasting many weeks (44), if the implant dissolves before significant restructuring of the defect can occur then it is unlikely to facilitate full healing. Another problem is that fast breakdown of scaffolds can cause many mineral/ceramic particles to be released into the area. Particles in high concentrations cause inflammation; excessive inflammation can reduce blood flow to an area and slow down or reverse the healing process (56).

1.3.3   SORS in bone imaging
1.3.3.1   *Spatial offset Raman spectroscopy in bone healing research*

In its current form, SORS offers the opportunity to monitor HA through scattering materials (69). In this thesis we extend this detection capacity to encompass other biologically relevant materials and form a basis for the prediction of concentration of materials in known areas. In chapters 4 and 5 we discuss our methods for bring SORS into line with what we see as a need in the regenerative medicine community for a quick, effective, and safe method for highly repeatable, non-destructive monitoring solutions to increase the productiveness of current research practices.

SORS has the capacity to monitor bone growth non-destructively and at a high frequency, possibly multiple times a day. Raman spectroscopy is non-ionising, and at

correct powers, non-damaging to tissue. This would allow for much more regular measurement of the defect region, effectively bringing the time between measurements down to as often as required. This has obvious benefits for the ethical use of animals in medical research as well as patient comfort. The ability of SORS to differentiate between materials on a chemical level allows for soft tissue growth to be monitored. This improvement over x-ray imaging without the increased cost of MRI means that studies of the early stages of bone healing such as the growth of the extracellular matrix and tissue inflammation could be conducted in vivo without the need for specimen sacrifice at each timepoint of interest. Being able to monitor the early stages of growth and comparing these stages in defects that had different levels of successful mineralisation would allow researchers to find patterns that are indicative of failure. By picking up failure early in the growth cycle these implants could be excised from defect and studied to find out more about how early failure occurs.

2   Chapter 2

Raman spectroscopy and diffuse optics

2.1   Raman spectroscopy

Raman spectroscopy is a method that uses the scattering interactions between a photon and a molecule to detect chemical species. Raman spectroscopy involves the excitation of a sample with a single wavelength of light. The shift in energy of these photons as they scatter from the material causes a quantised change in the wavelength which is measured as a spectrum. Raman measurements typically rely on the "fingerprint" region from 600 - 1800cm^{-1} as these are the wavelength changes that hold the most information about the chemical make-up of the sample.
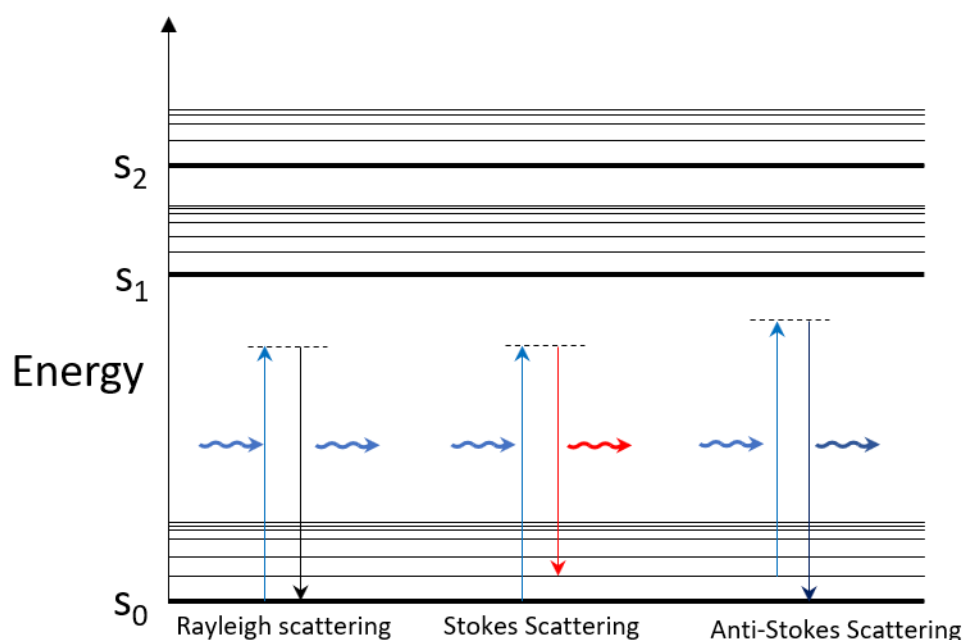
Figure 2.1 A schematic of Rayleigh, Stokes, and anti-Stoke scattering. S_0 denotes the ground energy state of the molecule. S_1 and S_2 denote excited electronic states. The dotted lines denote the virtual state that the photon excites the molecule to. Energy is not shown to scale. The horizontal wavy arrows indicate the photon before and after the scattering event.

2.1.1   Rayleigh scattering

Each time a photon scatters off a molecule there is a scattering event that is usually of the type called Rayleigh scattering (70). The elastic nature of the scattering means that no energy is lost or gained by the incident photon. The scattering can be modelled by

considering excitation of the molecule to a virtual energy state (71) followed by its return to its original level accompanied by the emission of a photon with wavelength equal to the wavelength of the excitation photon (Figure 2.1). A virtual energy state is a state that occurs for a very short period, in this case 10^{-12} s (72), which is unobservable. The lifetime and energy of these virtual bands is explained more fully in section 2.1.5.

2.1.2   Stokes Raman Scattering

Stokes scattering is the inelastic scattering of photons from molecules leading to a loss of energy and thus a longer wavelength (70). As can be seen from Figure 2.1 the same excitation photon as before causes the rise in energy to a virtual state as with Rayleigh scattering. In the case of Stokes scattering the energy state to which the molecule returns is higher than the original state (70). Energy states within a molecule are quantised, meaning that a molecule that is "Raman active" (see below) will have characteristic narrow bands describing the energy lost to different energy levels. It is these levels that gives the Raman spectrum of individual materials their wavenumber signature. This form of scattering happens approximately 10^{-7} times as much as Rayleigh scattering.

2.1.3   Anti-Stokes Raman scattering

In the anti-Stokes scattering case, the photon gains energy from its scattering event and the wavelength is shortened. Figure 2.1 shows that for this to happen the energy state of the molecule must start at an excited level. Because anti-Stokes Raman bands are much weaker than the Stokes bands, coherent anti-Stokes Raman spectroscopy is a common technique used for biological samples. This technique uses two light sources. The first is designated a pump laser (72)and has high power. The purpose of this laser is to saturate the probed area with monochromatic light to excite as many of the molecules as possible into a single excited state. The second laser has a much lower power and is the "Raman" laser, this laser generates fewer photons which scatter in the normal way, when they scatter off a molecule already excited by the pump laser the energy state rises to a higher state. When the molecule returns to a state below the pumped state the photon has more energy than before that scattering event (72). The fact that the pump laser is monochromatic means the excited states of most of the molecules will be identical, giving a unique fingerprint in the negative wavenumber shift region (72).
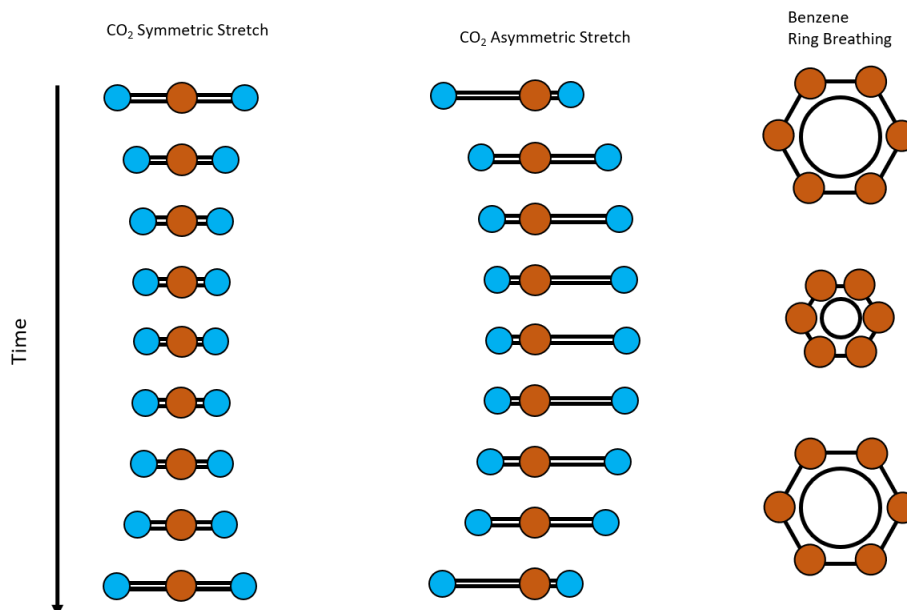
Figure 2.2 Symmetric and asymmetric stretch modes of carbon dioxide as well as the ring breathing vibrational mode in benzene rings. Red circles indicate carbon atoms and blue indicate oxygen atoms. The hydrogen is inferred. The diagram shows the full vibration cycle of a mode from start back to the same condition again.

2.1.4   Raman active vs inactive vibrational modes

In this context a vibrational mode of a molecule can be Raman active or inactive. This means that the bond will either generate a Raman band when excited by a photon or it will not, and this is dependent on the change in polarizability of the bond when excited.

Raman spectroscopy is an interaction between photons and molecular bonds. The selection criteria are based on the vibrational modes of the bonds within the molecule. A vibrational mode has both a polarizability and a dipole moment. A vibrational mode will be Raman active if the vibrational mode involves a change in polarizability (70). A change in dipole moment would give an IR spectroscopy signal. The difference between the two can be shown using two vibrational modes of CO_2. These are shown in the Figure 2.2.

For example, in the case of the symmetric stretch of CO_2 there is a change in polarizability between the extremes of vibrations as the bonds are shorter or longer at the same time. This means that the symmetric stretch of CO_2 is Raman active. The dipole moment however does change throughout the vibration, as it is a function of the distance between the centre of charges (73) and the symmetric movement of the oxygen maintains the centre of negative charge. This is an absorption inactive mode (70).

In the asymmetric stretch the centre of negative and positive charge oscillate in a way to causes a changing separation between them so the dipole moment changes causing the vibrational mode to be absorption active. The polarizability of the molecule has changed, however, as the bond length is the same at the end of each vibration. This vibrational mode would be Raman inactive. Not all vibrational modes fit neatly into one category with more complex vibrations being stronger in Raman or IR spectroscopy dependent on the degree of polarizability and dipole moment change that occurs.

If a molecule contains multiple bonds with the same configuration the signal for that mode will be increased, particularly in the case where the oscillation of the bonds is in phase. The most obvious demonstration of this is with the ring breathing mode at 1000 cm^{-1} wavenumbers for a benzene ring. As can be seen in Figure 2.2 a benzene ring contains six SP^2 bonds between the six carbons. The ring breathing mode is the simultaneous stretching and shortening of all six bonds in phase, this is part of why this peak is so strong relative to most other Raman peaks (74).

In general, the intensity of the Raman scattered light is given by:

$$I = KJ\alpha^2\omega^4 \qquad\qquad [2.1]$$

where α is the polarizability of the molecule, J is the laser power, ω is the frequency of the excitation light source, and K is a constant (71). From equation 2.1 we get that the intensity of the Raman signal is dependent on the fourth power of the frequency. Since in Raman spectroscopy we use wavelength to label our laser sources it follows that the intensity of our Raman signal will reduce with the fourth power of the wavelength (70):

$$I \approx \lambda^{-4} \qquad\qquad [2.2]$$

This has implications for the selection of laser wavelength when building as spectrometer as using a short wavelength will result in more absolute signal. It is important to balance this effect with other considerations. Photons with visible and IR wavelengths are safe, however, photons of sufficiently high energy become ionising radiation, such as x-rays. This means that in the case of biological materials, the higher energy photons of short wavelengths can cause cell damage even at low power. For this reason, it is not possible to just select the highest energy photons to maximise signal.

Longer wavelengths also improve the signal to fluorescence ratio in many of biological samples as many biological samples contain chemical compounds that fluoresce under green light. For this reason, it is common to see 785-1024 nm used in biological samples. Green, 532 nm, lasers are common where fluorescence is less of an issue, as this increases the Raman signal. Equation 2.1 shows that a more polarisable molecule will have a greater signal. Polarizability can be given by:

$$(\alpha_{\rho\sigma})_{GF} = k \sum_I \left(\frac{\langle F|r_\rho|I\rangle\langle I|r_\sigma|G\rangle}{\omega_{GI}-\omega_L-i\Gamma_I} + \frac{\langle I|r_\rho|G\rangle\langle F|r_\sigma|I\rangle}{\omega_{IF}+\omega_L-i\Gamma_I} \right)$$
[2.3]

where α is the molecular polarizability in the incident and scattering polarisation directions ρ and σ (71). Σ is the sum of all possible vibrionic states that can occur due to the photon scattering, and k is a constant, G is the ground state, I is an excited state, and F is the final state. r_σ is the dipole operator and the integral $\langle I|r_\sigma|G\rangle$ is the process of mixing the ground and the excited state. The left hand integral, $\langle F|r_\rho|I\rangle$, describes the scattering process from the excited state to the final state. These represent the mixing of the ground state with the excited state, then the excited state with the ground state. Since there is no reason that the mixing of states should start with the ground state the second set of integrals denotes the mixing of the excited states with the final state, and the initial state with the final state (71).

The components of the denominator of the first fraction are, ω_{GI} which denotes the energy difference between the ground and excited state, ω_L the energy of the laser, and ω_{IF} the energy difference between the final state and the excited state. In the first case the closer the energy state I is to the energy of the laser the greater the contribution it will have as $\omega_{GI} - \omega_L$ tends to 0. On the righthand side the denominator will always be much larger than $\omega_{GI} - \omega_L$ so the contribution from this will always be small. From this we see that an excited state will contribute proportionally more to the virtual state as its energy approaches the laser photon energy.

Due to the differences between the denominators the second set of integrals will have a much smaller effect on the polarizability that the first set of integrals. A state that is close to the virtual state will have a greater contribution to the polarizability than one that is further away, this is factored into the denominator as a constant $i\Gamma_I$. Since $i\Gamma_I$ is much less than ω_{GI} we can see it will have a far greater effect on the left side fraction than the right (71).

Another important equation describes the rate of Raman scattering:

$$I = \sigma' J N$$ [2.4]

where σ' is the Raman scattering cross section, J is the irradiating power in W/m^2, N is the number of irradiated molecules, and I is the Raman signal in watts per steradian. This shows two important dependencies for Raman spectroscopy (71). The intensity of Raman scattering is directly proportion to the number of molecules that are irradiated, and directly proportional the power of the excitation beam. The most important implication of this is: defocusing the beam to illuminate more of the surface does not increase signal from that surface as N and J both scale inversely to one another with the area of illumination as:

$$N = density \times area$$ [2.5]

Since laser damage is a real problem that limits the laser power density in a lot of applications this can directly limit the signal that can be generated and thus gathered by a Raman spectroscopy instrument (75). The direct relationship between number of molecules and signal strength also means that basic ratios between peaks heights can be used to determine the ratio of materials present in a sample.

2.1.5   Raman band Shape
2.1.5.1   Damped harmonic oscillator and Lorentzian peaks

The implication of quantised band energies is that each band should be a single wavelength. Spectral contain broader features that can be modelled more accurately as some combination of a Lorentzian and a Gaussian peak. The fundamental cause of this broadening is the "instantaneous" nature of the Raman interaction (76). The total time that the bond is in an excited state is approximately 10^{-12} s. Given the inherent uncertainty of quantum mechanical configurations this causes a broadening of the peal:

$$\Delta E_i \geq \hbar/\tau_i$$ [2.6]

where ΔE_i is the uncertainty in the energy band, τ_i is the mean time the bond is excited, and $\hbar$ is the reduced Planck's constant. The frequency of a photon is given by:

$$\omega = E/h$$ [2.7]

26

where ω is the frequency and E is the energy of that photon. The frequency of a photon a given Raman band is caused by the change in energy from the excited state to the lower state so the uncertainty of the frequency is:

$$\delta\omega = \Delta E_i/h = 2\pi/\tau_i \qquad [2.8]$$

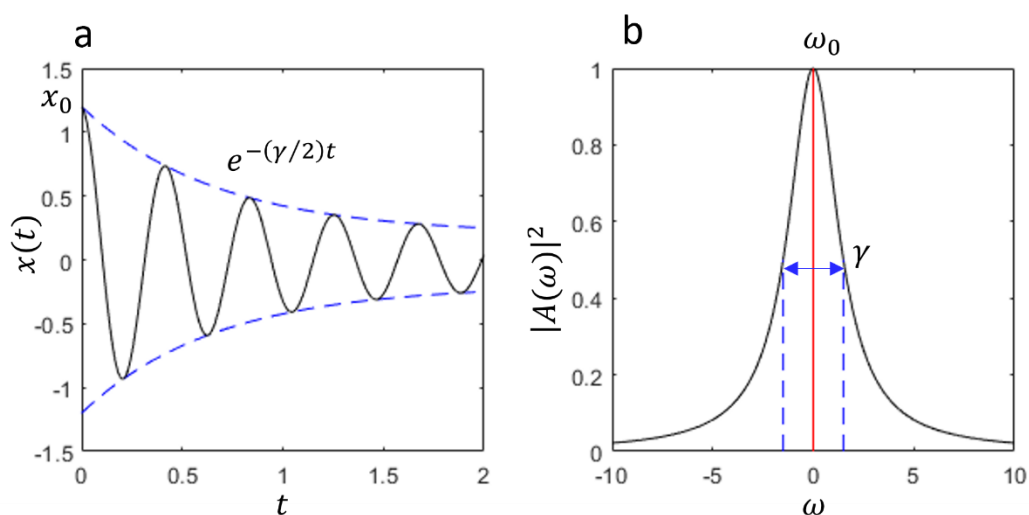From this we can see that as the time of interaction approaches zero the band broadens significantly (76).

Figure 2.3 a) Damped harmonic oscillation b) the frequency distribution $A(\omega)$ obtained from the Fourier transform of $x(t)$ shown as the amplitude $|A(\omega)|^2$.

The excitation of the molecule can be treated as a damped harmonic oscillator. This is what leads to the Lorentzian components of the peaks. The damped oscillation, $x(t)$, with a damping constant γ, can be described as the superposition of oscillations with different frequencies ω and amplitudes $A(\omega)$:

$$x(t) = \frac{1}{2\sqrt{2\pi}} \int_{-\infty}^{\infty} A(\omega)e^{-i\omega t} d\omega \qquad [2.9]$$

where the amplitude $A(\omega)$ can be calculated from the Fourier transform:

$$A(\omega) = \frac{1}{\sqrt{2\pi}} \int_{0}^{\infty} x(t)\cos(\omega_0)e^{-i\omega t} dt \qquad [2.10]$$

where ω_0 is the central frequency of oscillation, in this case the frequency of the Raman peak (76). This can be integrated to give:

$$A(\omega) = \frac{x_0}{\sqrt{8\pi}} \left(\frac{1}{i(\omega - \omega_0) + \gamma/2} + \frac{1}{i(\omega + \omega_0) + \gamma/2} \right) \tag{2.11}$$

The Real intensity $I(\omega)$ proportional to $A(\omega)A^*(\omega)$. Close to the central frequency, ω_0, the value of $(\omega - \omega_0)^2 \ll \omega^2$, therefore the $(\omega + \omega_0)$ can be neglected. This means the intensity of the peak with respect to the frequency shift from the central frequency is:

$$I(\omega - \omega_0) = \frac{C}{(\omega - \omega_0)^2 + (\gamma/2)^2} \tag{2.12}$$

where C is a constant to normalise the intensity such that:

$$\int_{-\infty}^{\infty} L(\omega - \omega_0) d(\omega - \omega_0) = 1 \tag{2.13}$$

where $L(\omega - \omega_0) = I(\omega - \omega_0)/I_0$. From this we get that the constant $C = I_0\gamma/2\pi$. $L(\omega - \omega_0)$ is called the normalised Lorentzian profile and has a full width half maximum of $\delta\omega = \gamma$ (76). This is shown in Figure 2.3b.

2.1.5.2 Gaussian broadening

As well as the Lorentzian structure of the vibrational modes there are other factors to consider. These factors typically introduce a Gaussian broadening to the peak. They are dependent on the samples that are being investigated, and the configuration of the optical microscope. In the gas phase there is often a significant Gaussian broadening caused by the Doppler effect. The apparent emission frequency of a molecule moving relative to an observer is:

$$\omega_e = \omega_0 + \boldsymbol{k} \cdot \boldsymbol{v} \tag{2.14}$$

where $\boldsymbol{k}$ is the wave vector of the emitted radiation and $\boldsymbol{v}$ is the velocity vector of the molecule. When $\boldsymbol{k} \cdot \boldsymbol{v} > 0$ frequency increases and when frequency $\boldsymbol{k} \cdot \boldsymbol{v} < 0$ decreases. It therefore follows that it is only the velocity in the direction of the wave vector, what we will define as v_z, of the molecule that affects the frequency shift (76).

At thermal equilibrium, the molecules in a gas follow a Maxwellian velocity disruption. This means that for any given temperature, T, the number of molecules with a velocity between v_z and $v_z + dv_z$ and energy level E_i, is

$$n_i(v_z) = \frac{N_i}{v_p\sqrt{\pi}} e^{-(v_z/v_p)^2} dv_z \tag{2.15}$$

where v_p is $(2kT/m)^{1/2}$ and N is the density of molecules in the energy level E_i. It can then be shown that the intensity profile of a Doppler-broadened spectral line becomes:

$$I(\omega) = I_0 exp\left[-\left(\frac{c(\omega - \omega_0)}{\omega_0 v_p}\right)^2\right]$$
[2.16]

This has a Gaussian profile with a full half width of $\delta\omega_D = \frac{s\sqrt{\ln(2)}\omega_0 v_p}{c}$. It is worth noting here that in this form of peak broadening is linear with the frequency (76). Another form of peak broadening is caused by the laser, spectrometer, and microscope used to measure the peaks. Laser spots are typically Gaussian in shape following the equation

$$I(r,z) = I_0 \left(\frac{w_0}{w(z)}\right)^2 exp\left[-\left(\frac{-2r}{w(z)^2}\right)^2\right]$$
[2.17]

where, $w(z)$ is the radius at which the field amplitudes fall to 1/e at a given height, w_0 is the waist radius at zero, z is the distance from the imaging plane, and r is the radius from the centre of the spot. This beam shape is then propagated on to the spectrometer assuming no other spatial filters and will have a significant effect on the peak shape if not corrected. Mayerhöfer et al point out in there 2018 work that modern slit based spectrometers make mean that this consideration does not vastly effect the "goodness of fit" if a pure Lorentzian is fitted to a peak (77). With the spectrometer set up as described for use in chapter 3 however our slit does not act as a spatial filter so these considerations must be investigated.

When band fitting it is possible to combine both a Lorentzian and a Gaussian profile in two ways. Either as a linear combination or as a convolution of the two called a Voigt profile (77). While a linear combination of the two is computationally fast and will account for much of the discrepancy between the pure Lorentzian and the true, the Voigt profile is a much more accurate representation of the combined effects of energy uncertainty, peak broadening, and microscope effects. A Gaussian profile has a sharper centre peak and approaches zero much faster. In contrast the "wings" of a Lorentzian profile have higher intensity further out. 5 FWHM from the centre the Lorentzian profile has 1% of its peak intensity.

2.1.6 Confocal Raman spectroscopy

Confocal Raman spectroscopy is used to maximise spatial resolution in Raman spectroscopy by focusing on a single, tightly confined point to localise the signal generated and detected. Confocal Raman spectroscopy takes advantage of high numerical aperture (NA) lenses and pinholes to highly localise the area from which the Raman signal is detected. A microscope objective with high NA focuses the laser beam to a small area. There is also a pinhole in the form of a slit at the spectrometer. This localised distribution of signal allows for high spatial resolution scans to be performed on samples as small as cells, though resolution is limited by the wavelength of light.

Figure 2.4 shows that the beam is brought down to a point at z=0. This is the focal point. The beam width is dependent on the angle the lens focuses the light to and at z = 0, ω_0 is the spot size. This highly localised excitation spot is localised in the z direction as well as the x-y plane. This means that three dimensional structures can be imaged (78) by scanning the sample in all three dimensions. There is a limit to the depth that this method can scan into a material due to the Rayleigh scattering that photons undergo in a turbid material. This means the spatial resolution decreases rapidly as the depth increases.
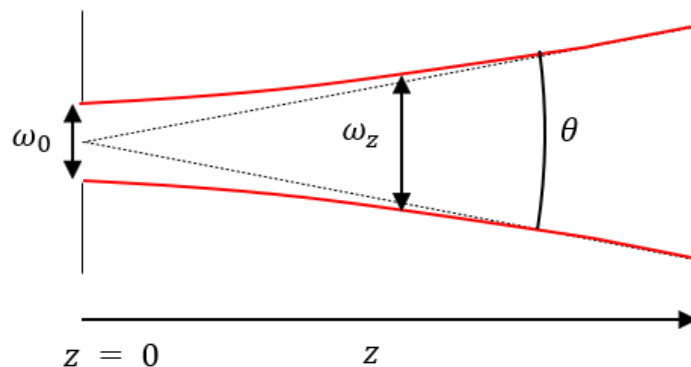
Figure 2.4: A schematic of a laser focused to the ω_0 is the beam width, z is the vertical distance from the focal point, ω_z is the width of the beam at distance z from the focal point, θ is the angle made with the beam as if the beam width were 0. The red line is the outer edge of the beam and the black dotted line is the line from the centre of the beam at the focal point to the outer diameter of the lens.

Each set of measurements taken in an x-y plane at a given height Z can be considered an optical slice of the material. These slices can be aligned and used to create a 3D image of a sample. Figure 2.5 shows a 3D map of an endothelial cell imaged using the area under the

30

2800-3020 cm^{-1} band at each point. These slices that are seen in part A are put together to generate the 3D image that is shown in part C and sliced in part D. While the spatial resolution of these images is very high, the volume that is imaged is less that 3 cm^3 for the whole scan. Since each point in the 3D sample requires a Raman spectrum to be acquired this method does not scale up easily to large volumes even where scattering does not present a problem.
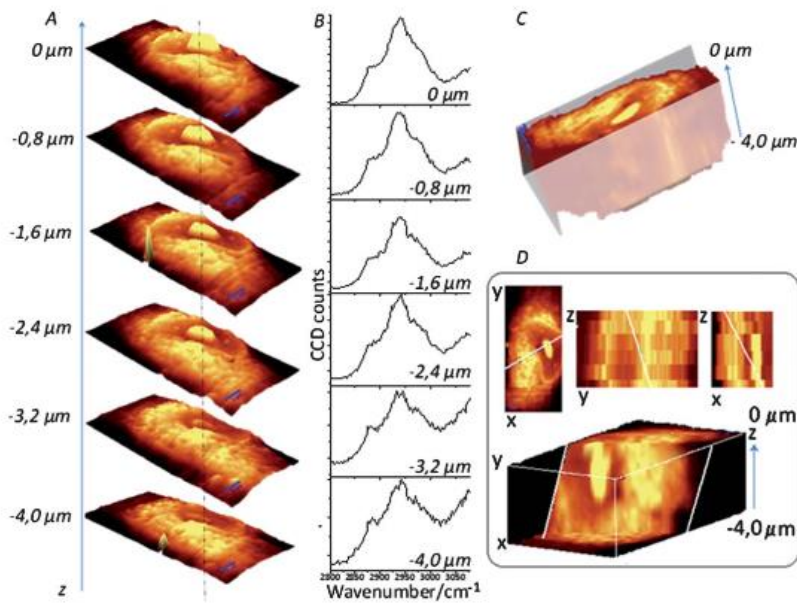

Figure 2.5: a) Confocal Raman imaging-stack of an EA.hy 926 cell covering 16.7x34.1x4mm^3. Integration map over the C–H band(2800–3020cm^1 range), b) single spectra extracted from the same point in the maps (dotted line), c) a reconstructed 3D image seen from the top d) and a cross-section of the reconstructed 3D image (D). Taken from reference (79)

2.2 Diffuse Raman Spectroscopy

2.2.1 Spatial offset Raman spectroscopy (SORS)

While confocal Raman spectroscopy is used to maximise spatial resolution in Raman spectroscopy by focusing on a single, tightly confined point to localise the signal generated and detected, SORS uses the diffuse nature of light to build a depth profile for the chemical properties of a sample. The use of scattered photons means that SORS has the potential to be used to sample much larger volumes of material than the confocal method of three-dimensional sampling. While confocal Raman spectroscopy can take advantage of non-scattering medium to measure deeply through clear samples, SORS relies on the scattering to generate the photon paths. This means that in materials that do not scatter photons SORS will not work. This is most easily demonstrated by the fact that confocal is used on samples that are on a glass slide with no need for SORS to image the sample through the slide.
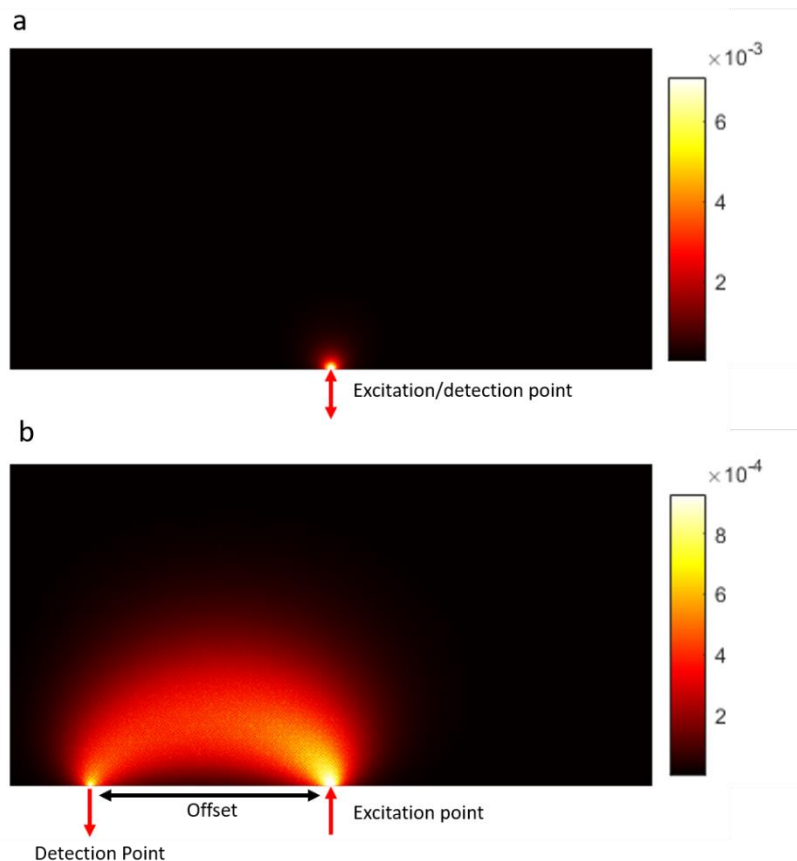
Figure 2.6: SORS compared to conventional Raman microscopy, a) The spatial origins of the Raman photons that are collected from conventional Raman. b) The spatial origins of the Raman photons that are collected from a single offset during SORS.

As discussed in Section 2.1.1**Error! Reference source not found.**, the vast majority of photon scattering events are Rayleigh scattering. Rayleigh scattering being the main form of scattering means that the light that scatters through the whole medium has the same wavelength as the excitation laser. The Raman signal can still be generated from scattering events that happen deeper in the material so any light that makes it back to the surface will contain the same chemical information. Figure 2.6 shows the distribution of Raman signal that is generated within a sample for two different configurations; traditional Raman spectroscopy (where the excitation and collection points are the same), and spatially offset Raman spectroscopy (where the light is collected from an offset). The colour of each node indicates the contribution of that node to the Raman signal detected at that collection point for the given excitation detection pair. The colour bars on Figure 2.6 show that the number of Raman photons collected is significantly higher for traditional Raman as there is the minimum average photon path of absorption.

The scattering of the photons is dependent on the scattering and absorption coefficients of the materials as well as their concentrations. This means that rather than just reflecting chemical properties of the material, the Raman signal will be dependent on the structural and geometric properties of the sample (80). Raman signal propagation will follow the normal propagation of photon scattering as the vast majority of the scattering events that happen before and after the Raman scattering event are Rayleigh scattering (71).
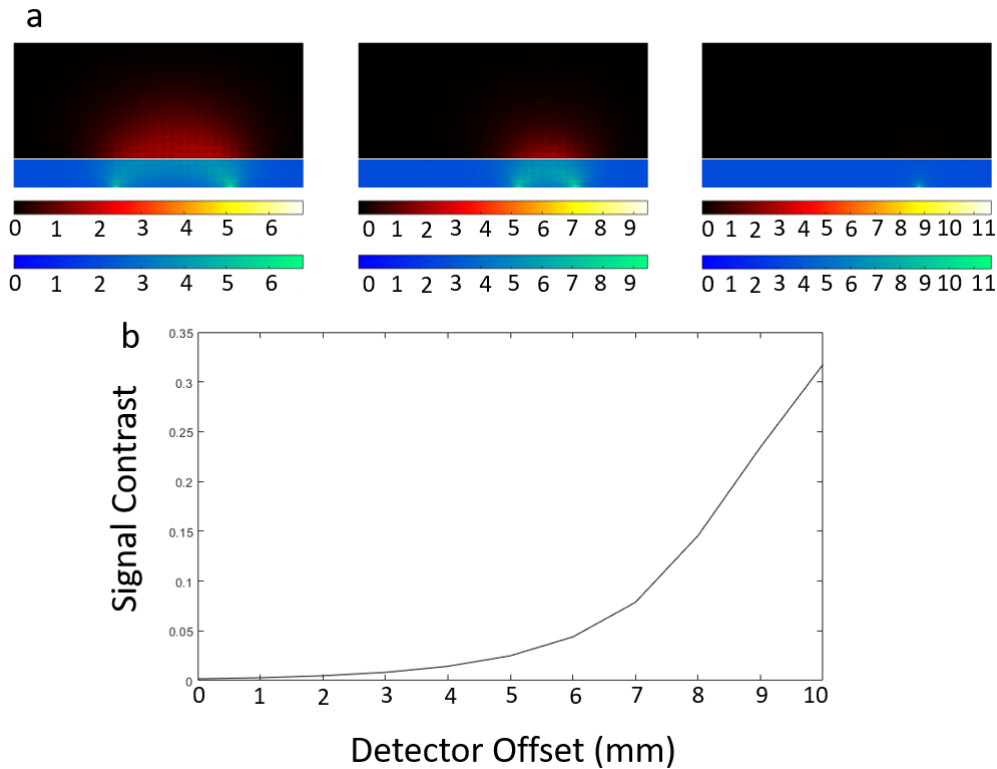
Figure 2.7 a) The spatial origins of the Raman photons in a two-layer system where the blue/green region is a 2mm thick surface layer and the red/black region shows the 8mm thick sub layer. (Left) shows an 8mm offset, (middle) shows a 4mm offset, and (right) shows 0mm offset Raman. b) The relative contribution of the two layers as defined by the total signal from the deep layer divided by the total signal from the surface layer against the offset of the detector from the excitation point.

Figure 2.7 shows the difference between the excitation path for conventional Raman and a single offset variant of SORS. The simplest form of SORS is the use of a single offset collection point focused on some distance from the excitation point of the laser. This signal alone can be used to measure the contents of a container of known material as the signal from the other side of the boundary of the container will be relatively higher than that of material the container is made of. By the method of combining a single offset with a 0 mm offset, or conventional Raman, signal it is possible in some cases to separate the signal of the two materials in a simple two-layer system. This is because the surface layer dominates the signal in 0 mm offset and the difference between the signal of the zero and non-zero-millimetre offset is the contribution from the deeper material. This can be seen qualitatively by comparing the subsurface layer from Figure 2.7a left and Figure 2.7a right.

With a single offset more information cannot be gathered. From this single point of information, it is not possible to determine exactly what concentration or depth a different material is without prior information. If the geometry of the system is known, it can still be possible to build an understanding of the concentration of separate materials in some cases.

2.2.1.1   *Diffuse Raman spectroscopy configurations*

Multiple methods exist for generating an offset between the excitation and collection points. These include using two objectives, using digital micro-mirror displays (DMD), mirror galvanometers, and optical fibres.

As shown in Figure 2.8 the method of two objectives involves using a normal Raman spectrometer set up which can be used to take measurements with a single point. A second objective can be focused on a point some distance away from the excitation point. This creates an offset between the excitation of a normal traditional Raman set up and a collection point of the extra objective.
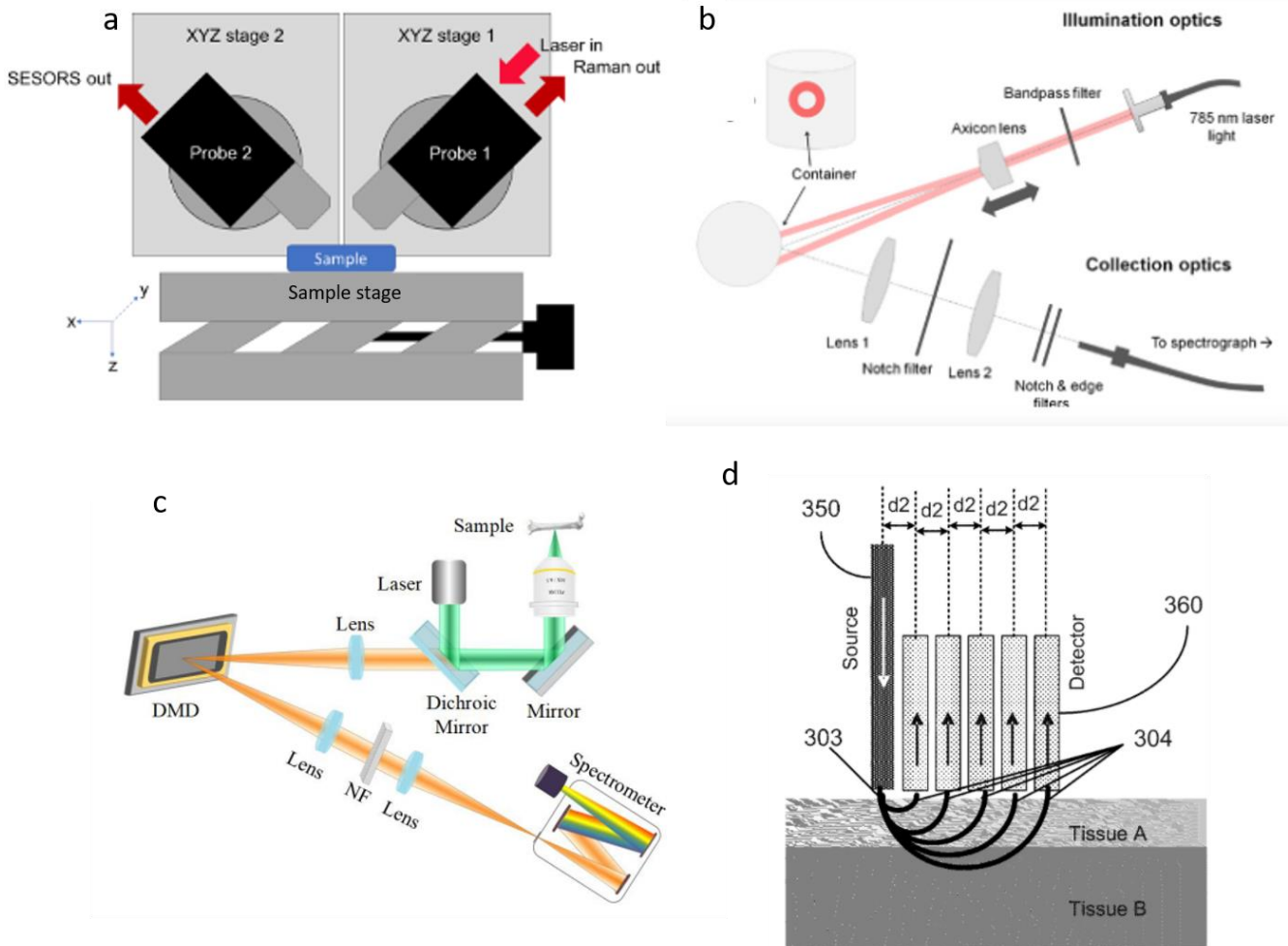
Figure 2.8: a) Schematic of the Raman spectrometer used in SORS and SESORS experiments. Taken from (81) b) Circular iSORS created with an axicon lens. Taken from (82) c) Schematic of SORS system with DMD controlling. Note: DMD, digital micro-mirror device; NF, notch filter. Taken from (83) d) A fibre optic probe with different fibres for excitation and collection. Taken from (84).

The use of a mirror galvanometer before the objective and the dichroic mirror allows the angle of the laser to be adjusted so that the laser enters the objective not parallel to the normal line. This means that the laser point will be offset from centre at the sample. In this way a single point or a ring can be excited on the sample while light is collected from the centre. This configuration is called inverse SORS as the ring illumination is around a central collection point compared to SORS where the central point in used for excitation.

The other method for selecting multiple offset points is the use of fibre optics. Each fibre can be taken directly from the objective to the spectrometer. In this configuration the probe often uses different fibres to excite and collect signal so a true 0 mm offset may not be possible. While the efficiency of a fibre optic system has the potential to be greater than that of current DMD set ups, Figure 2.8d shows that a probe is often a solid body of metal with fibres attached in a fixed format. While this gives a very stable system, fibre optic SORS systems lack the flexibility of DMD-based SORS.

Instead of creating an offset excitation point it is possible to select multiple collection points. This can be achieved by placing a DMD in the path from the sample to the spectrometer. By selecting small points on the DMD that are offset from the central excitation point artificial pinholes can be created to be reflected into the spectrometer, this is shown in Figure 2.7. This is the method that was selected for the initial experimental investigation undertaken in this thesis and will be discussed at length in chapter 3.

2.2.1.2 Depth detection of chemical defects independent of their concentration

Mosca et al showed that an estimation of the depth of an inclusion is possible in certain conditions using a method that is not dependent on the concentration of the material being measured (85). The scattering coefficients of a material is dependent not just on the properties of the materials but also the wavelength of the photon that is scattered. The extreme example of this is that x-ray radiation passes through the softer materials of the human body with hardly any scattering allowing clean and sharp images of the human skeletal structure, whereas visible wavelength photons are absorbed efficiently by just a few millimetres of skin (e.g., the eyelids) to reduce the visible amount of light close to zero.

The relative absorption at different wavelengths changes less drastically in SORS, but across the range of approximately 100 nm, which is roughly the width of the fingerprint region at 785 nm, there is enough of a change in absorption and scattering to measure depth in material. With a known material it is possible to calculate or measure the absorption of different peaks with regards to path length. By measuring the ratio of two peaks with significantly different absorption coefficients under normal Raman conditions a baseline is set. As that material fills a defect that is deeper and deeper into a bulk material the ratio of those two peaks changes further as the photons that have the wavelength with higher

absorption will be absorbed at a faster rate. The ratio of these to peaks can be used along with other known factors to generate a form of depth profile.
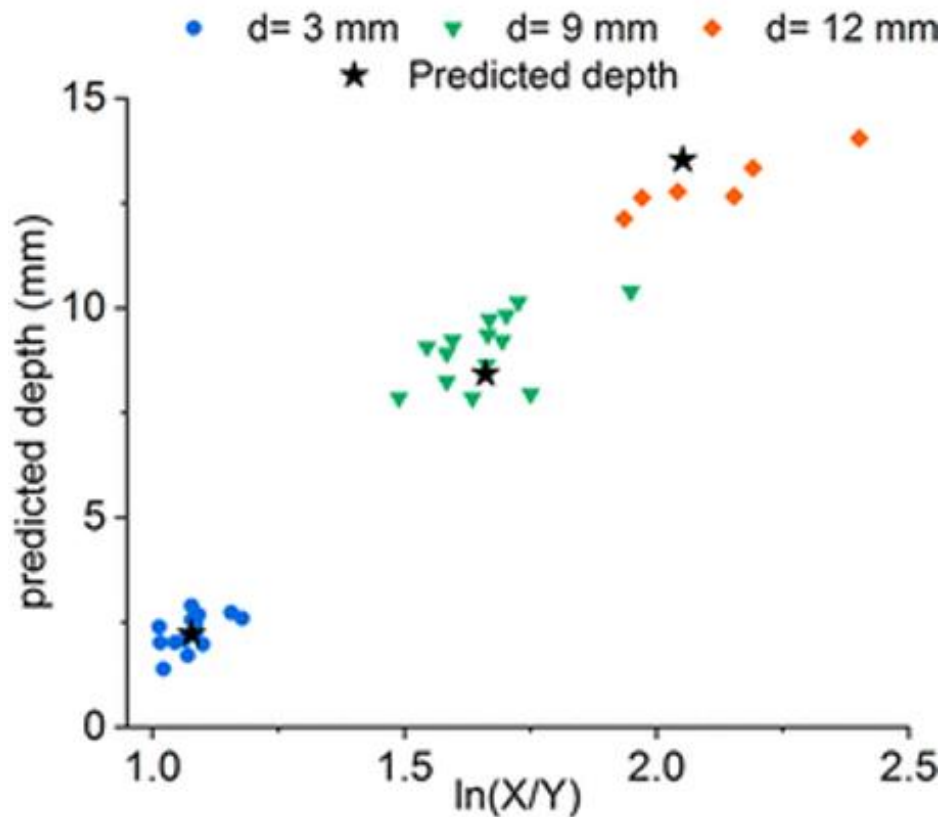

Figure 2.9 The predicted depth against the log of the ratio of the two peaks used for the prediction model. Each colour denotes a defect at a different depth, each point is the prediction model of a single offset reading and the star is the prediction that considers all the predictions from the offset. This graph is taken from Stone et al. (85)

The sample used to create figure 2.9 was homologous, and the defect was directly in line with the collection point. A model of the signal ratio to depth was created using multiple measurements at different depths. Each offset then can make a prediction about the depth of the defect. By combining the answers from multiple defects, they were able to increase the predictive power of the method; particularly combining SORS with another form of diffuse Raman spectroscopy, transmission Raman spectroscopy, improved accuracy further. As can be seen in Figure 2.9, each individual offset allows for some level of prediction. In the paper the authors combined measurements from multiple offsets to improve accuracy.

This method of detection of the depth of a material is concentration independent because it relies on the relative strength of the two peaks rather than the absolute values. Since the absolute values of the spectra are dependent on the chemical properties of the material rather than amount of the material, the depth of a defect of any concentration can be calculated using the same calibration model.

There could be several ways to apply a spatially offset technique to Raman spectroscopy. It is possible to gather qualitative depth information, such as the detecting the existence or concentration of depth materials or suppressing unwanted surface signal. With the application of appropriate mathematical models, it may also be possible to use the above technique to build a quantitative understanding of a tightly constrained system, such as the concentration of a known material in a package of known size.

2.2.1.3 SORS and Inverse-SORS

There are two major forms of SORS that are typically used. The first is a configuration with a single illumination point and multiple collection points often arranged in circles around the central illumination point. This configuration is designated SORS (Figure 2.10c). The inverse of this is to have a single central collection point and rings of illumination points. This is designated Inverse-SORS (Figure 2.10b). Both configurations have their benefits and disadvantages.
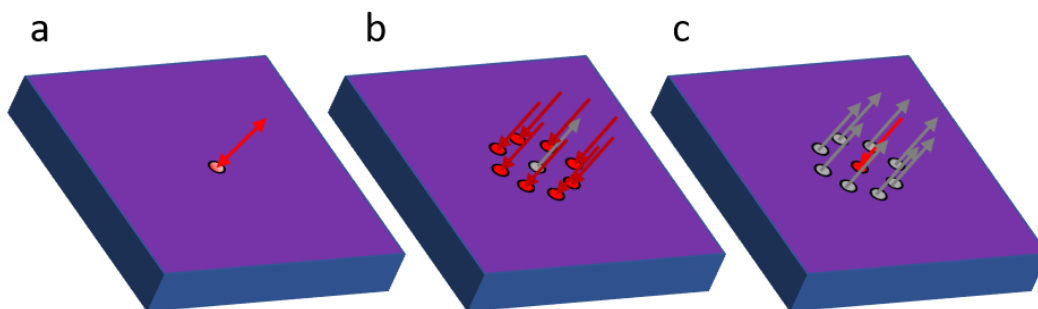
Figure 2.10 a) A sample with a single excitation/detection point, conventional Raman. B) A ring of excitation points around a central detection point, inv-SORS. c) A ring of detectors around a central excitation point, SORS.

Given the low efficiency of Raman spectroscopy as a detection method it is often preferable to have high powered lasers as the illumination source. Given that Raman microscopy requires the spot to be focused to get high spatial resolution this can often lead to high

power densities. The issue with high power density sources is that this can cause laser damage to the surface that is being imaged. To this end it can be beneficial to reduce the power density to reduce damage. Given that total Raman signal is proportional to the incident light it is preferable not to lower the power of the laser. Increasing the surface area of illumination point is the other option and this is what inverse-SORS does. By illuminating in a ring, the surface area of the illumination point scales with r^2 of the illumination ring. Increasing the offset increases the number of detectors that can be placed on the surface. Since photon count noise is proportional to the square root of the number of photons, inverse-SORS has the potential to increase signal to noise proportional to the radius of the detection ring in the same amount of time.

Depending on the configuration of SORS it is often possible to measure Raman signal from multiple offsets at the same time. A single point can be at the centre of a ring of detectors. Building another ring of detectors around the first does not interfere with the readings as all detectors are independent of each other. This can either be carried out using a DMD that we used or using concentric rings of fibres. These configurations mean that readings of multiple offsets can be parallelised to increase the time efficiency of readings. This can make up for some of the lost efficiency due to the smaller detection size. Taking readings from multiple offsets at the same time also brings other benefits and is the main benefit of SORS over inverse-SORS. In the case of inverse-SORS a full ring illumination means the light detected at the central point is detected all at the same time and in the same spectra as SORS. Multiple excitation points used at the same time will cause a combination of signal from the different excitation points at each collection point. To simplify the analysis of the spectra each ring offset is excited in turn. With SORS, however, the spectrum at each point is separate from the others. Due to this, with SORS, it is possible to multiplex the readings for multiple offsets at the same time.

For applications in industry, which impose constraints on the measurement conditions, (such as a powder in a plastic bag), an inverse-SORS set up can be the better choice to maximise light throughput and simplify data analysis. Systems such as Agilent have created quick and powerful devices for the fast identifications of materials through bags, sacks, or thin-walled boxes. Our interest in SORS as a steppingstone to creating a diffuse Raman based imaging technique means that the benefits of radial resolution as well as the ability to

take several offsets at once are something that we are willing to sacrifice raw signal for. It may be possible to increase signal in two ways, firstly, the optimisation of parameters such as collection point distribution, and, more importantly, the utilisation of the full diffuse Raman illumination detection space.

2.2.2   Simulation of diffuse spectroscopy.

Simulation is a powerful tool for understanding diffuse photon paths. Figures 2.5 and 2.6 showing the spatial distribution of the origin of Raman photons within a sample were created using NIRFast which is a numerical simulation tool that uses finite element method. Here we compare this method with the more tradition Monti Carlo method as shown in Figure 2.166.

2.2.3   Monti Carlo Vs NIRFast

2.2.3.1   Monti Carlo simulations

Monti Carlo simulations are a branch of simulation that use randomisation to investigate a statistically significant collection of states of a system. Monti Carlo simulations are mostly limited to systems that aren't easily described by mathematical equations with unique solutions. They have been utilised in several unique fields such as chess engines, meteorology, and financial analysis (80).

Monti Carlo has been applied to photon scattering for some time, both in astronomy where it is used to investigate light scattering in gas clouds and nebulas, and more recently to understand the scattering involved in spatial offset Raman spectroscopy. In its simplest form this form of Monti Carlo tracks a simulated photon through a scattering material. The photon scatters by moving a distance, changing the angle, and moving another distance until the photon has moved outside of the scattering material.

The scattering distance is randomised across the same distribution of possible scattering distances. This is dependent on the scattering properties of the material and can be simulated by the equations:

$$S = -\frac{\log(RAND)}{\mu_s + \mu_a} \qquad\qquad [2.18]$$

where S is the distance travelled by the photon and μ_s and μ_a are the coefficients of scattering and absorption (86). $RAND$ is a random number that is uniformly distributed

between 0 and 1. The new direction that the photon travels in in the simplest simulation is simply a random direction chosen from the even distribution around a sphere. More complicated and accurate models take into account the anisotropy of the scattering, 'g', which considers the effect of the material of the scattering direction of the photon. By simulating millions of photons or more, a representative sample of the possible photon paths can be generated, and this can be used to give insight into how the simulated sample responds.

Layers of complication can be added to these simulations. For instance, for Raman spectroscopy more than a single wavelength needs to be simulated for a full spectrum to be generated. In order to simulate a spectrum, the relative quantum yields of the materials are needed. This can also vastly increase the number of photons that need to be simulated as simulating a full 1024-pixel spectra with the very low quantum yields that Raman has increases the possible vector space hugely (80).

This can be mitigated somewhat by treating each photon as a "packet" of photons where the assumption is made that any photon path will have a large number of photons that follow closely enough that path so that within the resolution of the system the paths will be effectively identical. By reducing the intensity of the excitation wavelength at each step the absorption of the photons won't lead to lost information where a photon that is absorbed in the single photon simulation is simply deleted.

At each step, an array of the intensity of the photon packet at each wavelength can be added to in the proportion of the Raman spectra of the material that the photon has scattered in. This way each step builds a Raman spectrum that will closely represent the spectrum that this sample would have generated with this combination of excitation and collection arrangements (80).

The strength of Monti Carlo simulations is that, once enough photons have been simulated to have reached a stable answer, all the morphology of the system can be simulated. The mesh for the arrangement of the materials and coefficients within the sample is limited only by the RAM of the system running it. Thin systems, or systems with a strong bias in the starting direction will be captured well by the rules of Monti Carlo.

The problem with Monti Carlo for SORS is that it does not scale well. As the offset that is being simulated is extended fewer and fewer particles reach the desired radius. This means that a longer and longer simulation needs to be run in order to saturate the probability space of possible photon paths to create a stable answer. The path length of each individual iteration cannot be scaled so a path length that is twice the distance takes on average twice as long to complete (86). As this path length increases the system becomes less and less efficient.

Monti Carlo Systems also have the problem of being potentially very computationally wasteful for simulating Raman systems. Any photon whose path takes it outside of the dimensions of the simulated sample is a photon that would be lost to the air in a real system. This means that that photon is deleted from the simulation and the computational time taken to follow that path of this photon does not contribute to the final answer of a spectrum at a given offset. This is true for any photon that leaves the sample in the imaging plane but at the incorrect offset from the detector, and it will not contribute usefully to the read out of the simulation. In this way only a very small fraction, less than 1% while simulating typical offsets in a Raman system, of the simulated photons will contribute to the spectral simulation.

2.2.3.2 NIRFast

NIRFast is a light diffuse simulation software package developed for near infrared tomography. It is a numerical system that is based a finite element method (FEM) (86). Numerical simulations are often much faster than Monti Carlo systems due to the limitations discussed in the previous section. The assumption that allows NIRfast to mathematically solve an analytical problem is the assumption that our system is outside of the diffuse limit. The diffuse limit is the limit at which the addition of successive photon scattering instances, the anisotropy of individual scattering event decreases in importance; at a sufficient number of scattering events the average direction of all the photons in the system is no longer dependent on the anisotropy of the scattering events. Instead of modelling each individual photon the model uses the diffusion approximation equation:

$$-\nabla \cdot \kappa(r)\nabla \Phi(r,\omega) + \left(\mu_a(r) + \frac{i\omega}{c_m(r)}\right)\Phi(r,\omega) = q_0(r,\omega) \qquad [2.18]$$

where and μ′$_s$ and μ$_a$ are the reduced scattering and absorption coefficient, $q_0(r, \omega)$ is an isotropic source term, $\Phi(r, \omega)$ is the photon fluence rate at position r, and modulation frequency, $\kappa(r) == \frac{1}{3(\mu_a + \mu'_s)}$ is the diffusion coefficient and $c_m(r)$ is the speed of light in the medium at any point, defined by $\frac{c_0}{n(r)}$, where n(r) is the index of refraction at the same point and c$_0$ is the speed of light in vacuum (86).

NIRFast uses a mesh which contains the spatial as well as optical properties of the material. This increases its scalability for use for large offset spatial offset the density of the mesh can be easily varied during set up. The total number of node points can be optimised for the combination of required resolution and the computing power available.
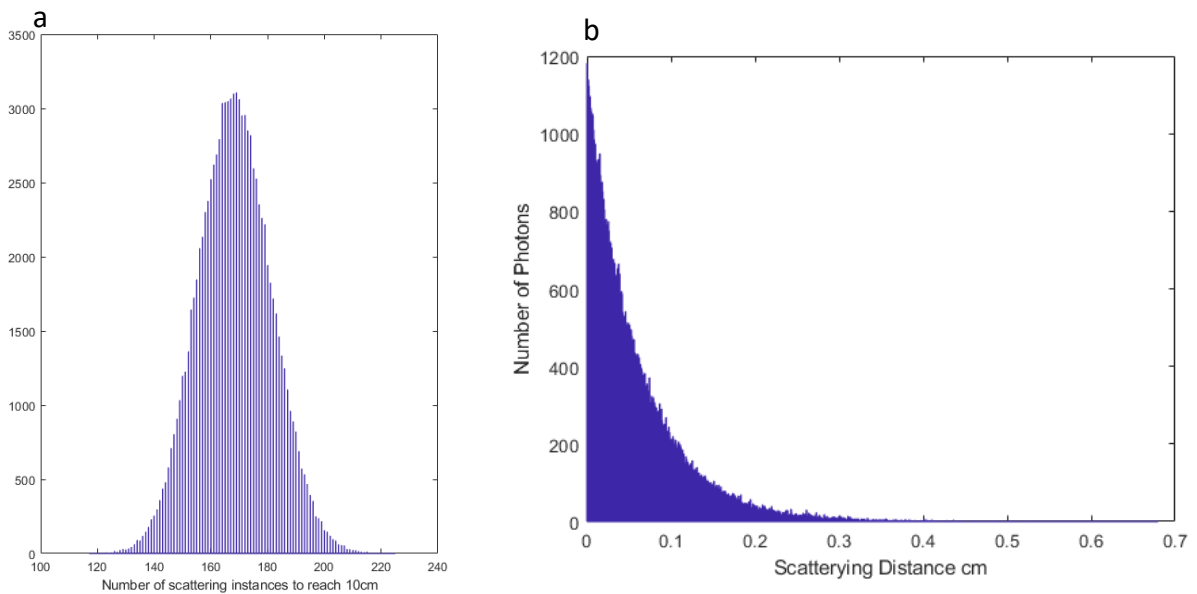
Figure 2.11 a) the distribution of the number of scattering events that travel on a 10cm path through the material, simulated in a Monti Carlo simulation written for the purpose. B) The distribution of distance between scattering events using equation 2.18 and a μ'_s of 10cm^{-1}.

The issue with dropping the anisotropy component and using the diffuse approximation is that short photon paths and the interactions through small inclusions in a simulated system may be less accurate. This possesses limits on the use of NIRFast to simulate a real system. Two factors about the systems we will apply NIRFast to will mitigate this problem. Due to the use of large offsets in SORS, photon paths will be of the order of tens of millimetres. Combining this high number of scattering events with the strongly scattering material of interest in these studies we can calculate the number of scattering events.

Typical scattering coefficients for biological materials such as fat and skin range from μ_a =0.03–1.6 cm^{-1} and $\mu s'$=1.2–40 cm^{-1} (86) with common values of 0.8 cm^{-1} and 16 cm^{-1} respectively. From these values we can see that the mean scattering length is 0.06 cm. This scattering length means that there will be on average 165 scattering instances for a 10 cm photon path. A 10 cm path assuming a semi-circular path with no deviations would mean only a 1.5 mm offset. These numbers come from simulations of 100,000 scattering photons following the distance. The distributions shown in Figure 2.11. of 165 scattering events is enough to justify the diffuse approximation.

One small drawback of a mesh based system is that the illumination distribution is limited to points on the nodes. The exact Gaussian distribution of the exciton beams cannot be simulated, excitation is simulated at individual nodes which will often have a large enough separation that the excitation any enamouring node is effectively zero. This precludes the simulation of highly confocal SORS, which is not something we do with our larger focal length lens. This can reduce the maximum spatial resolution that we can achieve with regards to separating different offsets.

2.3   Spatial offset Raman Spectroscopy as a tool to study bone health.

2.3.1   Traditional Raman spectroscopy as used in bone analysis.

Raman spectroscopy has been used as a method to investigate bone quality for several years. This is because in the fingerprint region from 0-2000 cm^{-1} there are well defined peaks that characterise both the mineral and non-mineral components of bone while the high wavenumber region is dominated by lipid and water (86).
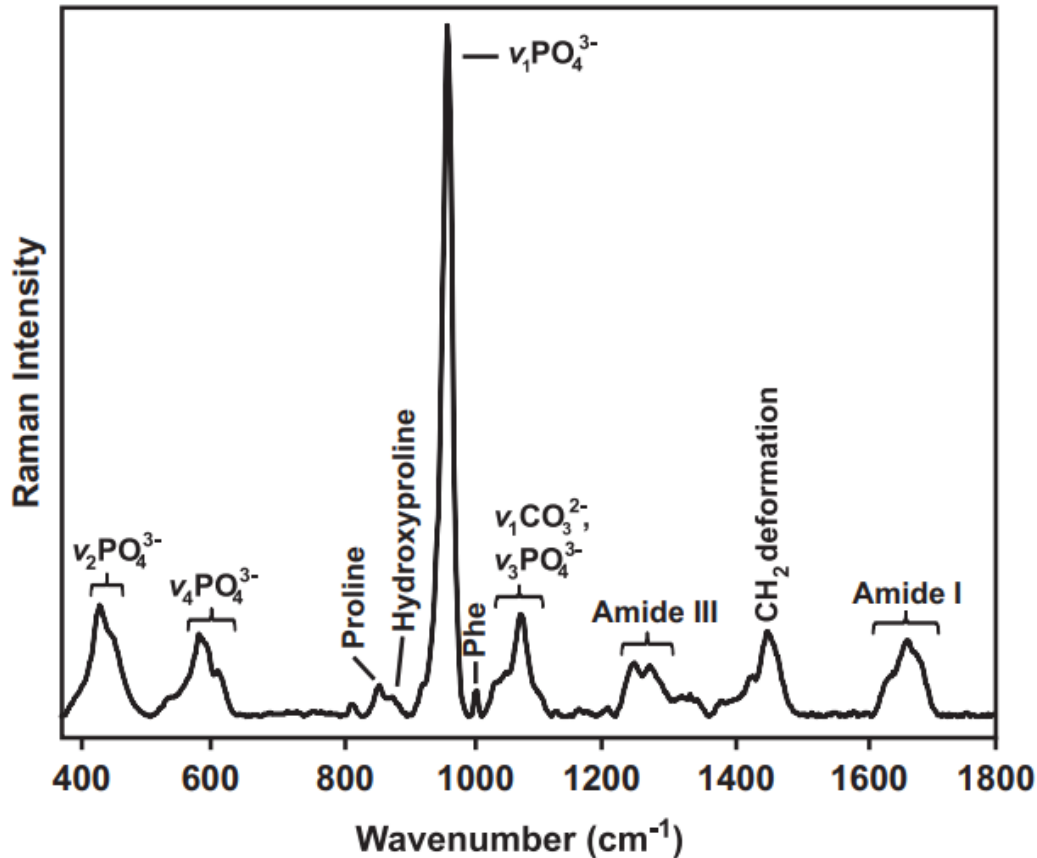
Figure 2.12 Baselined-corrected Raman spectrum of cortical bone acquired using a 785 nm laser. Major bone mineral and matrix collagen band positions and associated spectral regions are marked. (86)

The strongest peak is the 960 cm^{-1} peak, as can be seen in Figure 2.12, which corresponds to the phosphate band (86) and is characteristic of hydroxyapatite and other carbonated apatites. The exact position and width of the peak is dependent on properties such as the relative concentrations of monohydrogen phosphate and mineral carbonates, the crystallinity (87), and the mineral density (86; 88). The stronger the peak the greater the mineral density as we know from section 2.4 that Raman signal is directly proportional to number of molecules present. The relative concentrations of monohydrogen phosphate and carbonated apatites affects the peak position as monohydrogen phosphate has a lower wavenumber than the carbonated apatites which shifts the peak downward. Monohydrogen phosphate is present in higher quantities in young bone compared to older bone (89).

The crystallinity of the apatites affects the full width half maximum of the 960 cm^{-1} peak. A more regular structure within a crystal means that there will be less deviation in bond geometry so the excitation energies that the bonds can exhibit will be more similar. The result is that the full width half maximum is inversely proportional to the crystallinity of the mineral component (86).

There is a secondary peak that links to the phosphates and carbonates which is made up of an overlap of peaks from each material. This is the 1031cm^{-1} band from HPO_4^{-3}, and the 1070 cm^{-1} band from CO_3^{-2}. The relative heights of these two peaks can be used to determine the ratio of carbonate to phosphate within the bone.

Most of the other peaks within the fingerprint region are indicators of the chemical components of the extracellular matrix that makes up ~30% of bone. The most used indicators are the bands assigned to the CH_2 deformation vibrations at 1445 cm^{-1} and the Amide I band which is characterised predominantly by the overlapping bands the 1660 cm^{-1} and the 1690 cm^{-1} (83; 90). The 1660 cm^{-1} band is amide band related to the crosslink pyridinoline $\nu(C-O)$ and the 1690 cm^{-1} peak is related to the immature crosslink dihydroxylsinonorleucine (91). The ratio of these two can be used as an indication of mechanical damage to bone (92) and it has been shown that the relative amounts of dihydroxylsinonorleucine reduces with age (93) which suggests its use as measure of the maturity of bone. The other peaks of interest are the amide III peak at 1242 cm^{-1}, the proline and hydroxyproline peaks at 853 cm^{-1} and 876 cm^{-1}. While most of the peaks are not collagen specific, the proline and hydroxyproline peaks are and can be used to specifically interrogate the collagen content of bone structures.

Equation 2.4 shows us that the relationship between signal and chemical concentration is linear. This means that it is possible to measure the relative concentration of chemical species in a sample using just two peaks. An identifying peak is selected that corresponds to just one material in the sample for each chemical that is of interest. By comparing the relative intensities of the peaks against some known concentrations it is possible to work out the relative concentrations of the chemicals in the sample of interest. By selecting the 960 cm^{-1} peak as a proxy for mineral content and one band of the soft tissue band typically the 1445 cm^{-1} or 1660 cm^{-1} band it has been shown that calcium content can be measured.

Cooper et al showed that multiple peak ratios have the potential to investigate multiple factors at the same time though this requires further study (94).

2.3.2 Spatially offset Raman spectroscopy as applied to bone monitoring.

Both fibre optic probes and DMD based SORS have been applied to bone analysis and with each method comes trade-offs. SORS can be used to interrogate several different principal indicators of bone health. These range from directly measuring physical quantities of the bone such as mineral and collagen concentration (95; 96), to attempting to create models to allow the prediction of bone strength directly from Raman spectra (97).

In the application of bone monitoring the benefits of fibre optic and DMD based systems come with their own benefits and drawbacks. A fibre optic probe allows for more flexibility in the choice of configuration when designing the initial experiment. This can be seen by the fact that fibres have been used to measure Raman spectra in a backscatter (98), transmission (99), and radial (100) configuration. Once these probes have been designed, they are fixed, which offers less flexibility as new samples come in or new questions present themselves.

Liao et al showed that a DMD controlled by software could be used to select offsets and gather Raman spectra in a dynamic fashion (101). So far DMD based SORS has been limited to backscatter geometries for Raman signal collection though there is no reason to believe that the collection method would not be well suited to transmission Raman spectroscopy. Zhiyu et al discussed that the relationship between offset of the DMD and the spatial offset at the sample is proportional to the ratio of the objective lens and the lens that focuses onto the DMD (101). This relationship between the focal length of the objective and offset that can be achieved is one of the keys to the flexibility of DMD based SORS. This means that it is possible to achieve both SORS and micro-SORS with the same device by carefully selecting the Z position of the point of focus of the objective. Microscope objectives, with high magnification give high spatial resolution and allow for micro-SORS, and lenses with much larger focal lengths lead to much larger available offsets, allowing for SORS.

The application of SORS to bone detection was first shown in a paper by Matousek et al (102), where the bone in one human finger was measured. The measurement consisted of a fibre optic probe with a power density within the safe limit for human use. It compared two measurements: seven fibres at 0 mm offset and 26 fibres at 3 mm offset. The spectral region that was measured in the study was 800 cm^{-1} to 1800 cm^{-1} which encompasses the important peaks as outlined above. The study showed that when bone is at a depth of approximately 2 mm increasing the offset vastly increases the contribution of the bone to the total signal strength of the spectrum.
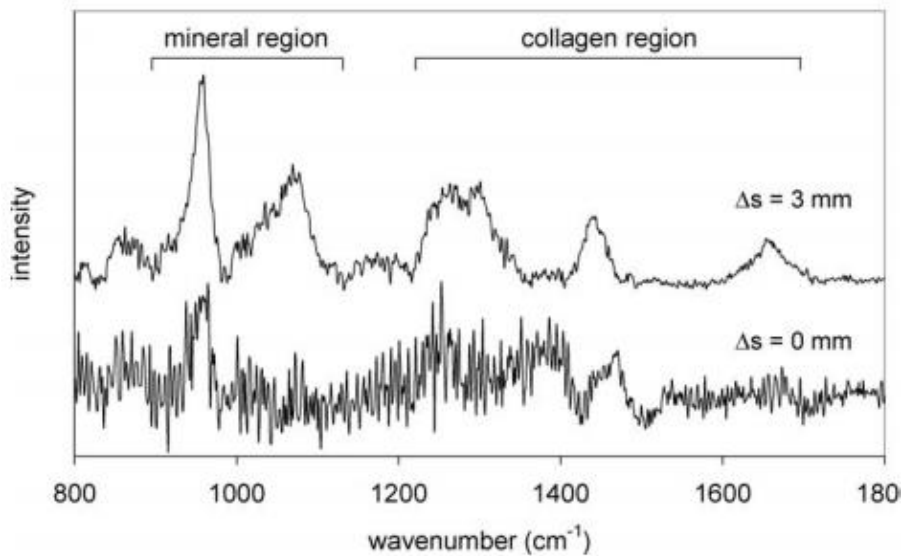
Figure 2.13 SORS spectra for a zero and 3 mm offset from the measurement of human bone of the thumb in vivo. Spectra are offset for clarity. Spectra labelled "Δs = 0mm" is the Raman measurement of the surface material with a skin-safe laser power. The spectra labelled "Δs = 3mm" is a measurement taken with a collection annulus with an offset of 3 mm offset (102)

Figure 2.13 shows that it is possible to increase the contributions of bone signal by increasing the offset. It also demonstrates that a subtraction method could be used to estimate the spectrum of the underlying layer. This showed that SORS could be used as a method of measuring chemical composition of bone without *a priori* knowledge of the

spectral composition of the surrounding soft tissue.
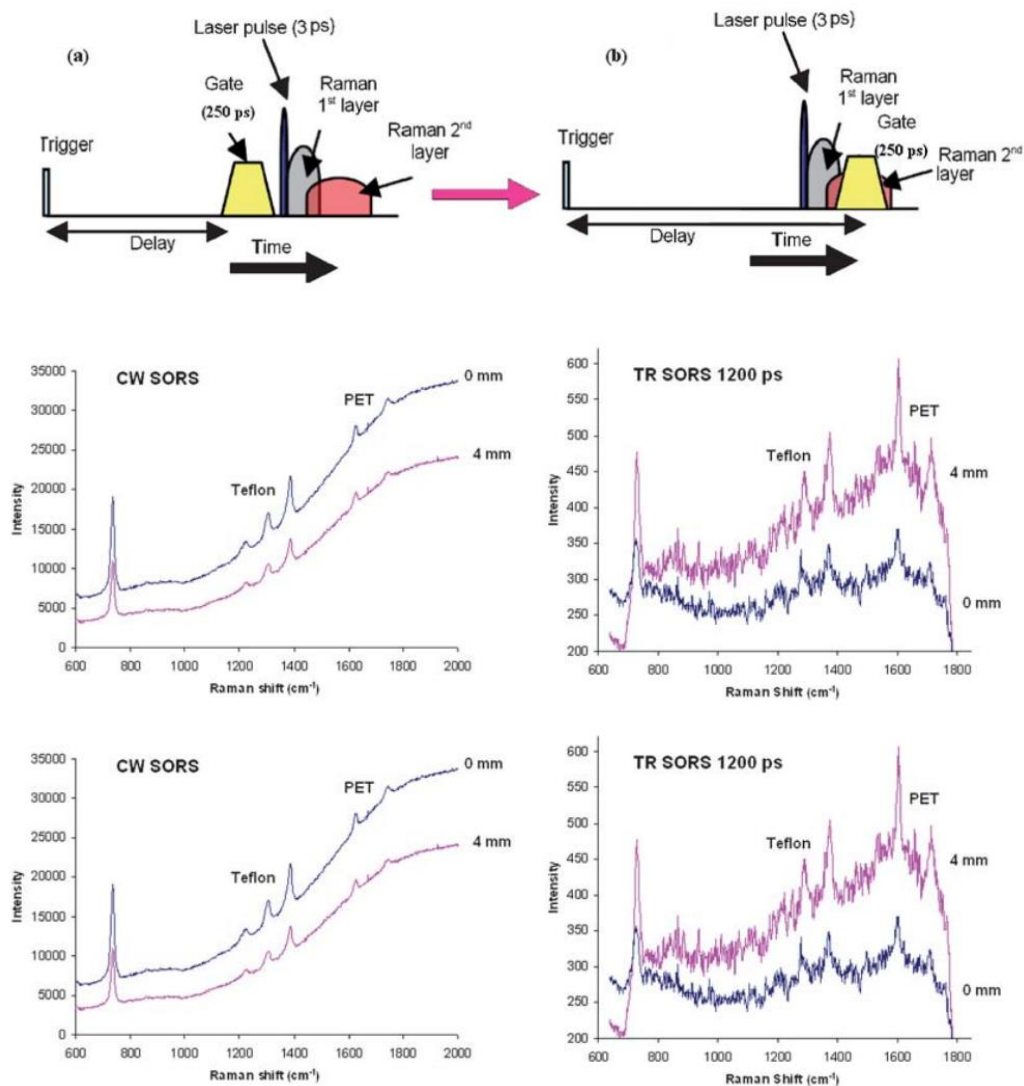
2.12. By selecting the time gate carefully, it is possible to preferentially select the signal from one part of a sample over the others. In this case using a Teflon top layer and a lower PET layer they showed that time resolved spatially offset Raman spectroscopy creates a significant improvement in surface layer signal suppression compared to constant wave SORS. So much so that with a 5 mm offset and an 800 ps delay the signal from the second layer is twice that of the top layer (103)*.*

Further investigation of surface layer suppression combined time resolved spectroscopy with spatial offset Raman spectroscopy. As photon velocity is relatively constant within a material, we know that scattering path length and time of flight are directly proportional to each other. This means that the photons associated with Raman spectra from deeper within a sample will arrive later than the surface layer

2.3.2.2 Applying data analysis and multivariate analyses techniques to the spectra gather with SORS to maximise the spectral fidelity of the reconstructed spectra

Methods of spectral reconstruction range from principal component analysis (PCA) and partial least squares (PLS), to more complicated methods such as band targeted entropy minimisation (BTEM). In 2014 Matousek et al used first a plastic phantom then a bone and soft tissue to test different methods for spectra reconstruction (104). They showed that in all methods that were tried, multivariate curve analysis (MCR), BTEM, and parallel factor analysis (PARAFAC), managed to reconstruct the spectra well enough to accurately reconstruct the phosphate-to-carbonate ratio to within 2%. The difference in methods came in reconstructing the Phosphate-to-amide III ratio which MCR produced 69% of a known reference measurement, BTEM reconstructed 275% and PARAFAC reconstructed 80%. They also showed that PARAFACT produced much lower noise in the silent regions of the spectra than BTEM.
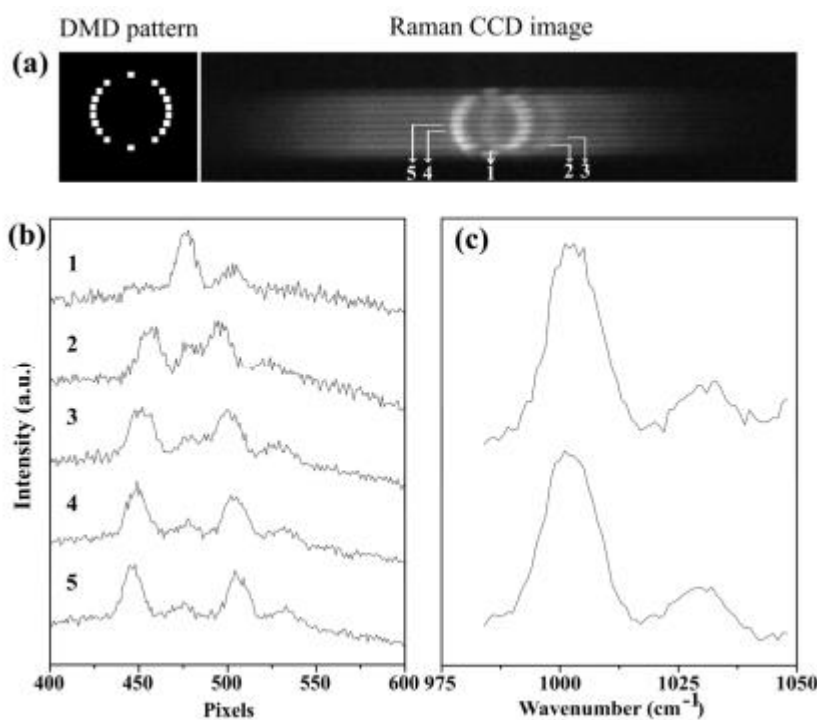
Figure 2.14 (a) Full-annular collection geometry for SORS spectra and Raman spectra captured on the spectrometer CCD; (b) Raman spectra corresponding to selected rows on the CCD, as indicated by 1, 2, 3, 4, 5. (c) Mean SORS spectra obtained by averaging the spectra from semi annular geometry (top) and full-annular geometry (bottom). Overlapped spectra, such as row 2 in (b), were excluded. Laser power: 14 mW, acquisition time 5 seconds. (101)

In 2016 Liao et al (101) developed a DMD based SORS system and tested it on plastics and biological materials. First demonstrating the potential of DMD based SORS to dynamically change the collection point geometries controlled by software (101). There was also a demonstration of multiplexing possibilities, by using a narrow pass filter they were able to place two spectra on the same channel of the CCD without interference between them that can be seen in Figure 2.15. They moved on to investigate biologically relevant materials. Regenerative medicine has been discussed in chapter 1 and monitoring the mineralising of scaffolds in a bone defect is one of the goals of our work. To investigate this possibility of this a phantom was created. First a layer of chicken skin was used as a surface layer, then a PGLA scaffold then hydroxyapatite powder. The powder was detectable through the scaffold and skin using an objective demonstrating the feasibility of using SORS in this capacity.
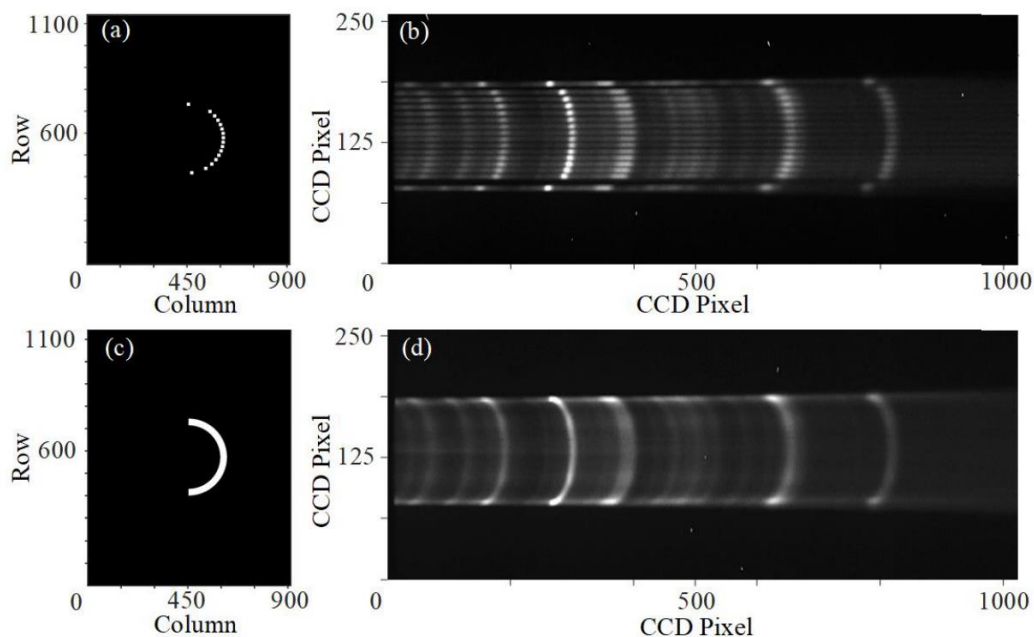
Figure 2.15 . Illustration of the mirror pattern used in the discrete (a) and continuous (c) DMD patterns; (b) and (d) images on CCD corresponding to the discrete and continuous patterns. The sample used was a 3 mm thick PMMA sheet. For (a) and (c), the x, y axis are the indices of the micro-mirror array on the DMD chip; for (b) and (d) the x, y axis are CCD pixel elements of the detector. (83)

Increasing signal to noise ratio would increase the fidelity of the recovered bone spectra. Cui et al (83) implemented a DMD based system that maximised the collection surface area. This was achieved by drawing a continuous arc instead of discrete points on the DMD.

Figure 2.15 demonstrates the difference in two styles of excitation distribution showing an increase in the surface area of 25% for the trade-off of a slight reduction in spectral resolution due to bleeding between rows. The paper also calculated a phosphate peak ratio with 1445 cm⁻¹ CH_2, 1660 cm⁻¹ Amide III, and 1070 cm⁻¹ CO_3^{-2} peaks, all of which increased with increasing collection offset.

2.3.2.3 Depth estimation

Measuring the position of a material of interest is almost as important as measuring the exact chemical properties of the material. A phosphate signal in breast tissue can be an indication of cancer but without spatial information to biopsy and then remove the tumour, the imaging method has limited practical use. Likewise, localising the signal to the edge of a healing bone fracture would help monitor healing without contributions from the bulk of the healthy bone surrounding. To this end there has been work on using the spectra gathered from SORS to predict the depth of a region of interest.

In 2008, Macleod et al used PCA as a method for prediction of depth of different materials (105). This was done by creating an initial data set with Teflon covered by sheets of paper. The layers of paper gave a 100 micron step size for the Teflon depths from 100-1400 microns and measurements at each depth was taken. Using the ratio of 730 cm⁻¹ Teflon peak to the 1100 cm⁻¹ surface peak a calibration was made. The calibration was successful up to a depth of 800 microns. Using root mean square error cross validation there was an error of 26 microns for the SORS depth prediction. This same method was then applied to bone using the 960 cm⁻¹ phosphate peak to identify the bone and the 1450 cm⁻¹ CH_2 peak to identify the bulk material. This new calibration using PCA and PLS achieved a 0.3 mm error on depths up to 5 mm.

Monti Carlo simulation has been used since the beginning of SORS to understand the distribution of photons generated within a sample during a SORS measurement. In 2005 Parker et al published a paper simulating a single top layer and a semi-infinite bottom layer (106). They showed that for each offset, there is a different depth where maximum signal is generated. They also showed in their two-layer configuration that while increasing the excitation power by using a ring excitation increased the total signal measured, it did not affect the signal contrast as that is a function of the geometry.
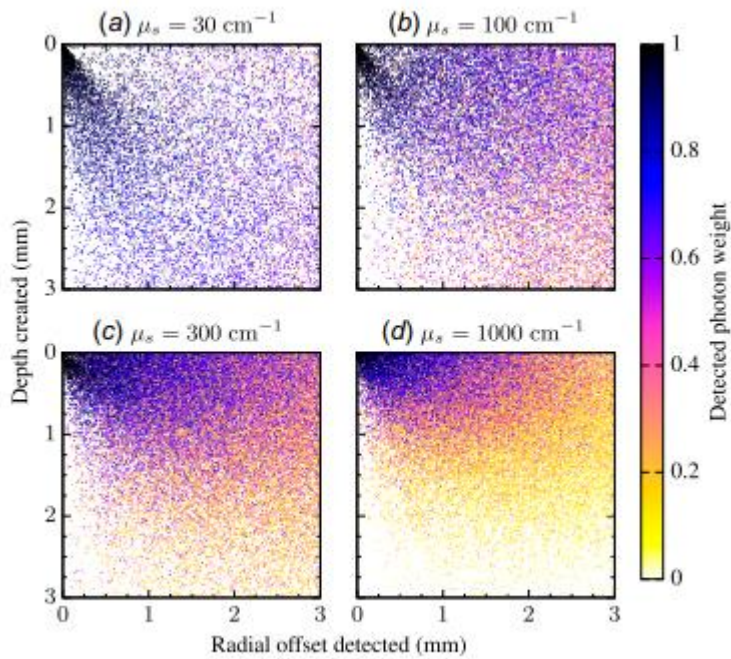
Figure 2.16 Visualizations of spatial origins of Raman photons from Monte Carlo simulation. Each figure(a-d) shows the density of Raman photons with an origin in that spatial coordinate for four different scattering coefficients. The scale bar on the right shows the scaled weight of each point where 1 is the maximum concentration and 0 is no generated photons. (80)

Further work by Di et al investigated the effects of scattering coefficient on photon distribution. They showed that the scattering coefficient can have a large effect on exactly where most of the signal is generated and then detected at a given offset (80). They also demonstrated that as the scattering coefficient μ_s of a sample increases, the spatial origins of the Raman photons become more and more localised to the excitation point, as can be seen in Figure 2.16. This shows the surface suppression effect may be more powerful in more highly scattering materials.

2.3.2.4   Monitoring bone health

As well as creating a mechanically stable framework for the body, parts of the bone are key producers of red blood cells. To this end when monitoring bone health, it is important to not just measure the structural components of collagen and mineral but also the internal structures of the bone such as the marrow (96). While detecting minerals through thin layers of skin is possible, the 960 cm^{-1} peak is a strong peak which means it could obscure

54

information from deeper in the bone. Therefore, an investigation was undertaken to take a measurement through bone, which was achieved through thickness of bone up to 3.9 mm deep with a 7 mm offset (90).

Investigation of both signal to noise and signal contrast was performed on bone and phosphate rich materials such as antler. By comparing the ratio of the 960 cm⁻¹ peak to the 730 cm⁻¹ peak from Teflon placed at various depths under phosphatic layers, a greater understanding of through-bone measurement was built (107). This study showed that different offsets were optimal dependent on the depth of the PTFE. There was also a difference between the optimal offset for the different materials showing that different depths and different scattering properties effect optimal offset.

2.3.2.5 *Prediction of bone quality from spectral features*

Okagbare et al introduced a Raman tomographic setup that used a set of axially offset fibre bundles to take Raman measurements around the outside of a chicken leg (108). This work used a single excitation point and each fibre bundle contained five collection fibres. Similar work by the same group (109) also involved coupling each fibre bundle with its own spectrometer to improve the dynamic range of the measurements. These studies demonstrated the ability of SORS to accurately measure the 1070 cm⁻¹ band which, allows for the monitoring of the relative concentration of carbonate. This capability has the potential to be used for the measurement of a small ~2 cm⁻¹ shift in the position of the 960 cm⁻¹ which can be an indicator of the age of bone. This was cross validated with three samples with varying CO_3^{-2} amounts as can be seen in Figure 2.17. This demonstrated the capacity of SORS to monitor biologically relevant spectral features through skin.
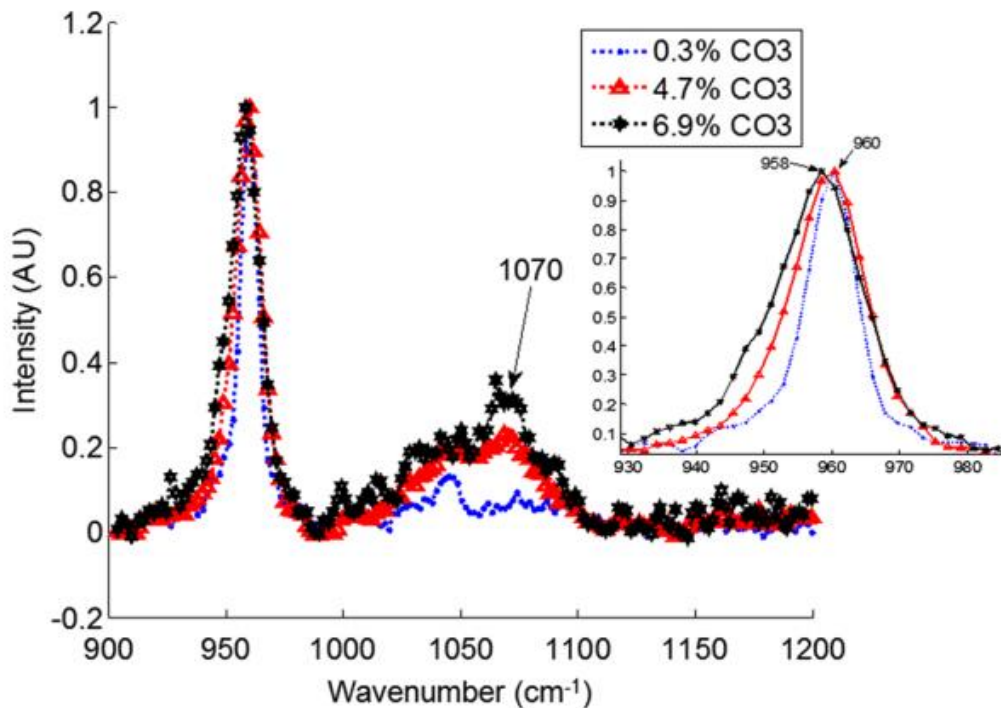
Figure 2.17 Transcutaneous Raman spectra acquired from rat leg. The rat leg models were constructed using carbonated hydroxyapatite with varied level of carbonate substitution. The expanded view of the spectra in showing the wavenumber range from 930 to 980 cm^{-1} is presented as an insert. (108)

Using inverse SORS this capacity to measure the relative signals of phosphate and collagen was applied by Buckley et al to investigate the composition of bone of a patient with osteogenesis imperfect (OI), a form of genetic disorder affecting bone collagen (95). Direct Raman measurements were taken of an excised femur as well as SORS measurements through skin on both the hand and the arm. Through use of BTEM, spectra decomposition was performed and the mineral-to-protein (phosphate-to-amide III) ratio was compared to a healthy age-matched patient. The OI patient's ratio was ~14% higher than the control and this increase was seen in both the SORS and exposed bone.

Direct prediction of bone quality through soft tissue continued to be a goal of SORS. In 2018 Shu et al used SORS combined with micro-CT as a reference standard (110). Using the bone from 24-week-old mice, measurements were taken both on excised bone and transcutaneously. Using a PLS leave one out validation method a calibration was created of bone mineral density (BMD) and maximum torque. Both the SORS and excised

measurement performed similarly well on the BMD achieving a 20% root mean square error cross validation (RMSECV). Larger offsets did not improve prediction of BMD though they did improve the prediction of maximum torque applied through the three-point test.
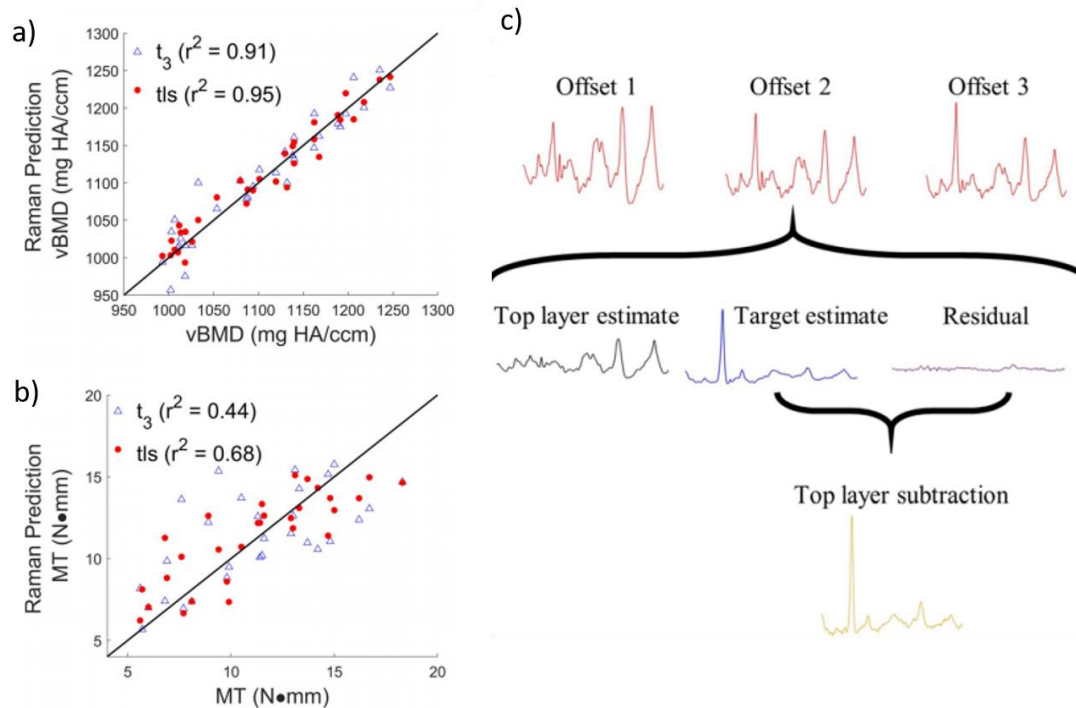
Figure 2.18 A) Cross validation results for BMD prediction as measured with micro-CT for the prediction model using just the target layer and the top layer subtracted spectra. B) Cross validation results for maximum torque prediction as measured with micro-CT for the prediction model using just the target layer and the top layer subtracted spectra C) A figure showing the spectra from three offset take, their decomposition into components and then how a top layer subtraction is created. (111)

In addition to multivariate techniques of spectral fitting, Chen et al reported a method of library fitting (111). Library fitting has been used in other applications where simple mixes of two or more unknown materials are present. By using an error minimisation function such as non-negative least squares the spectra from the library can be fitted to the recovered mixture. By finding the combination of spectra that best fit the spectrum of the mixture an accurate estimation of the components can be made (112). In the case of monitoring bone regeneration, there is a much narrower range of possible materials that need to be in the library. Berger et al showed that an over-constrained library can be used where the library

57

consists of two data banks (97). One data bank contains multiple spectra of bone and the other contains multiple spectra of soft tissue components that may be found in the sample. The multiple spectra are taken from a range of samples that should cover the extremes in variation in component concentrations that are likely to be found within the samples. By building a two-component fit using the library it is possible to accurately reconstruct the sample spectrum with some small residuals. Figure 2.18 shows that from this process three components are created, "top layer" consisting of soft tissue spectra, target layer of the bone, and the residual. Using the target layer spectra allowed the group to create a prediction model for both BMD and maximum torque (MT) (97).

The authors postulated that the residual may hold information that was not within the target estimate. This is because it is entirely possible that the library does not contain all the possible variations in enough possible combinations for the library fit to accurately account for all important spectra variations. To test this idea, they compared the predictive power of just the estimated bone signal to spectrum, referred to as (**t**), they referred to as top layer subtraction (**tls**), Figure 2.18c shows is the combination of the bone estimation and the residual. This **tls** was able to predict both BMD and MT more accurately than the bone estimation alone. Figure 2.18 shows both the **t** and **tls** prediction dataset where in the BMD prediction **t** the RMSECV was 23.4 mg/cm^3 and the **tls** RMSECV was 17.0 mg/cm^3. For MT the RMSECV were 2.64 Nmm and 1.97 Nmm for the **t** and **tls** respectively. This showed that adding the residual to the prediction model caused a significant improvement in prediction for real qualities of bone health (111).

3 Chapter 3

Instrumentation: design, development, and validation

3.1 Experimental design

The main aim of the thesis was to investigate whether Raman spectroscopy can be used for monitoring bone regeneration. The two main applications were: i) mineralisation of critical defect in large bones (Chapter 4); ii) development of the extracellular matrix in calvarial model (Chapter 5). To design a Raman spectroscopy system, it is important first to understand the samples that were measured as this affected the design process.

3.1.1 Types of samples

Bone growth and healing have multiple components that can be studied in many modalities. These conditions range from large bones such as the femur to subcutaneous scaffold inserts that will yield very low mineralisation levels (low concentration of HA). To make our system as applicable to biologically relevant samples as possible we started by working closely with members of the School of Pharmacy and School of Medicine, University of Nottingham. The first study investigated whether it was possible to measure the concentration of HA in a scaffold implanted in the head of a femur of a sheep. Phantom samples could then be built to simulate all stages during bone mineralisation following regeneration of a critical bone defect. The second study investigated the changes in soft tissue components using phantom and animal samples to ascertain whether it was possible to detect the early growth of collagen within a critical defect in a rat skull.

3.1.2 Phantom construction - an overview

A phantom sample is an object that is designed to mimic the optical properties of the target samples for imaging. These samples are designed to standardise the properties in a controlled way that allows for highly repeatable measurement to be taken using an imaging technique. This high degree of control of the sample means that the capabilities of the imaging system and data analysis can be evaluated.

In both studies undertaken we produced phantom samples of biological systems that were of interest to us. To build these phantoms it was important to understand the optical properties of the materials present in the systems they were mimicking (113).

3.1.2.1 Design considerations for skin and fat facsimiles in phantoms.

It is possible to mimic the optical properties of skin and fat in several different ways (114). One popular method involves mixing a gelatine base with different materials to match the optical properties of the target (114). There has been a fair amount of work done by people such as Pogue et al (115) where polystyrene micro beads were mixed into the material. The density of polystyrene beads needed for the correct optical properties had been characterised (115) as has adding fluorophores to mimic the background fluorescence in skin from sources such as blood (115). In the case of phantoms for optical experiments involving diffuse Raman there is another consideration: the relative Raman scattering cross-section and concentration of the chemical of the defect being investigated compared to the confounding factors such as surface layer skin.

For these reasons it was decided against these methods in favour of using a biological substitute. The substitute in the case of the sheep study was pig skin and fat that was taken from pork belly sourced from the local supermarket (Sainsbury's). Pork skin and fat was used for several reasons. First, the belly fat allowed us to cut a single sample that was up to 8 mm thick with skin attached. Second, the high levels of homogeneity in the fat layer of pork belly increase the reliability of the measurements taken through it and third, pork belly is much easier to source in large quantities and much cheaper than lamb skin. In the case of the phantom built to mimic rat skulls this was not an appropriate material and instead chicken skin was used as the skin and fat layer to mimic the skin covering the rat skull. The chicken skin was taken from the leg of a chicken as this was found to have the same thickness as the skin covering a rat skull (approximately 1 mm) (116).

3.1.2.2 Design considerations for bone facsimiles in phantoms.

As well as skin and fat, the next material that needed to be mimicked was bone. The first consideration of the bone phantom was that it was necessary to differentiate between the signal from defect and that from the surrounding bone. To facilitate this, a material with two characteristics was required - similar optical properties to bone, and a clearly differentiable Raman signal for hydroxyapatite (HA). Teflon fit both criteria (117) with the benefit that the largest peak at 734 cm^{-1} is at a lower wavenumber than the range of interest. This meant that Teflon could be used to build a phantom of the healthy bone surrounding the defect. When HA and collagen are added to these defects it is easy to

differentiate the signal that is directly from the defect using the chemical signature of those materials without needing to account for the signal that would be from the surroundings.

It was also possible to construct a phantom for bone that mimics the changing concentrations of mineral and extracellular matrix throughout the healing process. As discussed in section 1.2.2, the principal components of bone are collagen and hydroxyapatite. The concentrations change based on the phase of bone healing, with an initial growth consisting almost entirely of collagen and then later an increase in mineralisation which is mostly hydroxyapatite. By mixing powdered forms of both materials, it was possible to create samples that approximated the major spectral qualities of bone, in the 960 cm^{-1} phosphate peak for the HA and the majority of the collagen peaks as described in Chapter 2. These are not perfect analogues as there is no cross linking formed to create the collagen structures, the hydroxyapatite also is very pure and as such does not have the ranges of carbonate that causes the changes that are seen in the spectra that are discussed in Section 2.3. This could limit the ability of phantom studies when attempting to detect variables just as bone age or carbonate concentration within the bone.

3.1.2.3   Phantom design for the sheep model

Porous scaffolds of polycaprolactone (PCL) and HA were 3D printed to build phantom samples for mimicking the bone regeneration in a critical defect. The ability to print HA directly into the scaffold meant that it was possible to mimic mineralisation into the defect by increasing the concentration within the defect. This meant that healing pathways could be modelled and mimicked in a study.
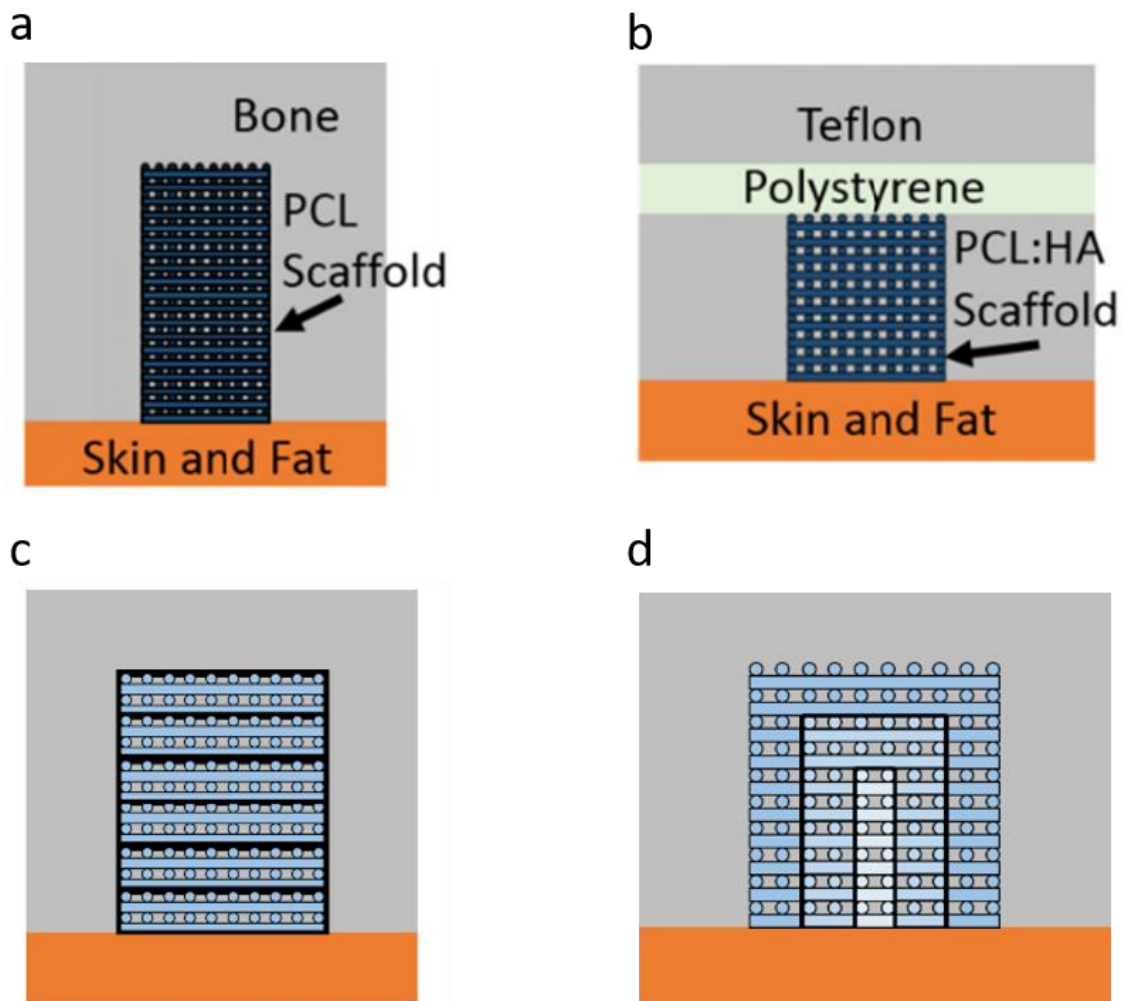
Figure 3.1 a) Schematic of a scaffold within a bone defect, b) schematic of the phantom mimicking the defect using Teflon as a bone replacement, c) configurations of the PCL/HA scaffold configuration for the depth profiling measurements, and d) schematic of the two PCL/HA scaffold configuration for the growth simulation measurements.

To create a phantom that would be suitable for testing the efficacy of the apparatus, a phantom that mimicked scaffold in a long bone, such as the femur, was built. This phantom design consisted of a 40 mm x 40 mm x 30 mm Teflon block with adjustable sides to account for some variance in the printing process of the scaffolds, Figure 3.1. The Teflon block was large enough to simulate the head of the femur or other similarly large mass of bone. The defect, which was a 10 mm x 10 mm x10 mm cube, mimicked the size of defect that was of relevance to the literature (44). The scaffolds were modular to allow use to easily test different configurations of scaffold and hydroxyapatite distribution. Two configurations

were used. A simple set of five 2 mm thick layers that allowed us to place a single HA doped layer at any desired depth between 4 mm and 12 mm from the surface to assess the depth penetration of our method. The second configuration created concentric layers to allow us to mimic the bone healing pathway.

3.1.2.4 Phantom design for the monitoring of collagen in a rat cranial defect

I used phantom samples and animal skulls to expand our investigation into the detection of collagen concentrations within bone, which are at a much lower concentration with a corresponding weaker Raman signal than skin and fat. For this reason, rat skull bone growth was investigated. Rat skull has a relatively thin layer of soft tissue that would generate a large amount of signal masking the important Raman signal from the defect. The defect was a 3 mm radius hole drilled into the centre of the skull. As the number of animals was limited, for the phantom, chicken thigh skin was used instead of rat skin as the thickness is similar, and a 1.5 mm thick Teflon sheet was used in place of the skull, with pork adipose tissue placed behind it to mimic the scattering effect of the brain. Figure 3.2 shows how the phantom and biological sample are similar. Where the light source is incident on the skin at the point directly under the centre of the defect.
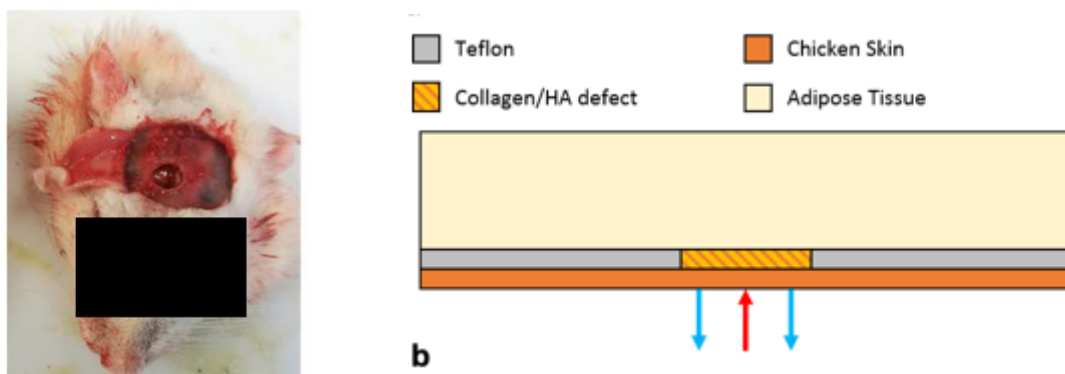
Figure 3.2 a) The defect shown in a rat skull with the skin peeled back for access to the space to add a sample. b) the schematic of the phantom used to mimic the rat skull. The red arrow indicates the excitation beam and the blue arrow indicated Raman signal collected at an offset from the exaction beam.

In the rat skull defect bone formation was mimicked in its two components, the soft tissue formation of the extracellular matrix with collagen powder and the mineralisation of bone using HA powder as our mineral source. By mixing these two powdered materials in a mould the concentration of collagen and HA within the defect was accurately controlled. The fine

control that this method allowed was used to create implants that mimicked the early, mid, and late stages of bone healing.

3.2 SORS Instrument design

3.2.1 Comparing SORS and inverse-SORS as a method for collecting spatially resolved Raman spectra.

The multiple collection points of SORS has the possibility to encode different spatial information in each collection point. The chemical and geometric composition of the sample directly between the excitation and collection point has the greatest effect. Figure 3.3 shows how the signal is distributed for a sample with multiple excitation or detection points. Figure 3.3b shows the signal at each collection point. The inv-SORS has a much larger total signal than any of the individual collection point of the SORS set up though there is only one measurement compared to twenty separate signals from each of the detectors for SORS.

Figure 3.3c and d both show how the signal from within the sample contributes to the signal at the detector for each pair of source and detector. Figure 3.3c shows the distribution for 4 of the detectors each at the cardinal directions, Figure 3.3d shows the single detector at the centre. Figure 3.3c shows there is a clear directional bias in signal towards the detector that is in line with the sample. This can be seen in Figure 3.3b where the four detectors are labelled with the signal each point detects. This distribution of signals can give a strong indication of the direction of the region of interest (ROI) from the excitation point.

Figure 3.3 d shows that there is a clear bias in the distribution of light generated in inv-SORS the single detector has no way of focusing in on this direction as only a single point measurement has been acquired. This means that each individual inv-SORS reading lacks directionality.

In terms of raw signal, Figure 3.3b shows that the signal at each SORS collection point is significantly weaker than that of inv-SORS, ranging from at most 0.255 to 0.000424 (to 3 sig. fig.). This means that an inv-SORS measurement has the potential to be much faster if only a single measurement is needed. This faster measurement speed could allow for multiple inv-SORS measurements with different centres to be taken and used to triangulate the position of the ROI. SORS can achieve the same result by summing the spectra from each offset.

64
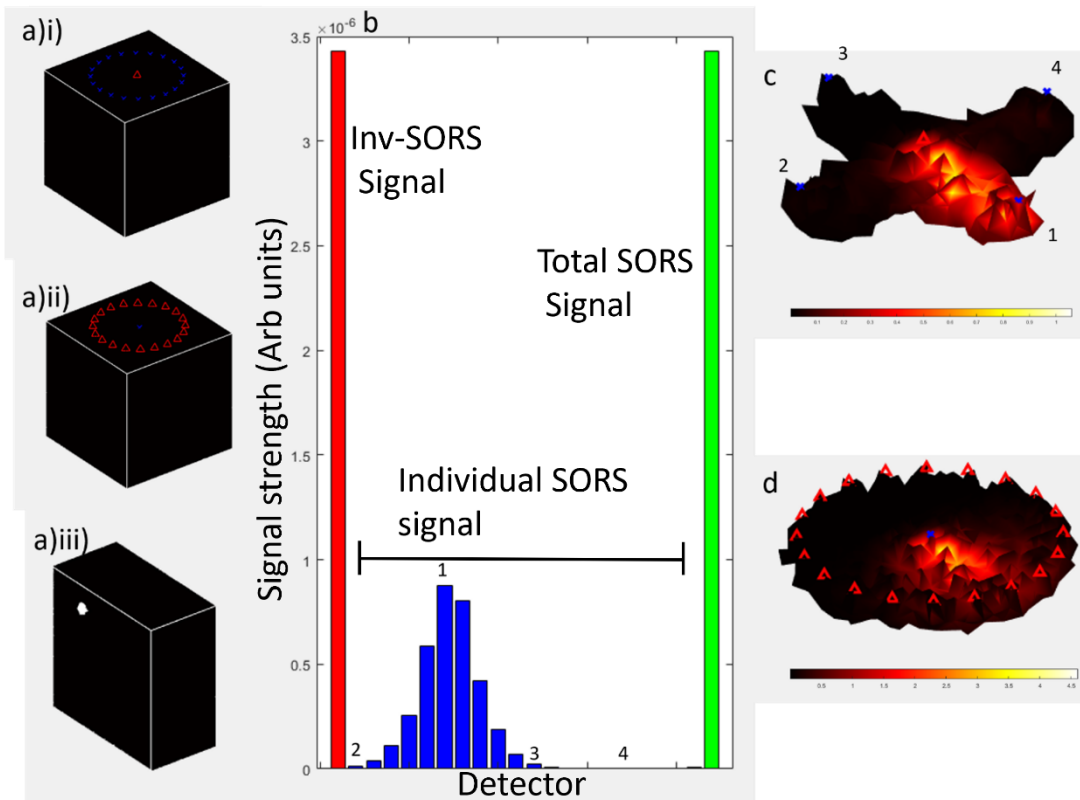
Figure 3.3 : a)i) A 20x20x20mm sample with a SORS configuration, the red triangle is the excitation point and the blue triangles are the collection points. ii) A 20x20x20mm sample with an inv-SORS configuration. The red triangles are the excitation points, and the blue triangle is the central collection point. iii) A cross section of the sample along the y = 0mm plane which shows a region of interest in white against a background of the black material. b) A bar graph showing the log of the signal from the ROI at each of the collection points for SORS (blue), inv- SORS (red), and the summation of all the blue spectra (green). c) Distribution of the nodes that contribute at least 10% of the signal from the region of interest for the SORS set up. d) Distribution of the nodes that contribute at least 10% of the signal from the region of interest for the inv-SORS set up.

3.2.2 DMD-based SORS

For this study, a digital micro-mirror device (DMD)-based SORS was developed. The DMD allows rapid reconfiguration of spatial offsets. This flexibility in setting the spatial offsets enables optimisation of the choice for light collection points for each of the samples included. The DMD-based system uses the projection of the sample plane onto a digital

micro-mirror display (DMD). This display allows us to select in software the points of the sample that will be projected onto the spectrometer with all other light diverted to the inspection camera. It is the lenses between the sample and the DMD that affect the magnification and efficiency of the system.
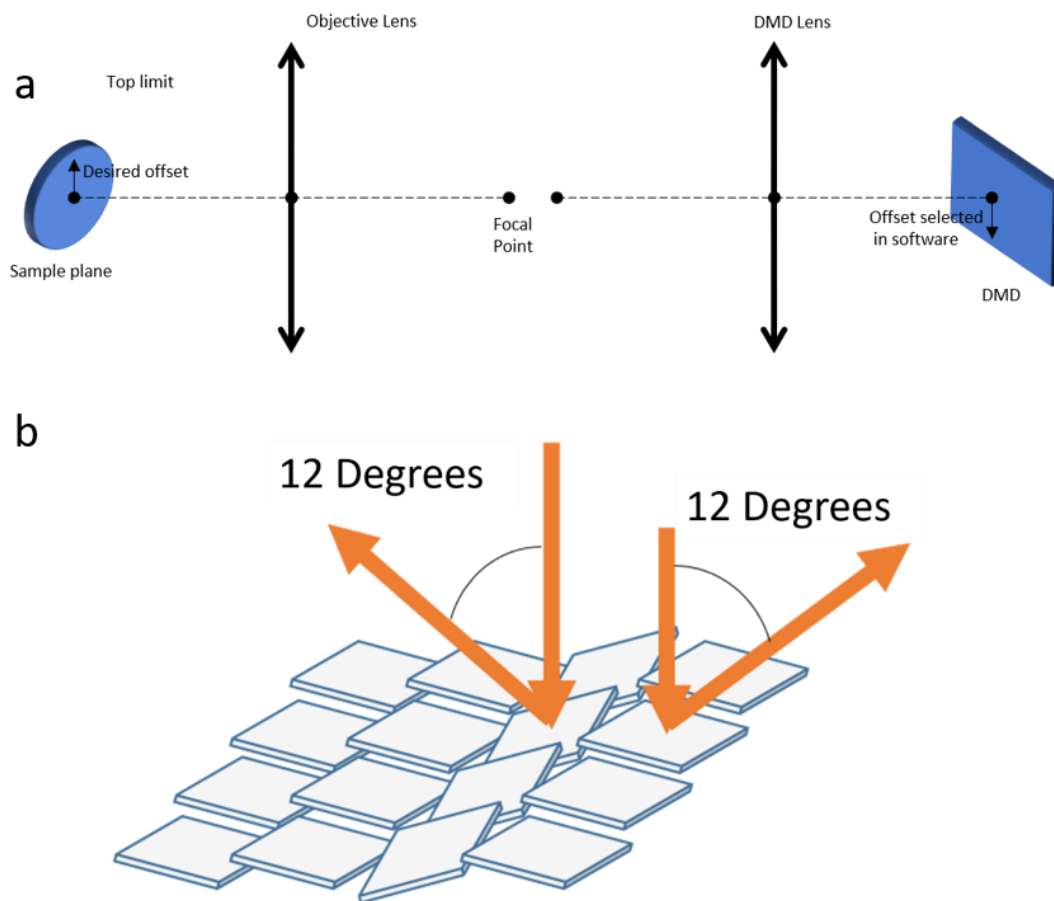
Figure 3.4 a) A schematic of the sample plane and DMD shown with focusing lens. b) A graphic demonstrating the configuration of the mirrors in a DMD with the laser direction selection demonstrated

Figure 3.4a shows the most basic principle of a DMD based SORS system, both the sample plane and the DMD have a focusing lens set so that they are each at the focal point of the lens. Therefore, the sample plane will be projected directly onto the DMD which will allow for a one-to-one mapping from the sample to the DMD. This means that selection of a point (micromirror) at the DMD will select a single point on the sample. In this way offsets can be selected dynamically.
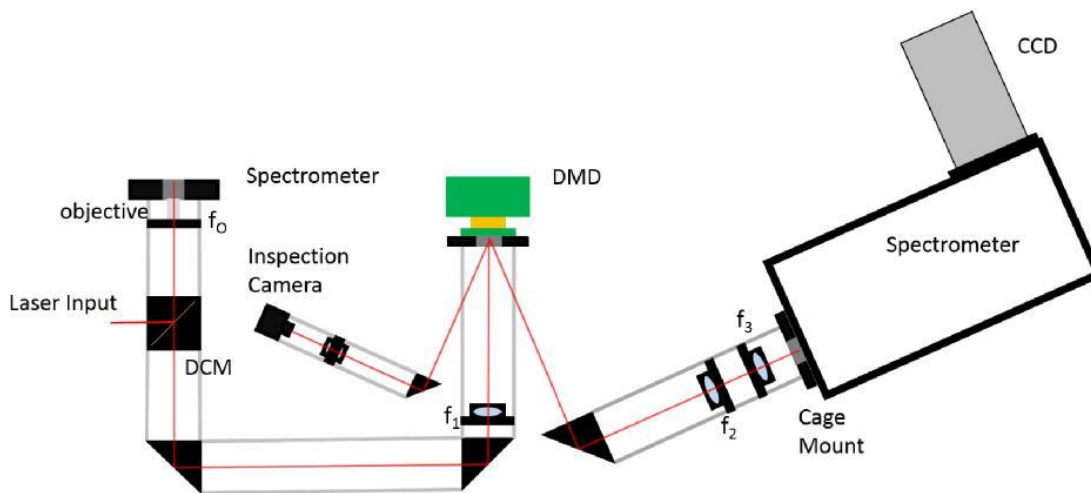
Figure 3.5 The spectrometer set up used to acquire the results discussed in later chapters.
DCM is the dichroic mirror, f_0-f_3 are the four lenses used in the system. Diagram is not to
scale.

Figure 3.5 shows a schematic of the experimental set up. It starts with the excitation laser
that is reflected to the sample by a dichroic mirror and focused on the sample by the
objective lens f_0. The light is then collected by the same lens and is parallel through the
dichroic mirror and on through two mirrors to be focused by the lens f_1 onto the DMD. From
there the DMD selects the reflection direction to direct either to the inspection camera,
where the light is focused by the secondary lens, or towards the spectrometer. The signal
that is reflected towards the spectrometer is collected by the lens f_2 and then is refocused
into the spectrometer by lens f_3. All of this is mounted on Thorlabs cage mounts. The set up
was built entirely around the DMD to achieve a highly adaptable system with which the user
could dynamically change the collection point configuration in software.

3.2.3   Instrument design

To make informed decisions about the correct choice of components, it is important to
understand the underlying theoretical elements that determine the performance of the
instrument.

A DMD based system relies on the projection of the sample surface onto the DMD to select
the collection points. The magnification of this system is then:

$$m = {f_1}/{f_0} \qquad\qquad [3.6]$$

where f_1 is the focal length of the lens focused on the DMD, f_0 is the focal length of the objective lens, and m is the magnification. This gives a linear relationship between the position of the collection points on the DMD, and the offset selected at the sample. This Equation is:

$$\Delta x = S\,{f_0}/{f_1} \qquad\qquad [3.7]$$

where S is the distance of the collection point from the excitation point on the DMD and Δx is the offset at the sample. In this way the lens selected is governed more by the size of the DMD and the desired offset than maximising spatial resolution.

Larger optics were favoured for this set up for several reasons. To achieve larger offsets, it is necessary to increase the focal length of the objective lens, f_0, as seen from Equation 3.7. With very large offsets field of view must also be accounted for which forces even larger focal lengths. A larger lens helps to collect more of the light from the sample which is particularly useful with larger focal lengths. Another problem to solve with DMD-based SORS is the long path length of the laser which leads to the loss of light as not all the light is collected and focused onto the DMD by the lens f_1. The Equation for the relationship between offset of a collection point angle the parallel light makes to the normal of the lens is:

$$\Delta x = f_0 \tan(\theta) \qquad\qquad [3.8]$$

where θ is the angle the light makes with the normal of the lens. Since the path length is often a significant distance relative to the angle, light is lost due to the light not fully overlapping with lenses in the beam path.
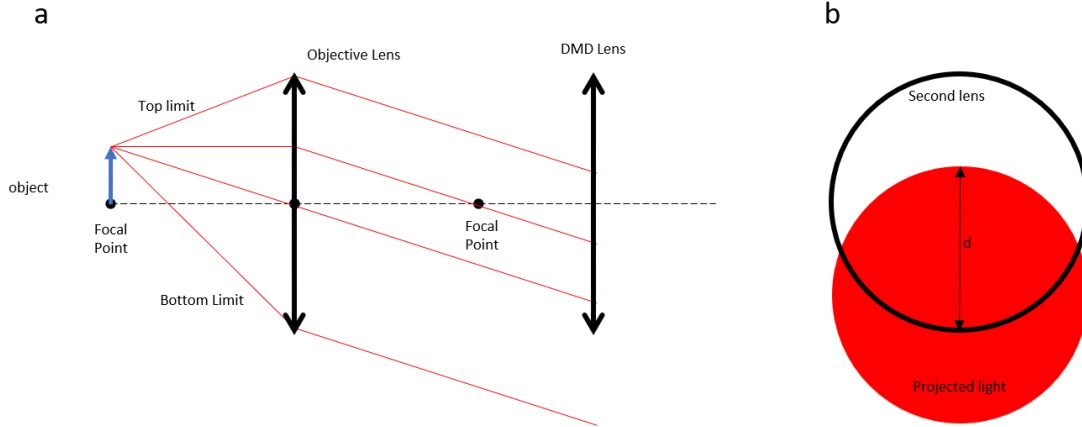
Figure 3.6 a) A line diagram showing the path of light from a point on the focal plane offset from the centre through an objective lens to the lens that focuses onto the DMD. The focal points shown are for the objective lens. b) The overlap between the second, DMD, lens and the light that is collimated by the objective lens.

Figure 3.6 demonstrates that even though an offset may be within the field of view of the optical system design the lens choice has led to a large loss of light and therefor a low efficiency for the system. Increasing the lens size increases the efficiency. The amount of overlap that the light from a certain offset is calculated at:

$$d = 2R - L_{path}\tan(\theta) \qquad [3.9]$$

where d is the overlap as shown in Figure 3.6b, R is the radius of the lens, and L_{path} is the distance between the objective lens and the DMD focusing lens as shown in Figure 3.4. From the overlap, assuming the light from the first lens and the second lens are both circles of equal size the amount of overlap between the two is:

$$A = 2R^2 \cos\left(d/2R\right) - d/2\sqrt{4R^2 - d^2} \qquad [3.10]$$

where d is the overlap between the area of the lens, and A is the projected area of the sample plane. The ratio of A to the total area of the lens used is the amount of light that is transmitted in an ideal set up with a uniform flux across the entire area of the lens.
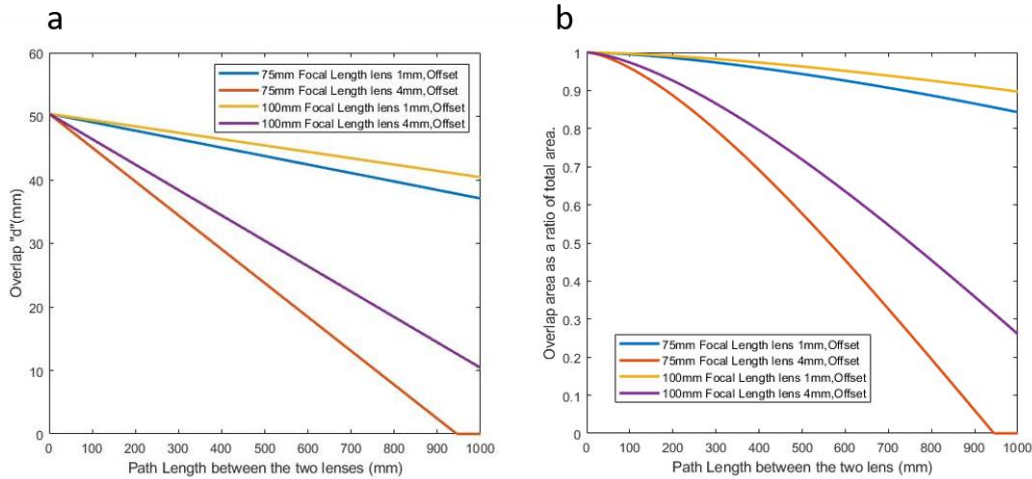
Figure 3.7: a) Overlap of the two areas against path length for lenses with different focal lengths and offsets, and b) the proportion of light that is collected by the lens when the centre of the projected area is offset by a distance d.

Figure 3.7a shows that for any given focal length lens the overlap decreases as path length increases. It also shows that increased offsets also increase the rate that the overlap decreases with increased offset. This comes from Equation 3.8 where a larger offset means a larger angle for the parallel light. Figure 3.7b shows the overlap between the projected light and the second lens as a ratio of area of overlap against area of total. As this is dependent on *d*, equation 3.10, an increase in path length decreases the total area of the overlap. Figure 3.7b also shows that larger offsets lose signal at a significantly steeper rate than smaller offsets.

The objective lens and the DMD lens in our setup were set 1000 mm part. This length allowed us to use the full range of the DMD within the field of view of a 100 mm focal length objective lens. Using the small angle approximation with a 2-inch (50.4 mm) diameter lens, a 75mm focal length objective lens, and a 5 mm offset there is no overlap between the projected light and the DMD lens, which means no light is collected.

Two other factors in the efficiency of the system should be considered: the numerical aperture of the objective used, and the detection pattern on the DMD. The effect of the numerical aperture of the objective lens affects the solid angle of light collected. Since all lenses used in our experiment were diameter 50.4 mm diameter set into a Thorlabs cage, the shorter the focal length the higher the percentage of light was gathered.

With a DMD setup the collection area can be maximised by drawing a full semicircle of collection points around the circumference of a circle with radius Δx. This means that the collection surface area can be approximated very closely as:

$$A = w\pi\Delta x \qquad\qquad [3.11]$$

where w is the width of the collection annulus, and A is the area of the collection annulus, so there is a linear increase of collection area with increase in offset. In a perfectly symmetrical geometric configuration signal collected will be proportional to the collection area as the light will scatter the same distance from the excitation point, through the ROI and to the surface where it will be emitted in a uniform manner. It should be noted though that if this symmetry is broken, by having the ROI closer to one part of the annulus than the rest, the signal from the ROI will not increase proportionally with additional collection area. Since symmetrical samples are very common, and both of our studies focused on samples with a high degree of symmetry, this is still an important factor.

By combining all these factors together, it is possible to estimate the efficiency of different setups. By comparing the efficiency of each setup across the width of offsets that they allow the user can make decisions on the choice of objective lens for a given sample, once the desired offsets are known.

With the width of the DMD being 8.8 mm, to fit both the 0 mm offset and the theoretical maximum on the same configuration the minimum focal length of the DMD lens must be 175 mm. This value was reached by rearranging Equation 3 to get:

$$f_1 = {S}/{\tan(\theta_{max})} \qquad\qquad [3.12]$$

where f_1 is the lens at the DMD, S is the offset on the DMD, and θ_{max} is the maximum angle that the Raman signal from lens f_0 can be incident to the lens with an overlap. By substituting the known size of the DMD and maximum angle θ_{max} from the known path length and Equation 4 a lower bound for was f_1 calculated. This distance is just smaller than the minimum focal length that can be used when considering the physical constraints on the arrangement of two lenses focused on the DMD. Thus, a DMD lens (f_1) with 200 mm focal length was selected. By aligning the 0 mm offset point to close to the edge of the DMD, the

largest spatial offset achievable with a 100 mm focal length objective lens (f_0) was 4 mm. Below is a table for some important landmark offsets and the relative loss due to offsets at each off the lens.
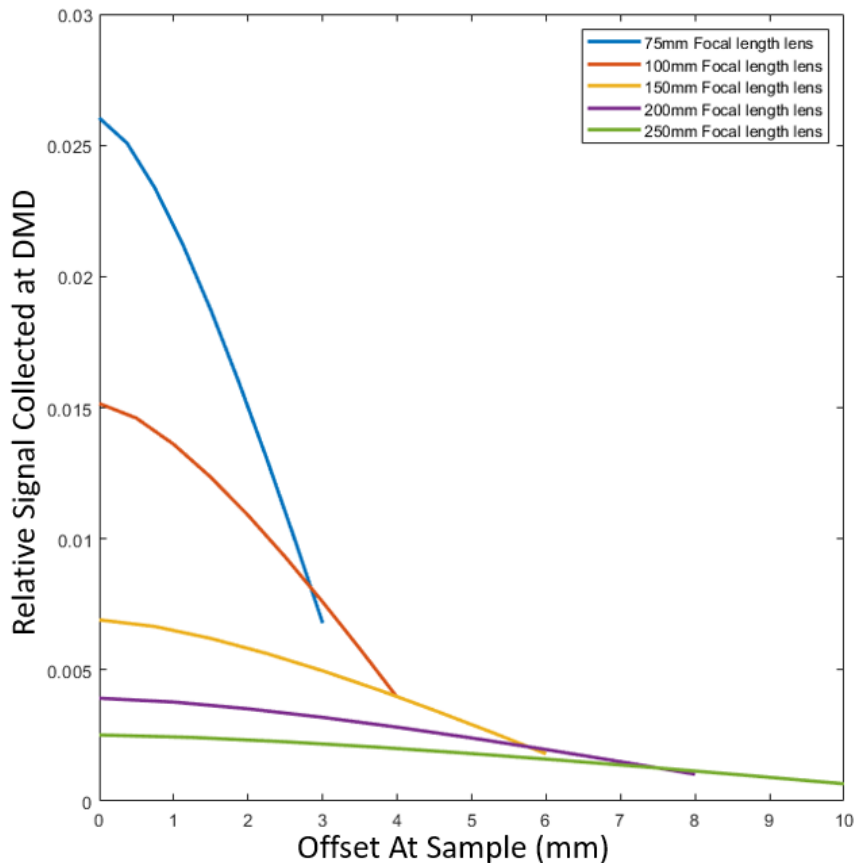
Figure 3.8 Each line corresponds to the relative signal collected using a given lens compared to the maximum signal that is emitted from the surface of a sample. Each lens (f_0) are paired with a DMD lens (f_1) of focal length 200 mm.

A contribution not calculated for the table but that must be considered is the configuration of detection points. The main strength of the DMD shows itself here by allowing the change of the configuration of detection points during a set of measurements. With a larger offset there is a relative gain in the number of detection points that can be placed along this radius, which helps to counteract the signal loss from light diffusion in the medium as shown in Equation 3.11. Since the collection point in each vertical position can be changed

independently it is possible to counteract this disparity in signal collected by biasing the selection of offsets toward those offsets that lack signal. If the measurement of multiple offsets is done concurrently a higher proportion of the channels can be dedicated to the larger offset over the course of the integration time.

Lens	S = 0mm	S = 2mm	S = 4mm	S = 6mm	S = 8mm
75mm	$\Delta x = 0$ $\varepsilon = 0.0260$	$\Delta x = 0.75$ $\varepsilon = 0.0234$	$\Delta x = 1.5$ $\varepsilon = 0.0187$	$\Delta x = 2.25$ $\varepsilon = 0.0130$	$\Delta x = 3.0$ $\varepsilon = 0.0068$
100mm	$\Delta x = 0$ $\varepsilon = 0.0152$	$\Delta x = 1$ $\varepsilon = 0.0136$	$\Delta x = 2.0$ $\varepsilon = 0.0109$	$\Delta x = 3.0$ $\varepsilon = 0.0076$	$\Delta x = 4.0$ $\varepsilon = 0.0040$
150mm	$\Delta x = 0$ $\varepsilon = 0.0069$	$\Delta x = 1.5$ $\varepsilon = 0.0062$	$\Delta x = 3.0$ $\varepsilon = 0.0050$	$\Delta x = 4.5$ $\varepsilon = 0.0035$	$\Delta x = 6.0$ $\varepsilon = 0.0018$
200mm	$\Delta x = 0$ $\varepsilon = 0.0039$	$\Delta x = 2.0$ $\varepsilon = 0.0035$	$\Delta x = 4.0$ $\varepsilon = 0.0028$	$\Delta x = 6.0$ $\varepsilon = 0.0020$	$\Delta x = 8.0$ $\varepsilon = 0.0010$
250mm	$\Delta x = 0$ $\varepsilon = 0.0025$	$\Delta x = 2.5$ $\varepsilon = 0.0023$	$\Delta x = 5$ $\varepsilon = 0.0018$	$\Delta x = 7.5$ $\varepsilon = 0.0013$	$\Delta x = 10.0$ $\varepsilon = 0.0007$

Table 1 A table of the offset and theoretical efficiency at a sample of values for offset at the DMD (S) for selection of 2-inch lenses that were available to us. The "Lens" column shows the focal length of the objective lens used "S" is the distance on the DMD, Δx is the offset at the sample and "ε" is the proportion of Raman signal that leaves the surface of a sample that readings the DMD.

Combinations of different offsets can be used to maximise the effective signal from each of the offsets of interest. Each larger offset allows for a larger number of collection points placed along the circumference of the arc drawn at that radius which means that total light collected does not drop off as quickly in DMD-based SORS as it does in single illumination and detection-based SORS.

3.2.4 Comparing different configurations of collection points drawn on the DMD

Signal to noise ratio is a key factor in the quality of Raman spectra. Due to the attenuation of light that occurs between the excitation and collection point, raw signal is often much weaker in SORS than conventional Raman spectroscopy, so multiple different methods are employed to increase signal to noise ratio. Circular SORS utilises a ring of detectors to increase the detection surface area. The signal from these collection points is summed to create a single spectrum with greater signal. In a DMD-based signal each offset can be measured repeatedly with only collection points that correspond to a single offset used for each Raman measurement.
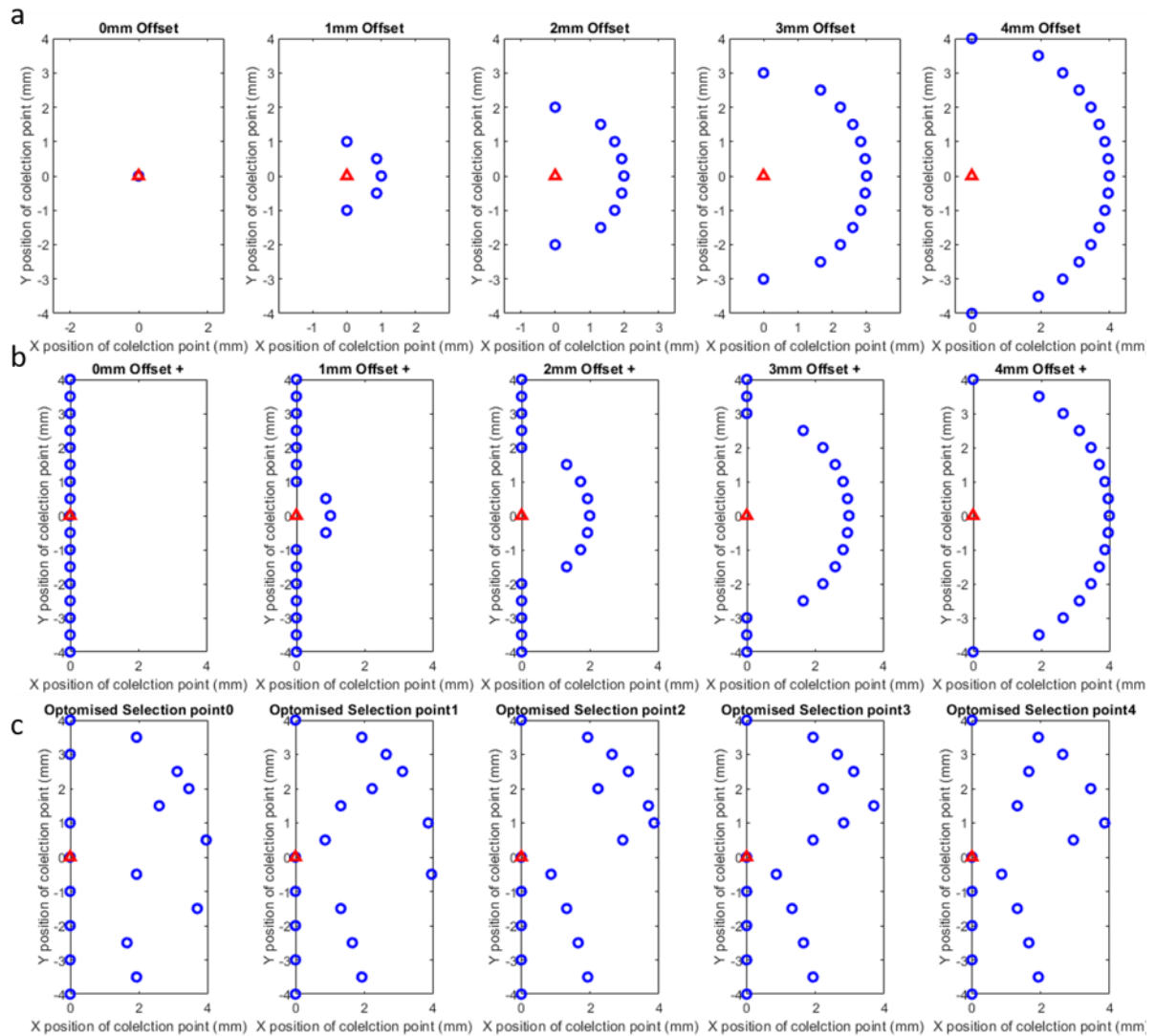
Figure 3.9 a) The configuration of points where only the collection points for a given off of 0mm to 4mm where turned on, red triangles are the point of excitation and blue circles the collection points, b) the configuration of points where each channel that can be used for a given offset is used and all the other unused channels are turned on, c) The configuration of collection points that were chosen to most evenly distribute the signal collected at each offset

Different offsets will have different signal strength that will depend on the scattering properties of the sample material. The major strength of DMD-based SORS is its programmability and flexibility. An approach to signal collection was therefore posited where collection point distribution would be selected to improve the signal to noise ratio, **Error! Reference source not found.**.

74

Error! Reference source not found.a shows that the smaller offsets do not completely fill the possible space on the CCD due to the maximum height above the centre point being limited to the offset currently being measured. Since the entire CCD is always on, it is possible to gain time by filling as much of the vertical space as possible with larger offset while smaller offsets are also being measured. **Error! Reference source not found.**b shows that these channels can be always left on to collect more signal. From there it is possible to optimise the use of the extra channel by taking the theoretical signal gathered at each collection point and selecting a set of configurations create the signal profile that is desired. In the case of **Error! Reference source not found.**c the collection points were selected to be
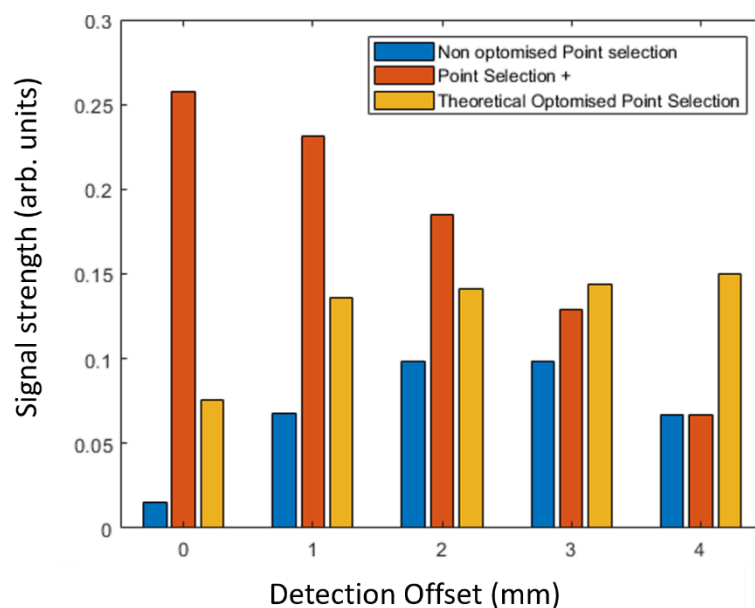
most evenly distributed across all five offsets.

Figure 3.10 A bar chart showing the relative signal collected for each offset distance from 0mm to 4 mm for the three different configurations from figure 3.9, a, b, and c when the sets of points are taken as a whole.

Figure 3.10 shows that significantly more signal is collected for all the offsets apart from the largest when the extra channels is used. This value was greater than double. This shows that utilising the extra channels can not only increase signal gathered, which will decrease integration times, but also increase the specificity of the configuration to the sample that was being measured. It was this method that was carried forward into the second paper (118) where detection of collagen would pose a far greater challenge than the hydroxyapatite detection of the first paper. This method also opened the possibility of hand crafting patterns or dynamically changing the offsets based on incoming data from earlier.

This could be weighted towards certain offsets, for instance increasing the signal to noise of the 0mm offset collection point would give sharp and clear spectra to be used as subtraction see (Chapter 4).

3.2.5   Choice of laser wavelength

The choice of laser wavelength illustrates the inherent trade-off for Raman spectroscopy in biological materials. The longer the wavelength the lower the fluorescence background is generated. This increases signal to noise ratio of the Raman spectra and reduces the chance of mathematical errors in background subtraction. As discussed in Chapter 2, however, the intensity of Raman light is inversely proportional to the fourth power of the excitation wavelength (Equation 2.2) this means that significantly less signal is generated as the excitation wavelength increases. Balancing these two factors becomes the first question when a new Raman system is being built, where the materials that are to be studied will guide the selection of excitation wavelength. In systems where high spatial reposition mapping is important, such as those systems involved in cell studies, the diffraction limit is also a consideration.

In previous work by our group a 532 nm laser had been used as the excitation source (101). While these 532 nm lasers are used often in Raman spectroscopy, they have limitations in their application to biological systems. Most tissue is highly fluorescent under excitation with green light and throughout most of the visible spectrum with the fluorescence decreasing into the NIR and IR wavelength range (119). For this reason, 1064 nm lasers would seem to be a promising solution when fluorescence is the main source of noise. These systems are still more expensive and lower efficiency than VIS -NIR due to the low demand for these systems in general, though advances are being made. The significant reduction in signal for increasing the wavelength of the excitation beam caused by the dependence of Raman intensity on excitation wavelength is also a significant barrier to the use of very long excitation wavelength sources. For these reasons 785 and 830 nm wavelength lasers remain the predominant lasers used in the biological setting (119).
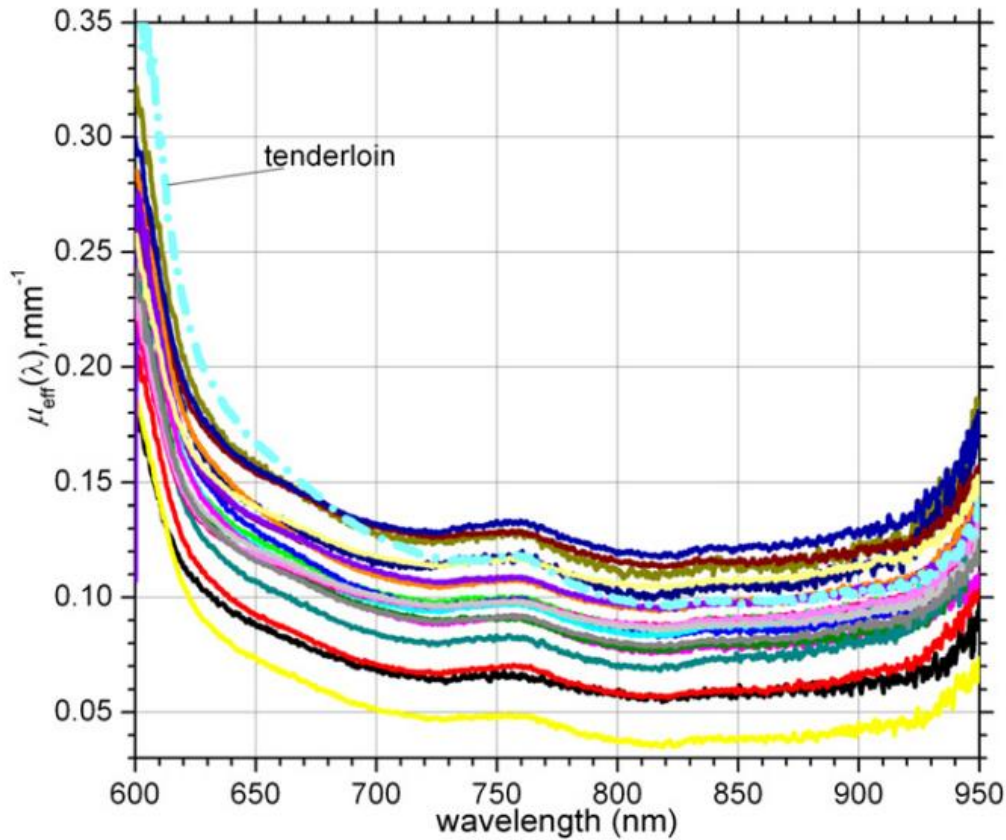
Figure 3.11 The scattering coefficient of multiple samples of tenderloin across the NIR wavelength, each plotted line represents the scattering coefficient of a different sample. (120)

The absorption profiles of porcine tissue (120) present in Figure 3.10have minimum values at approximately 830 nm. While it is tempting to select this wavelength for the Raman spectrometer, the distribution of the shift of the Raman photons across the fingerprint region need to be considered, along with the relative importance of each of those peaks. Our range of interest is roughly 700-1660 cm^{-1} with the main collagen bands in the 800-900 cm^{-1} region, the phosphate peak from hydroxyapatite at 960 cm^{-1}, and the CH_2 and $C = C$ stretch from proteins and fats at 1450 cm^{-1} and 1660 cm^{-1} being the most important bands.

Peak Shift	Wavelength with 785nm Excitation	Wavelength with 830nm Excitation
700cm⁻¹	830	881
800-900cm⁻¹	837-845	889-897
960cm⁻¹	849	902
1450cm⁻¹	885	943
1660cm⁻¹	900	963

Table 2 A table comparing the wavelengths of important Raman peaks for biological samples with 785 nm and 830 nm wavelength.

Table 2 shows that the 785 nm excitation bring most of the fingerprint region into the lowest range of scattering coefficient. While the laser itself will be more attenuated it was judged that this wavelength would offer a good compromise between Raman signal generated within the sample, attenuation of that signal, and efficiency of the camera. This is close to the 790-810 nm range suggested by Matousek and Stone in their paper discussing the effect of wavelength on signal in diffuse Raman (119).
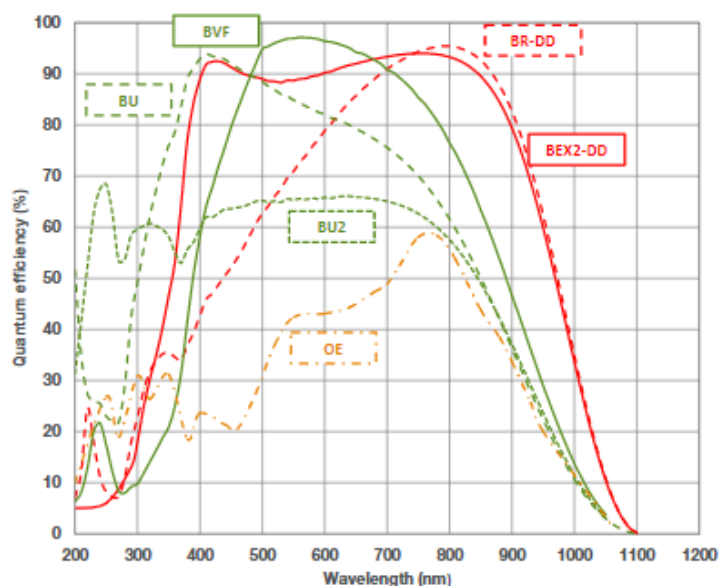
Figure 3.12 The quantum efficiency of a number of CCD coatings available from Andor, a supplier of spectrographic CCDs (121).

Another factor is the quantum efficiency of the camera at detecting the photons across the spectrum. These values are published by the CCD production companies and different

coatings can be used to increase the efficiencies at different wavelengths. The iDus 420 is a typical camera for the NIR range and comes with a selection of coatings. Above is the quantum efficiency graph of this camera across the UV-VIS-IR spectrum from the Andor website (121). Figure 3.11 shows that quantum efficiency drops rapidly beyond a wavelength of 900 nm.

Given that the goal of this PhD was to develop a Raman spectrometer optimised to investigate biological samples, a longer wavelength laser would be preferable. In our case we also must consider the scattering properties of our materials at the wavelength of our laser and our Raman signals. It has been shown that Raman signal through a material is proportional to the reciprocal of the absorption (120). Maximising total signal will then be a balance between a number of factors including the reductions in signal from the fourth root of the wavelength, the quantum effect of the DMD, the quantum effect of lens and spectrometer, and the absorption profile of the relevant materials.

3.2.6   Choice of Offset range.

One of the benefits of our DMD-based SORS design is that the instrument can be tailored to match the properties of the phantom sample investigated in this project. In each case, different spatial dimensions of the region of interest (ROI) will affect the choice of offsets. Deeper regions of interest benefit from larger offsets while ROIs closer to the surface can potentially benefit from smaller offsets. Equation 3.8 shows that our choice of objective lens is what allows us to change our range of accessible offsets, as well as the efficiency at these offsets. For the first the ROI was at a depth of 4 – 14 mm. For this an objective lens with focal length of 100 mm was selected which allowed for a central excitation and up to 4 mm offset. This was done to maximise the signal collected within the range of offsets and to allow a large range of selectable offsets. Figure 3.12 shows that the signal that could be gathered with this lens was significantly greater than the signal with larger focal length lens as well as collecting more signal at 3 mm and 4 mm offsets than the shorter focal length lens. The experiment focused on a sample with a cubic side length 10mm. This means that a 5 mm offset would be on the boundary between the defect and the bulk Teflon. As the goal is to maximise signal from the defect, it was decided that an offset greater than 4 mm was not necessary.

For the second experiment, which focused on collagen concentration in calvarial defects in rat skulls, a cylindrical defect of 3 mm radius and 1.5 mm depth beneath approximately 1.5 mm of chicken skin. For this reason, much smaller offsets were needed, from 0-1.5 mm with 0.5 mm steps. The selection of 1.5 mm as the maximum offset was based on experience with the initial paper and borne out by the fact that only minimal improvements were seen. To maximise the signal at these smaller offsets the smallest lens, which was the 75 mm focal length, was selected. This decision was based on the work done in section 3.2.3 (including Figure 3.6). The smaller offsets also meant that projection from the sample to the DMD could be aligned so that the excitation point was at the centre of the DMD allowing a full semicircle to be collected at each offset, improving the total signal. As with chapter 4 another consideration was the edge of the defect. As the rat sample did not have a phantom bone signal there was risk that the already present healthy bone signal might obscure the changes in signal caused by concentration difference within the defect. An offset of 2 mm that was inaccurately centred by only a millimetre would overlap with the healthy bone, significantly affecting the detected concentrations of HA and collagen.

3.3   Instrumentation Development

The Raman instrument was based on an inverse microscope setup with a DMD-based SORS system to allow easy mounting of the samples. A 785 nm laser was selected for excitation. Lenses that were 50.4 mm in diameter were selected as objective lenses in order to maximise field of view in the focal plane at the sample. 50.4 mm optics were utilised throughout the whole system to maximise light collection and throughput and fit into the 60 mm Thorlabs cage to allow rapid prototyping. It is important to note that while a 25.4 mm diameter lens with half the focal length has the same numerical aperture (NA) and therefore the same amount of light collected, the use of such a lens halves the maximum offset that can be reached as offset is dependent on the ratio of the two lenses f_0 and f_1 (Equation 3.7). It was the physical constraints of the DMD-based system that affected the choice of focal length more than light detection concerns.

The length of the beam path between the objective and f_1 is approximately 1 m. f_1 and f_2 are both 200 mm focal length lenses. A 200 mm focal length lens was selected due to the geometric limitation caused by the DMD. The DMD had a set switching angle of ±12 degrees and our optics size meant the limit on the minimum focal length that was possible for f_1 and

f$_2$ was just under 200 mm. The final selection of the focal lens of these lenses was based on several factors, from the size of the DMD to the range of desired offsets. It was calculated that a 200 mm focal length was a good choice. The DMD was an 8.8 x 14.4 mm rectangle with square, 7.84 x 7.84 μm mirrors that tilted along their diagonal axis. The mirrors have a binary position of ±12° which can be switched to direct light either to the inspection camera or towards the spectrometer. This DMD was selected as it was one of the larger DMDs on the market that had sufficient surface area. The array is treated by the computer as a 1960 x 1080 resolution screen with each of the mirrors acting as a pixel. By placing the focal plane of the lenses f$_1$ and f$_2$ on the DMD the selected points of the DMD can be used as a programmable slit for the spectrometer.

Given the known size of the DMD and the spectrometer light port Equation 3.6 was used to select a focal length for lens f$_3$. A 75 mm focal length lens was used to adjust magnification to the spectrometer to maximise the usable surface area of the DMD while still utilising most of the channels of the spectrometer. Given the 45° reflection axis of the mirror the DMD had to be mounted at a 45° angle to keep the beam path horizontal to the work bench. Each group of mirrors directed towards the spectrometer acts as a programable pinhole where the pattern on the DMD mimicked the light selection ability of a mechanical pinhole at the spectrometer light port.

The size of the pinhole will affect the total light collected, spectral resolution, and spatial resolution. The effective size of the pinhole is:

$$W_{pinhole} = \frac{f_3}{f_4} W_{DMD} \qquad [3.13]$$

where $W_{pinhole}$ is the width of the slit at the pinhole, W_{DMD} is the width of the point drawn with the DMD, f_3 is the focal length of the lens at the DMD, and f_4 is the focal length of the lens at the spectrometer entrance. The light collected is proportional to the area of the collection point. There is a minimum size of collection point that will not yield greater resolution but will continue to reduce light throughput. This is because of factors such as the spectral resolution of the spectrometer due to internal focal lengths, gratings, and CCD choice. Spatial resolution at the sample is also reduced with larger collection points as they gather light from a larger area of the sample.

Because the DMD has a 12˚ reflection angle, it is not possible to align the DMD, the sample, and the spectrometer so that they all lie in the same focal place. This means that the light from the offsets that are set further horizontally will end up being slightly out of focus on the CCD. A compromise is to place the DMD and sample on the same focal plane with the spectrometer placed in such a way that the CCD still ends up perpendicular with the laser path. This means there is a direct projection of the sample onto the DMD which vastly simplifies the calculations required to work out offset on the sample from the offset of the DMD. The effect of the out of plane alignment will affect the resolution of the system as the laser point moves further horizontally from the centre of the beam.

3.4 Validation of the device of simple samples

3.4.1 Two-layer system

The simplest form of sample that is investigated with SORS is a two-layer sample. These samples are often used to measure the ratio of surface and subsurface signal measured by a particular offset. Applications that mimic this kind of sample range from pharmaceuticals where SORS can be used to measure drug purity through packaging (122) or detecting the quality of blood stored in transfusion bags (123). Figure 3.13a shows a typical two-layer sample where a thin surface layer covers a bulk of material. The excitation and collection points are at the surface of this layer.

Figure 3.13b shows the spectra recorded from fifteen offsets, from -6 to 8 mm, for the two-layer system shown in Figure 3.13a with a surface layer thickness of 3.0 mm. The spectral feature assigned to the bulk material was polystyrene and the surface material was Teflon.
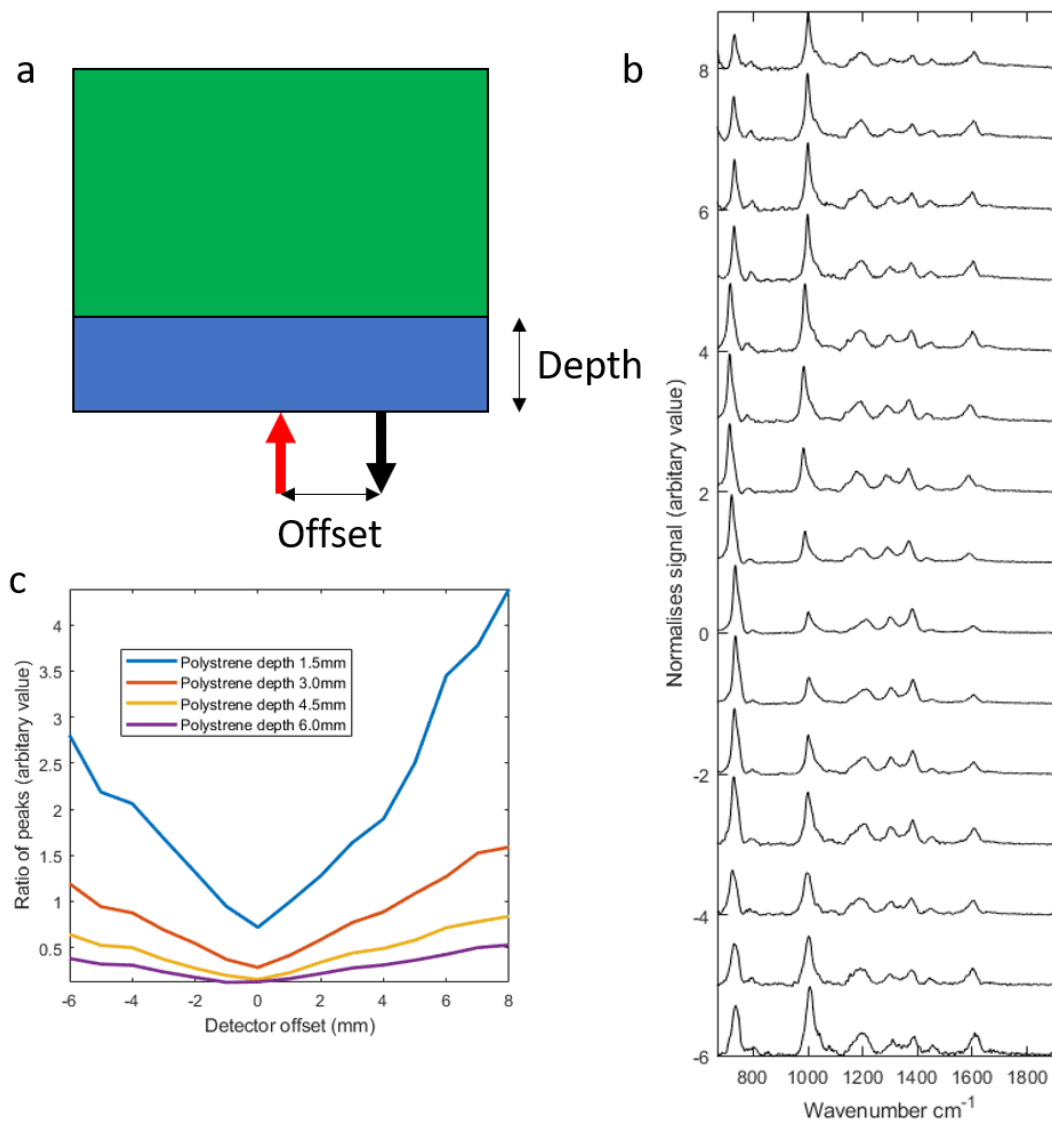
Figure 3.13a) A schematic of a two-layer system showing how the offset between excitation and detection points and depth are determined, the green layer is polystyrene, and the blue layer is Teflon. The red arrow is the excitation laser and the black arrow is Raman signal collected from a point on the surface. b) The spectra for a sample of depth 3.0mm from detectors from -6mm to 8mm offset at 1mm intervals. The numerical values on the y-axis shows the offset position. c) The ratio of the signal from polystyrene and Teflon at different depths.

In Figure 3.13b the peak at 734 cm^{-1} was assigned to Teflon and the 1001 cm^{-1} peak was assigned polystyrene. To measure the contrast in signal between the two materials the ratio of the peak intensities was plotted with respect to offset. Figure 3.13c shows this ratio of peaks for multiple thickness of surface layer:

$$Ratio = {I_{1001}}/{I_{734}}$$

where I_{734} and I_{1001} are the areas under the peaks, in photon count, of the peaks assigned to Teflon and polystyrene, respectively. Figure 3.13c shows that material closer to the surface creates a stronger signal. Each increase in depth decreases the signal contrast of the polystyrene. Both Figure 3.13b and Figure 3.13c shows that the signal from the surface layer is maximised at the 0 mm offset and the surface suppression increases with the offset as there is a greater proportion of the bulk material compared to the surface material.

3.4.2 Three-layer system

A three-layer system is like the two-layer system but instead of a surface layer with a different material acting as the bulk, both the surface layer and the bulk material are the same material. The material of interest is sandwiched between these two layers as in Figure 3.13a. This type of sample can be used to investigate the depth profile and find what depth makes the greatest contribution to the signal for a given offset. Figure 3.14b shows the spectra for the same fifteen offsets, from -6 mm to 8 mm as shown in Figure 3.13a. The same two peaks were selected to shows the relative signal from the two materials and these were again plotted for multiple surface thicknesses for the offsets and shown in Figure 3.13c. As before, the 0 mm offset has the lowest signal contrast for polystyrene as a ratio of the signal. In the two-layer sample the signal contrast increased monotonically with offset. In the three-layer sample there are two layers of the bulk material, a surface layer and then a deeper layer behind the ROI middle layer. This means that at sufficiently large offset the surface suppression effect starts to supress the signal from the ROI layer and the bulk material behind it dominates. This leads to the fact that at between 5 mm and 6 mm offsets the signal contrast no longer increases for the 1.5 mm deep sample and also explains the reduction of signal contrast at 8 mm offset.
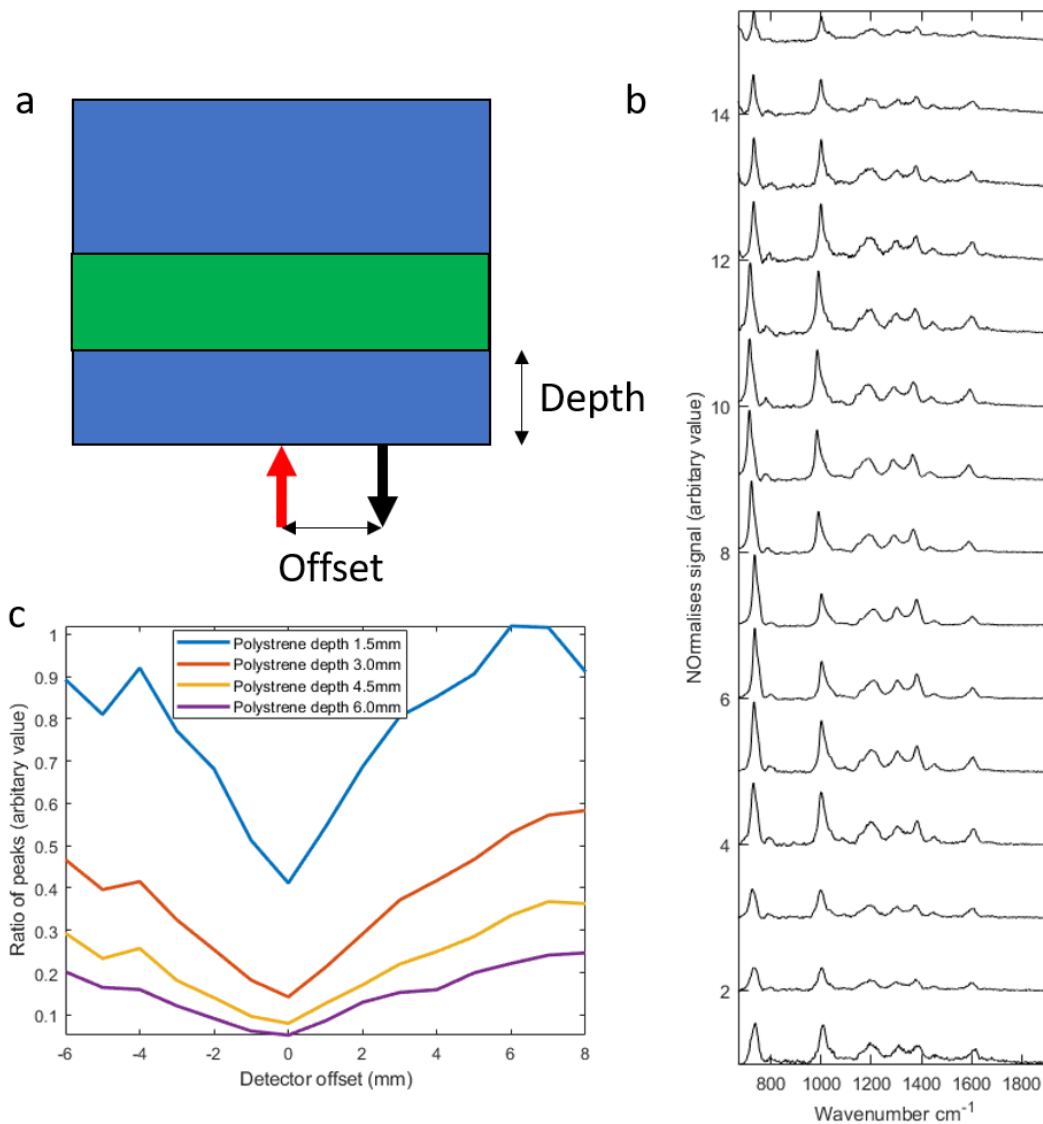
Figure 3.14 a) A schematic of a three-layer system showing how the offset between excitation and detection points and depth are determined, the green layer is polystyrene, and the blue layers are Teflon. The red arrow is the excitation laser and the black arrow is Raman signal collected from a point on the surface b) The spectra for a sample of depth 3.0mm from detectors from -6mm to 8mm offset at 1mm intervals. The offset on the y-axis shows the offset position. c) The ratio of the signal from polystyrene and Teflon at different depths.

3.4.3 Single inclusion

For one final validation a single defect was created within the bulk material by drilling a 2 mm diameter, 1.5 mm cylinder at a depth of 3.0 mm as can be seen in Figure 3.15a. This defect was chosen to demonstrate the localisation effect of SORS.

85
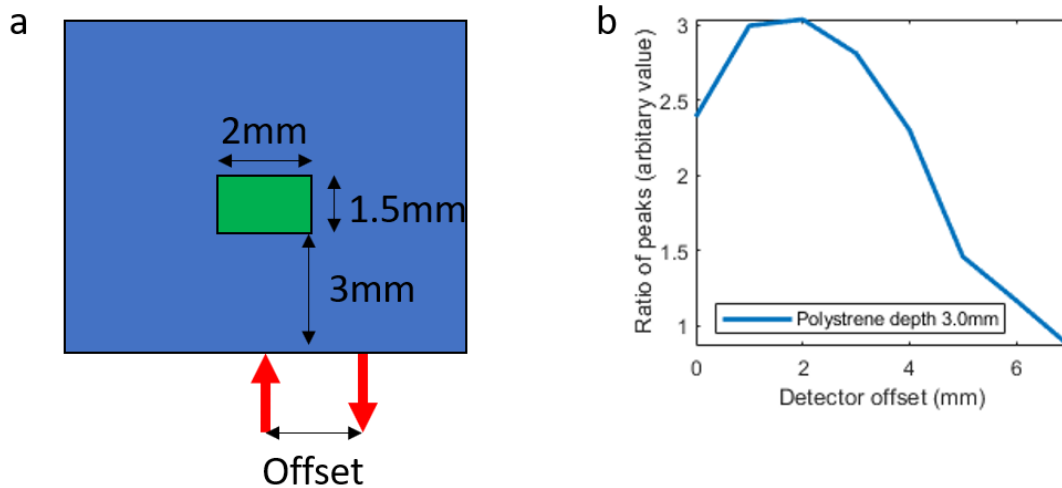
Figure 3.15 a) A schematic of a small defect sample showing how the offset between excitation and detection points and depth are determined, the green is polystyrene, and the blue is Teflon. b) The ratio of the signal from polystyrene and Teflon

The initial increase in signal seen in Figure 3.15b comes from the surface suppression of SORS where the material at the excitation point contributes less to the total signal. As the offset increases further the signal contrast reaches a maximum then a decrease in signal. The reason for this is made clear by investigating Figure 2.7. As the offset increases, more of the photon distribution is offset in the direction of the detector. At sufficiently large offsets the main part of the photon distribution is in the bulk material and this causes the signal contrast to decrease.

4   Chapter 4

Raman spectroscopy for monitoring mineralization of bone tissue engineering scaffolds: feasibility study based on phantom samples

Max Dooley,[1] Aruna Prasopthum,[2] Zhiyu Liao,[1] Faris Sinjab, [1] Jane McLaren,[2] Felicity R.A.J. Rose,[2] Jing Yang,[2] and Ioan Notingher[1,*]

[1]School of Physics and Astronomy, University of Nottingham, University Park, Nottingham NG7 2RD, UK.

[2]School of Pharmacy, University of Nottingham, University Park, Nottingham NG7 2RD, UK.

*ioan.notingher@nottingham.ac.uk

Abstract: Using phantom samples, we investigated the feasibility of spatially-offset Raman spectroscopy (SORS) as a tool for monitoring non-invasively the mineralization of bone tissue engineering scaffold *in vivo*. The phantom samples consisted of 3D-printed scaffolds of poly-caprolactone (PCL) and hydroxyapatite (HA) blends, with varying concentrations of HA, to mimic the mineralisation process. The scaffolds were covered by a 4 mm layer of skin to simulate the real *in vivo* measurement conditions. At a concentration of HA approximately 1/3 that of bone (~0.6 g/cm^3), the characteristic Raman band of HA (960 cm^{-1}) was detectable when the PCL:HA layer was located at 4 mm depth within the scaffold (i.e. 8 mm below the skin surface). For the layers of the PCL:HA immediately under the skin (i.e. top of the scaffold), the detection limit of HA was 0.18 g/cm^3, which is approximately one order of magnitude lower than that of bone. Similar results were also found for the phantoms simulating uniform and inward gradual mineralisation of the scaffold, indicating the suitability of SORS to detect early stages of mineralisation. Nevertheless, the results also show that the contribution of the materials surrounding the scaffold can be significant and methods for subtraction need to be investigated in the future. In conclusion, these

results indicate that spatially-offset Raman spectroscopy is a promising technique for *in vivo* longitudinal monitor scaffold mineralization and bone re-growth.

4.1   Introduction

A common treatment for major bone damage is autologous bone grafting (124). Autologous grafting is not the optimal solution because the quality and quantity of bone grafts that can be harvested is sometimes not sufficient to meet demand, it increases the risk of infection, and can lead to haemorrhaging, cosmetic disability, nerve damage, and a loss of function. An alternative to autologous grafts is the use of tissue-engineered scaffolds that can be implanted in the defect to offer a 3D structure to support and stimulate the regeneration and repair of the bone (125). *In vivo* models where scaffolds are implanted in critical bone defects in large animals (e.g. sheep) have been commonly used to model the healing process in humans (64). These studies provide a better understanding of the bone repair process in order to optimise the physical and chemical properties of the material to reduce healing time and improve the quality of the newly formed bone. For a critical bone defect, the damage to the bone is so great that the body fails to repair the bone correctly (126). What will constitute a critical defect depends on the size of the bone damaged (127; 128), and the age and health of the patient (129; 130). When a defect reaches this critical size, the body fails to fill the defect with extracellular matrix (e.g. collagen) and to mineralise; instead, the exposed damaged bone is repaired leaving an indent or hole in the tissue with repaired sides, leading to bone tissue that is weaker than before the damage (131). When using a scaffold, the quality of the repaired bone depends on the ability of cells to populate and remodel the scaffold. Thus, longitudinal data regarding mineral deposition within the scaffold is desirable and important for optimizing the physiochemical properties of the scaffold.

Typically, the quality of the repaired bone is evaluated by end-point histological tests. However, histology is destructive and therefore can be used only at the end time-point (typically 4-6 weeks after implantation). 3D micro-computed tomography (µCT) is commonly used to analyze the morphology and mineral density of newly formed

bone in animal models (132), including for *in vivo* longitudinal studies (133; 134). μCT has also been combined with single photon emission computed tomography (SPECT) in order to obtain more detailed molecular information during the course of bone formation and remodelling (135). Although this technique requires radioactive SPECT probes, a study using synthetic hydrogel scaffolds implanted in critical size calvarial defects generated in mice, showed that *in vivo* longitudinal data regarding morphology and bone density agreed with end-point histological and μCT evaluations (135).

Raman spectroscopy (RS) is a non-destructive spectroscopic technique that has high chemical specificity and does not require exogenous labels or probes (136). RS has been widely used for the analysis of bone tissue (137; 138; 139) and bone tissue engineering scaffolds (140; 141; 142; 143; 144). Spatially-offset Raman Spectroscopy (SORS) is a variant RS technique that is able to recover molecular information of bone *in vivo* transcutaneously (145; 146). Recently, we demonstrated the feasibility of using SORS to measure Raman spectra of hydroxyapatite (HA) powder buried in layers of polymer and ceramic tissue engineering scaffolds as thick as few millimetres, covered by 1 mm thick skin layer (147). While these feasibility studies indicated the potential of SORS for measuring *in vivo* longitudinal data from small animal model studies, a better understanding of the SORS signals is required in order to optimise the instrumentation for *in vivo* measurements (i.e. a hand-held probe) and support the data analysis. By increasing the maximum offset of the device and having control over the size of the collection points the sensitivity of the device was optimised.

Here we have developed a series of phantom samples to mimic the mineralisation of scaffolds implanted in a large animal critical bone defect and the measurement conditions for *in vivo* longitudinal study. The samples consisted of 3D printed composite scaffolds with polycaprolactone (PCL) and hydroxyapatite (HA) microparticles, for which the concentration of HA varied to simulate different degrees of mineralisation (148). The experiments were carried out using a table-top SORS instrument based on a digital micro-mirror device (DMD) (101), that allowed flexible adjustments of the spatial offsets in order to optimise the measurement conditions

and develop the design of a future fibre-optics SORS probe that could be used in real animal studies.

4.2 Materials and Methods

4.2.1 Spatially-offset Raman spectroscopy (SORS) instrument

The DMD-based SORS instrument was equipped with a 785 nm wavelength laser (Xtra II, Toptica). A 100 mm focal length 2-inch diameter lens was used to focus the laser beam on the sample (120 mW power, spot size ~0.5 mm) and to collect the backscattered Raman photons. After passing through a dichroic filter that blocked the elastically scattered photons, the Raman photons were focused with a lens on a software-controlled DMD (size 14.4 mm x 8.8 mm, resolution 1920 x 1080 pixels, DLP6500 Texas Instrument). As the DMD was located in a plane conjugate to the sample, it allowed the selection of multiple spatially offset collection points (0.22 mm size) distributed in a semi-circle around the point conjugated to the laser excitation, equivalent to spatial offset values in the range of 0-4 mm. The Raman photons reflected by the DMD collection points were analysed by a spectrometer (Holospec, Andor) equipped with a deep-depletion back-illuminated CCD (iDus 420, Oxford Instruments). For a selected spatial offset, the SORS spectrum was calculated as the sum of the spectra corresponding to all DMD collection points on the corresponding semi-circle, after aligning and calibrating them along the wavenumber axis. For each spatial offset, 18 repeat spectra were measured at an acquisition time of 10 s per spectrum.

4.2.2 3D printing of PCL:HA scaffolds

Porous scaffolds with the same pore size and different dimensions were designed by BioCAD software. A viscous polycaprolactone (PCL)/dichloromethane (DCM) solution was vigorously mixed with hydroxyapatite (Sigma Aldrich, UK) to create different ratios of PCL and HA in the order of 4:0, 4:1, 1:1, 1:2 and 1:4 (Table 1).

Ratio PCL:HA	Percentage HA by Mass	HA density g/cm^3 (±0.01)
1:0	0%	0
4:1	20%	0.18
1:1	50%	0.68
1:2	67%	0.83
1:4	80%	0.93
Bone	~70% (149)	~2 (149)

Table 1. Scaffold and bone samples used in this study
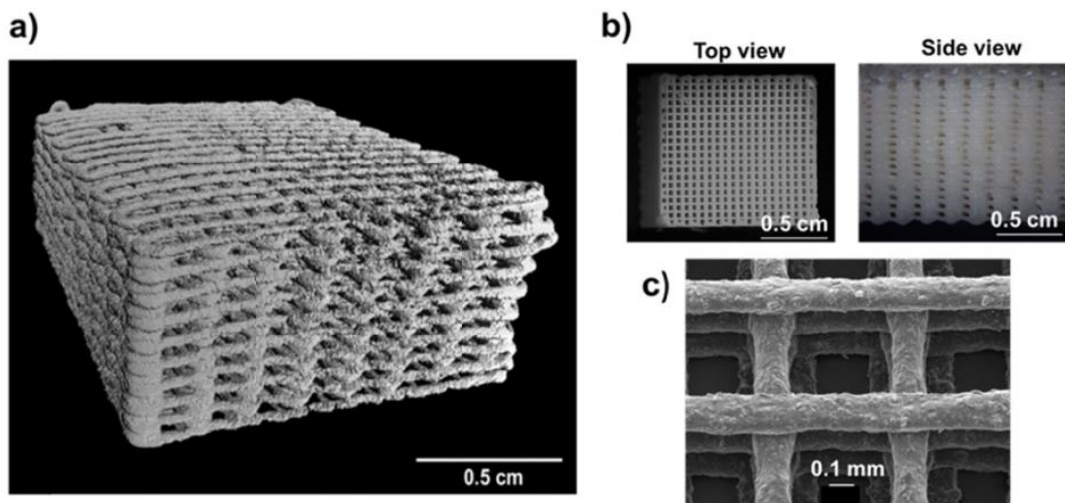
Figure 4.1Representative images of the 3D printed PCL:HA scaffolds used in this study. a) ⲘCT 3D reconstruction image of a PCL:HA 1:4 scaffold (1 x 1 x 0.5 cm3), porosity = 64.7 %; b) Images from dissecting microscope of a PCL:HA (1:4) scaffold (1 x 1 x 1 cm3). c) scanning electron microscopy of PCL:HA scaffold with 1:2 blend ratio

The solution was loaded into a printing cartridge and directly deposited through a 25G tip (250 µm ID, Adhesive Dispensing, UK) using 3D Discovery printer (regenHU, Switzerland) with a pressure of 6 bar and a printing speed of 5 mm/s. Rapid DCM evaporation led to solidification of the printed construct. Table 1 converts these weight ratios into HA concentration to allow a better comparison with data available in the literature for typical mineralised bone (149).

4.2.3 Phantom samples

Figure 4.2 describes schematically the intended use of the scaffolds in large animal models and the phantom sample developed in this study to mimic the mineralisation process and the *in vivo* SORS measurements. For real *in vivo* experiments, the scaffold is implanted into a critical defect drilled to a diameter of 8 mm and 15 mm depth in the femur of a sheep and covered by a layer of skin (typically 3-5 mm thick) (150)(schematically described in Figure 4.2a-c). The phantom consists of several parts made of different materials (Figure 4.2d). Multiple 1.5 mm thick layers of Teflon where layered to create an 18 mm thick phantom with a square hole (10 mm x 10 mm x 10 mm) which mimicked the critical defect. Behind the Teflon slab, a 5 mm thick layer of polystyrene (PS) was placed in order to give an indication of whether the femur bone at the back of the defect would contribute to the measured SORS signal.

After the insertion of the scaffolds (sizes 10 mm x 10 mm x 2mm) in the Teflon hole, the phantom sample was covered by a layer of pig skin (sourced from a local retail outlet) cut to 4 mm thickness, with a large enough surface area to cover the face of the phantom. While this phantom closely resembled the *in vivo* measurement conditions, the materials used were selected to have similar light scattering properties to bone (125) but distinctive Raman bands to allow an understanding of the contributions of various regions of the phantom to the measured SORS spectra. This is particularly important for SORS measurements where different parts of the sample can be probed depending on the value of the spatial offset. Figure 4.2e presents the Raman spectra of each material used for the phantom. The spectrum of HA has a strong band at 960 cm^{-1} (phosphate band) (108; 138; 139). The PCL has Raman bands assigned to the C-O-C vibrations as a triplet at 1067 cm^{-1}, 1098 cm^{-1}, and 1110 cm^{-1}, and CH$_2$ bands at 1300 cm^{-1} and 1445 cm^{-1} (126). Teflon and PS have strong Raman bands at 734 cm^{-1} and 1004 cm^{-1} respectively. Therefore, the use of these two materials for the bone phantom effectively allows us to identify the contributions of the sides (Teflon) and back (PS) of the critical defect to the measured SORS spectrum without interfering with our measurement of the 960 cm^{-1} band from HA. Because the molecular composition of pig skin changes with depth, Raman spectra were measured from the top epidermis/dermis part (bands at 970 cm^{-1} and 1300 cm^{-1} assigned to

collagen) and from the adipose tissue at the bottom part (strong 1368 cm^{-1} band) (151; 152).

4.2.4 Data analysis

First, all spectra were normalised to minimum 0 and maximum 1. The difference between the SORS spectra of the PCL:HA scaffold and PCL-only scaffold (control sample) at each offset value was then calculated using an in-house iterative algorithm. To eliminate errors caused by small baseline or intensity variations (likely due to small differences in optical scattering properties between samples), a correction factor in the form of a 2nd order polynomial was included in the subtraction algorithm. This polynomial was determined by minimising the square difference between the two SORS spectra in an iterative method. The spectral region 930-980 cm^{-1} containing the main HA band at 960 cm^{-1} was excluded from the minimisation. Thirty iterations were used, as this was observed to lead to stable solutions in all cases. .
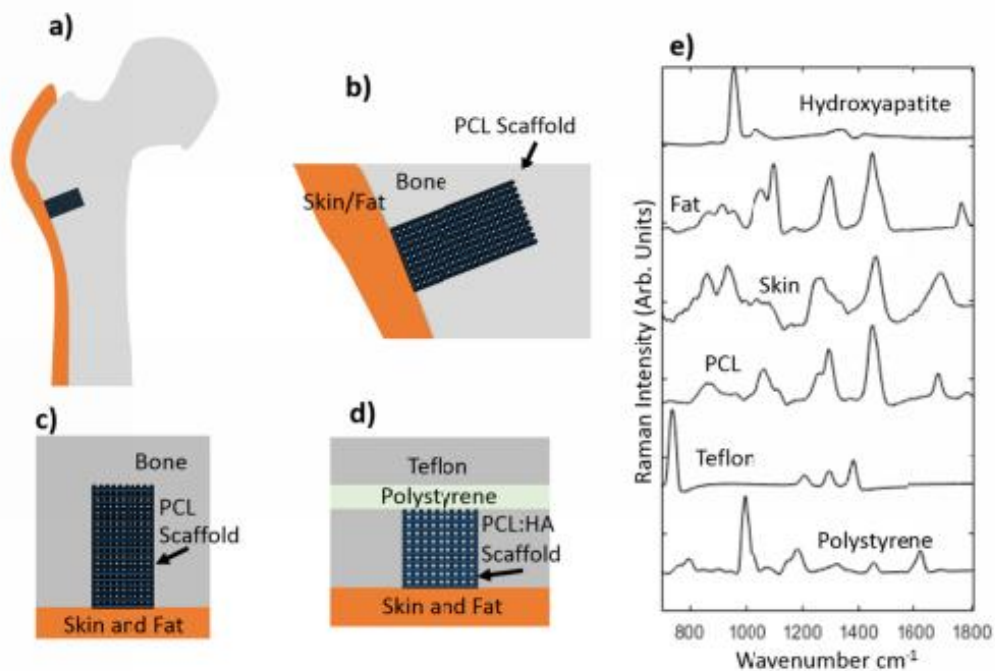
Figure 4.2a) Diagram of the head of a femur with a critical defect drilled into it with the position of the scaffold shown. b) Close up of the defect filled with a PCL scaffold. c) A schematic of a defect in the same orientation as the phantom for comparison. d) A schematic of the phantom used in this study, designed to mimic a critical defect. e) Raman spectra of the materials that make up the phantom (spectra normalized between 0 and 1 and shifted vertically for clarity).

4.3 Results and Discussion

4.3.1 Testing the limits of detection for the PCL:HA scaffolds

First, we tested the detection limit of the SORS measurements for PCL:HA layers with varying HA concentration, placed at different depths within the phantom sample. This was achieved by filling the defect hole with five 2 mm thick layers of scaffold. Four of these were PCL-only and one layer of PCL:HA blend (Figure 4.3a). For each ratio of the PCL:HA blend, the PCL:HA layer was placed in turn at 0, 2, 4, 6, and 8 mm beneath the skin layer. A sixth sample containing five PCL-only scaffold layers was used to mimic the initial conditions of a newly implanted scaffold into the defect. For all samples, SORS spectra were acquired using spatial offsets of 0, 1, 2, 3 and 4 mm. Figure 4.3b,c present the SORS spectra for the phantoms containing PCL:HA layers with the lowest and highest concentrations of HA.

Figure 4.3b,c show that at 0 mm spatial offset, all SORS spectra were dominated by bands assigned to the top skin layer, in particular epidermis/dermis. Increasing the spatial offset to 1 mm already enabled the detection of Raman bands assigned to the deeper layers of the sample, including the detection of the 960 cm^{-1} band assigned to HA, as well as bands assigned to the adipose tissue in skin (1445 cm^{-1} band), PCL (bands in the 1000-1100 cm^{-1} region), and Teflon (734 cm^{-1}). When the spatial offset was further increased (2-4mm range), the contribution of the subsurface layers of the phantom increased, allowing even detection of the polystyrene (PS) (1004 cm^{-1} band) back layer. For the PCL:HA 4:1 layer (HA concentration ~10 times lower than in bone), the HA band was detected only when the PCL:HA layer was at the top of the scaffold, immediately under the skin layer (i.e. 0 mm depth).
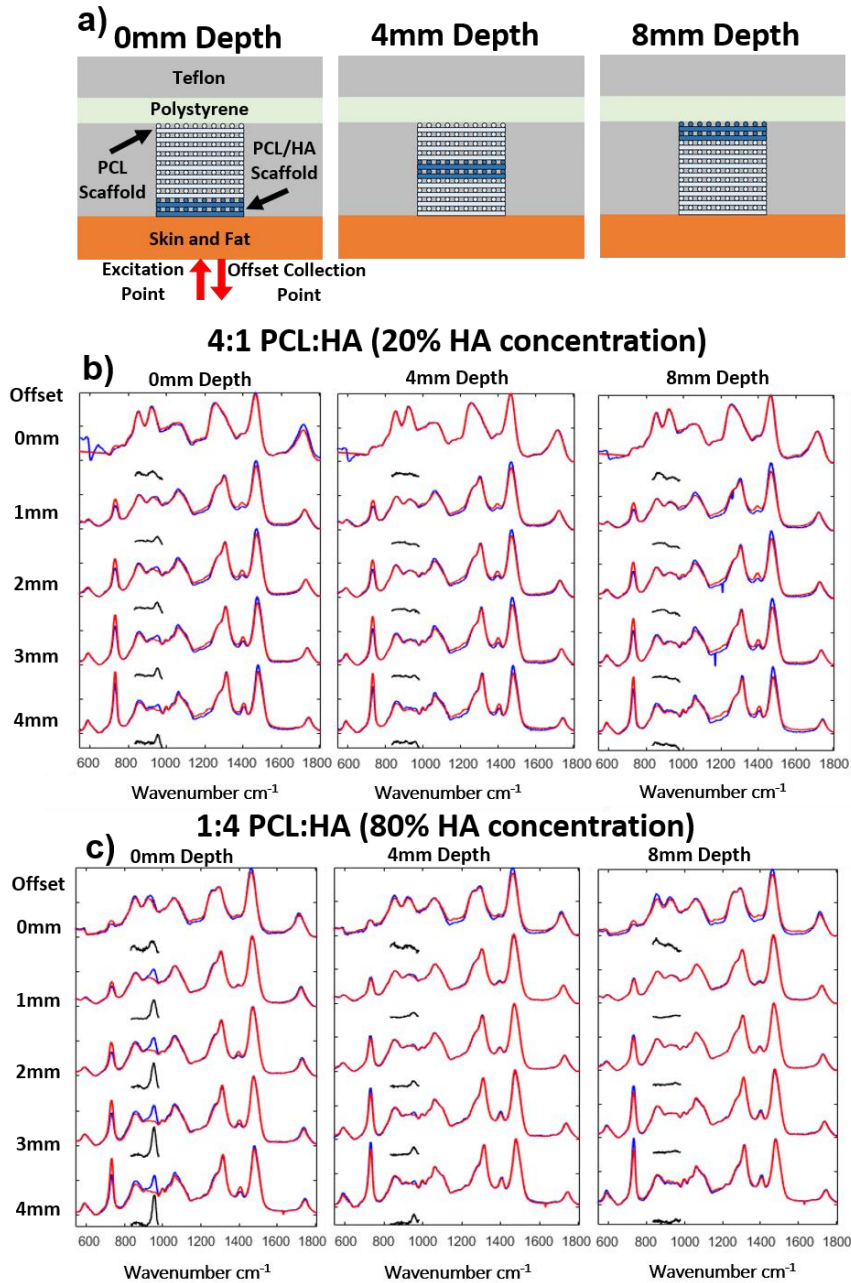
Figure 4.3 a) Schematic of the phantom with a single 2 mm thick PCL:HA scaffold layer at 0, 4 and 8 mm depth. b) SORS spectra for 4:1 PCL:HA ratio scaffolds at 0, 4, and 8mm depths. c) SORS spectra for 1:4 PCL:HA. The blue lines are the spectra of the phantoms containing the blended PCL:HA layers; the red line are for PCL only scaffolds (control). The black lines present the difference spectra blue minus red lines in the 830-1000 cm^{-1} region (2x magnified).

However, for the PCL:HA 1:4 layer (HA concentration roughly half that of bone), SORS was able to detect the 960 cm^{-1} band even when the layer was 4 mm deep in the scaffold. The presence in the SORS spectra of the 734 cm^{-1} band assigned to Teflon indicated that the side walls of the defect hole contributed to the measured SORS

spectra. This result suggests that in an *in vivo* experiment, the bone side walls of the defect would also contribute to the SORS spectra and the band at 960 cm^{-1} may overlap the signal from the mineralising scaffold. This contribution, which could be established at the start of the experiment (i.e. day zero), will have to be taken into account when attempting to determine the concentration of HA within the scaffolds.

In order to provide a quantitative measure of HA detection from the SORS spectra, the ratio between the 960 cm^{-1} band (HA) in the difference spectra and the 1445cm^{-1} band in the PCL:HA spectrum (CH$_2$ deformations, mainly in the skin and PCL scaffold) was calculated for all samples analysed (Figure 4.4). The 1445 cm^{-1} band was selected as an internal standard based on the assumption that the adipose tissue in the skin would have the lowest variation compared to any other parts of the bone defect. For comparison, a set of measurements were also carried out using a 2 mm thick bone sample from the leg of a sheep (sourced from a local retail outlet). The results in Figure 4.4 show that for 0 mm offset, the SORS spectra cannot discriminate between the different concentrations of HA present in the scaffolds. However, at 2 mm offset, the I$_{960}$/I$_{1445}$ ratio decreases as the PCL:HA layers are located deeper in the sample and as the concentration of HA decreases. The HA remained distinguishable until the PCL:HA layers were placed at 6 mm depth where the data started to overlap.
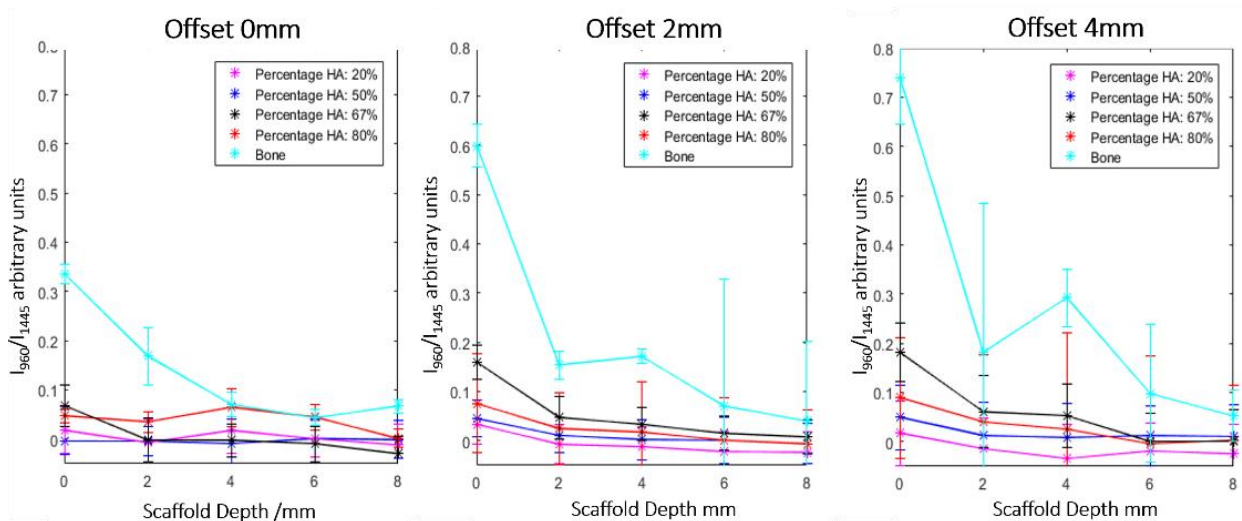
Figure 4.4 The ratio between the intensity of the 960 cm^{-1} band in the difference spectra and the 1445 cm^{-1} band in the spectra of the PCL:HA samples. Error bars represent the standard error of the mean for 18 repeat measurements.

These results lead to the conclusion that the 4 mm spatial offset provides the highest detection sensitivity and resolution for detection of HA. The 4 mm offset was the largest offset tested in this investigation (limited by the size of the DMD and instrument optics), and it is possible that larger offsets may have yielded higher sensitivity. The larger separation between the signals means that the larger offsets may be able to differentiate between smaller changes in mineralisation and therefore be more useful for longitudinal *in vivo* measurements. The results indicate that the limit of detection for HA depends on the depth, ranging from 0.18 g/cm^3 (~10x smaller than bone) at the top of the scaffold immediately under the skin layer to ~0.61 g/cm^3 (~1/3 of bone concentration) at 4 mm depth in the scaffold. For the PCL:bone samples, the 960 cm^{-1} band was broader compared to the bands recorded for the PCL:HA scaffolds, likely due to the more complex molecular composition of bone (HA present in more crystalline phases). Because all spectra were analysed using the algorithm optimised for the PCL:HA scaffolds, the analysis led to some larger error bars for the PCL:bone samples at 4 mm offsets.

4.3.2   Phantoms for mimicking in vivo mineralization patterns

Next, phantom samples were constructed to investigate the feasibility of SORS to monitor *in vivo* biologically relevant models for bone repair, with the focus on scaffold mineralization. The aim was to determine the lowest levels of HA that can be detected and to investigate whether the SORS spectral and temporal profiles can discriminate between spatially homogenous and non-homogenous mineralization models.

4.3.2.1   *Uniform mineralization model*

In this model the phantoms mimicked a process by which the mineralisation of the implanted PCL scaffold undergoes a uniform mineralisation throughout the PCL scaffold. The samples used in this test were PCL-only and PCL:HA scaffolds of 10 mm x 10m m x 10 mm inserted in the Teflon slab covered by the 4 mm pig skin layer (schematically presented in Figure 4.5a). The amount of HA in the PCL:HA scaffolds were increased using the ratios 4:1 - 1:4 in order to mimic different time steps in the process of mineralisation, from the moment of implantation to ~1/2 the HA concentration of mature bone.
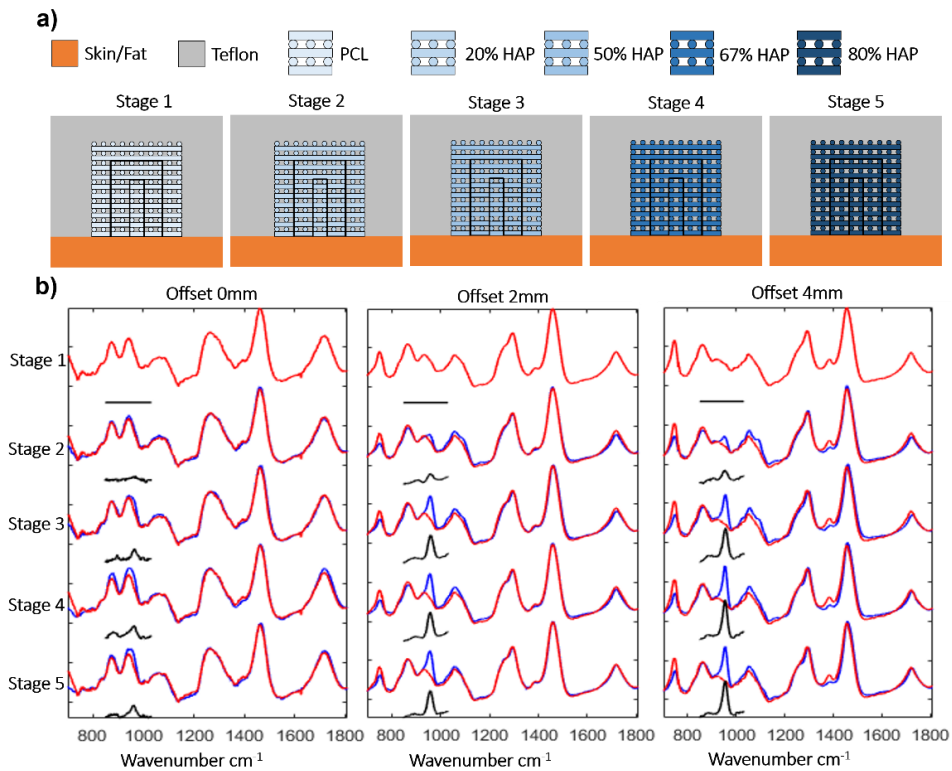
Figure 4.5 a) A schematic of the phantoms used for the uniform mineralization model. b) SORS spectra of the phantoms mimicking the uniform mineralisation model. Blue lines: SORS spectra of PCL:HA scaffolds, Red lines: SORS spectra of the PCL-only scaffold in the phantom; Black line the difference between the blue and red lines in the 830-1000 cm^{-1} range.

Figure 4.5b presents the SORS spectra measured from the uniform PCL:HA scaffolds within the phantom sample at different spatial offsets. At 0 mm offset, the SORS spectra were dominated by Raman bands assigned to connective tissue in skin. The 960 cm^{-1} band assigned to HA was detected only for the PCL:HA scaffolds with rations higher than 1:1 (~0.29 g/cm^3). Increasing the spatial offset to 2 mm allowed the detection of the 960 cm^{-1} band corresponding to HA in all scaffolds, even at the lowest HA concentration of 4:1 (0.18 g/cm^3). For a given spatial offset (apart from 0 mm), the intensity of the 960 cm^{-1} band increases with the increased concentration of HA. The data also indicated that for a sample with a given PCL:HA ratio, increasing the spatial offset value from 2mm to 4 mm led to an increase in the intensity of the 960 cm^{-1} band (the Raman photons travelling or generated deeper in the scaffold contribute more to the spectra). The deeper sampling also led to an increase in the intensity of the 734 cm^{-1} band corresponding to Teflon (side walls of the defect). However, for a given spatial offset value, the contribution from the defect side walls (i.e. Teflon

signal) was constant and could therefore be subtracted. Compared to the SORS spectra in Figure 4.3, for a given spatial offset value and PCL:HA ratio, the spectra corresponding to the uniform PCL:HA scaffolds (Figure 4.5) show a higher ratio between the intensity of the bands at 960 cm^{-1} assigned to HA and the 1090 cm^{-1} band corresponding to the PCL.
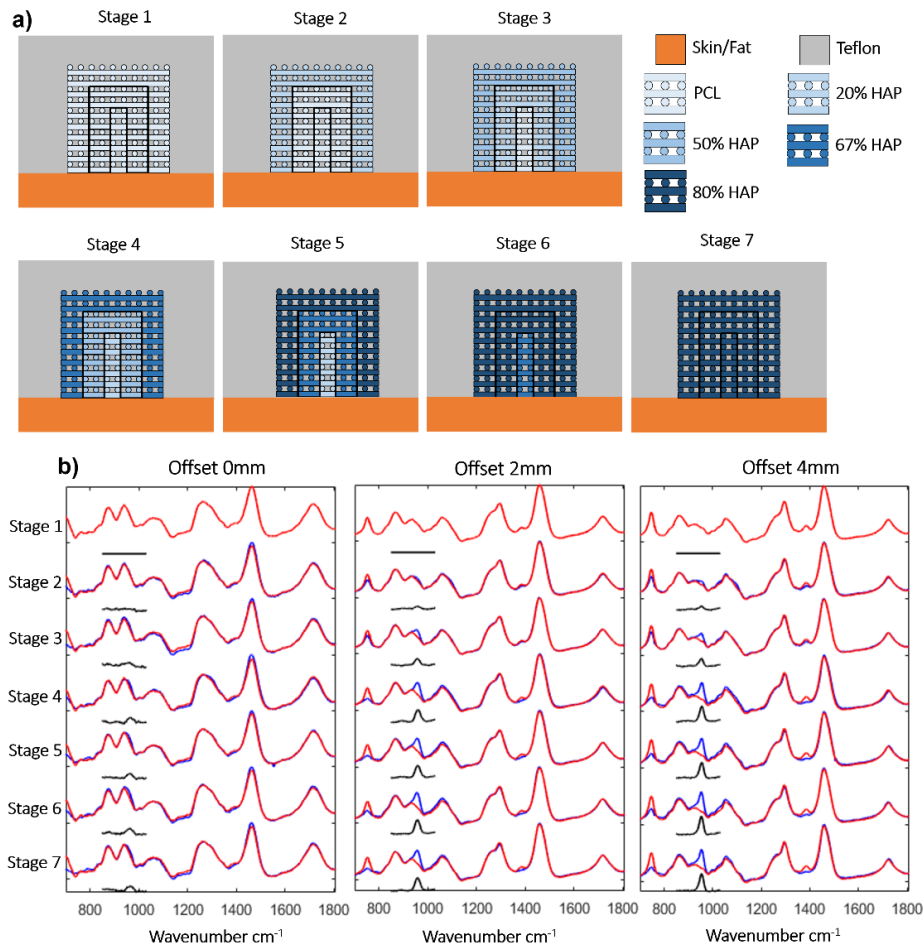
Figure 4.6 a) A schematic of the phantoms used for the gradual inward mineralization model. The 7 stages are shown with the shade of the layers of the phantom indicating the concentration of HA in the PCL/HA scaffold with a key of the colours used. c) SORS spectra for the graduated mineralisation model. The blue line is read with the blended material and the red line is the PCL only scaffold in the phantom. The black line is the difference between the two.

These results indicate that the combination between the I_{960}/I_{1090} and I_{960}/I_{1445} ratios could be used to quantify the density of the HA and the HA depth extend into the PCL scaffold.

4.3.2.2   Gradual inward mineralization

The second model studied here was the graduated inwards mineralisation of the scaffold. In this model, HA mineralisation of the extracellular matrix deposited within the scaffold starts at the surface of the old bone defect and grows into the scaffold with a concentration gradient of HA into the scaffold. We used seven different configurations of the phantom from all PCL-only to uniform 1:4 PCL:HA (Figure 4.6). A naming convention was designed to describe the scaffolds in the defect: the name uses the ratio of concentration in each of the layers naming them from outside inwards so 41:PCL:PCL is the 4:1 PCL:HA blend on the outside with two layers of PCL inside. Figure 4.6 shows that, as with the previous samples, the Raman spectra recorded at 0 mm spatial offset had low sensitivity for HA as the main contribution was from the top skin layer. At increased offsets, the 960 cm^{-1} band was detected in all spectra, even at the lowest concentration of HA such as the 41:PCL:PCL. This sample represents low levels of the mineralisation starting from the surface of the defect, as only the exterior of the scaffold contains HA at a density of 0.18 g/cm^3.
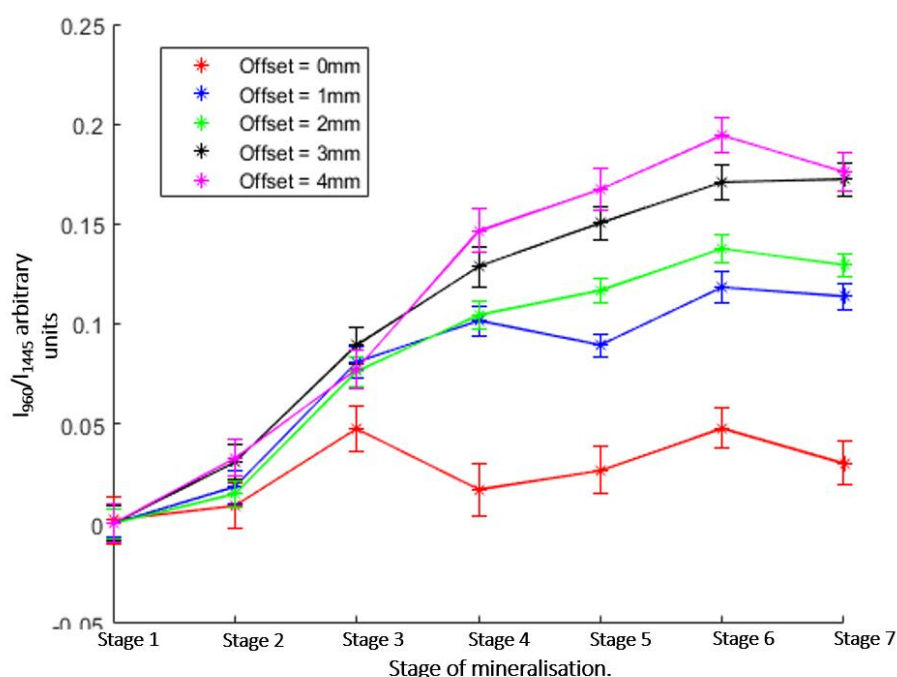
Figure 4.7 Analysis of the SORS spectra for the gradual inward mineralization model. The ratio between the intensity of the 960 cm^{-1} band in the difference spectra (PCL:HA minus PCL-only scaffolds) and the 1445cm^{-1} band in the spectra of the sample containing HA. Each stage from 1-7 represents an increase in HA concentration. Error bars represent the standard error of the mean for 18 repeat measurements.

These results indicate that for this model, HA present in the scaffold is detectable by SORS even at concentrations an order of magnitude lower than the concentration of complete mineralisation of bone. Increasing the offset to 4 mm provided a similar increase in the intensity of the 960 cm^{-1} band, but at the same time, an increase in the signal from the Teflon layers surrounding the scaffold. Therefore, the use of 2 mm offset seemed to be more advantageous as less background signal from the side walls of the bone defect are detected. In real measurements, this background signal can overlap the signal from the newly deposited HA in the scaffold. To evaluate the optimal conditions for quantification of HA in the phantom samples, Figure 4.7 presents the calculated ratio between the intensity of the 960 cm^{-1} band in the difference spectra (PCL:HA minus PCL-only scaffolds) and the 1445cm^{-1} band in the spectra of the sample containing HA (I_{960}/I_{1445}). The results show that the relative intensity of the 960 cm^{-1} band increased when the concentration of HA and the spatial offset increased. The highest sensitivity and detection resolution for HA was observed when using the 4 mm spatial offset. However, once the outer PCA:HA layer of the scaffold reached the 1:4 ratio, the I_{960}/I_{1445} ratio seemed to plateau, regardless of the value of the spatial offset (higher than 0), indicating a decrease in detection resolution for HA.

4.4   Conclusions

The use of tissue engineering scaffolds for stimulating bone re-growth in critical bone defects is a promising way to improve bone healing; however, monitoring bone growth *in-situ* remains a challenge. Using phantom samples based on 3D-printed PCL:HA scaffolds we investigated the feasibility of SORS to monitor mineralisation of bone tissue engineering scaffolds in large animal models. The tests investigating the detection limits for mineralisation showed that SORS is able to detect HA concentrations at an order of magnitude lower than that found in living bone, even through a 4 mm thick layer of skin (mimicking *in vivo* transcutaneous measurements). These low concentrations are only detected when the HA was located immediately under the skin surface. As the HA concentration increased so did the depth at which the HA was detectable. For the highest concentration of HA, the detection depth increased to 4 mm. Bone has a higher concentration of HA than any of the scaffolds

investigated here and a 2 mm thick layer produced a stronger signal across all depths as seen in Figure 4.4. The I_{960}/I_{1445} band ratio can be a useful parameter to attempt longitudinal quantification of HA concentration, but would require a means to measure the thickness of the skin layer, which can vary during the 4-6 week duration of the real *in vivo* experiments. Nevertheless, such changes in skin thickness may be measured using complementary techniques, such as ultrasound imaging.

For the experiments mimicking the uniform scaffold mineralisation, setting a spatial offset larger than 2 mm allowed sensitive detection of HA. Similar results were observed for the inward gradual mineralisation model. Nevertheless, the highest sensitivity and detection resolution for HA was observed when using the 4 mm spatial offset (largest offset possible with current instrument), which indicates that even the earliest mineralisation stage included in this study was detectable (i.e. only the outer 2 mm layer of the scaffold contained HA at a concentration ~10x lower than bone). The results also show that the surrounding walls of the bone defect also contributed to the measured SORS spectra (Teflon signal), that may overlap the Raman bands from the HA in the scaffold. For this reason, it would be advantageous to start the acquisition of SORS spectra as soon as the scaffold was implanted in order to establish a baseline SORS spectrum and quantify the changes in the HA signals during the 4-6 week period of bone re-growth. The ability to follow the bone healing process on the same animal will provide higher quality data with ethical and economic benefits from reducing the number of animals used during the research.

5   Chapter 5

Spatially-offset Raman spectroscopy for monitoring mineralization of bone tissue engineering scaffolds: feasibility study based on phantom samples

Max Dooley[a], Jane McLaren[b], Felicity RAJ Rose[b], Ioan Notingher[a,*]

[a] *School of Physics and Astronomy, University of Nottingham, University Park, Nottingham, NG72RD*

[b] *School of Pharmacy, Nottingham Biodiscovery Institute, University of Nottingham, University Park, Nottingham, NG7 2RD*

* Corresponding author: ioan.notingher@nottingham.ac.uk

5.1   Abstract

A wide range of biomaterials and tissue engineered scaffolds are being investigated to support and stimulate bone healing in animal models. Using phantoms and rat cadavers, we investigated the feasibility of using spatially offset Raman spectroscopy (SORS) to monitor changes in collagen concentration at levels similar to those expected to occur in vivo during bone regeneration ($0 - 0.84$ g/cm^3). A partial least squares (PLS) regression model was developed to quantify collagen concentration in plugs consisting of mixtures or collagen and hydroxyapatite (predictive power of ±0.16 g/cm^3). The PLS model was then applied on SORS spectra acquired from rat cadavers after implanting the collagen:hydroxyapatite plugs in drilled skull defects. The PLS model successfully predicting the profile of collagen concentration, but with an increased predictive error of ±0.30 g/cm^3. These results demonstrate the potential of SORS to quantify collagen concentrations, in the range relevant to those occurring during new bone formation.

5.2 Introduction

Bone healing involves complex spatial- and time-dependent molecular processes related to the development of extracellular matrix and deposition of the hydroxyapatite (HA) mineral phase. Understanding these molecular processes is vital for developing optimized scaffolds and grafts that can stimulate bone regeneration in patients. X-ray imaging is the main technique currently used for monitoring bone regeneration in vivo, but provides limited information: it shows the spatial distribution of the mineral components of bone but it is insensitive to the organic molecules forming the extracellular matrix (153). In addition, X-rays can have health risks to both patients and the clinical practitioners and therefore limits X-rays use for monitoring new bone formation (154). Current bone healing studies in animal models (e.g. rats, sheep) use micro-computed tomography (CT) to image bone resections corresponding to particular time points of the study (155; 64). Micro-CT provides detailed information regarding the morphology and mineral structure of the bone but lacks molecular specificity. A key challenge in understanding bone regeneration is measuring the subtle molecular processes related to the extracellular matrix, which occur at the earlier stages of the healing process and are the precursors of the later stages of bone mineralization.

In this paper, we investigated the feasibility of spatially offset Raman spectroscopy (SORS) for in vivo detection and quantification of molecular changes related to bone extracellular matrix deposition as would be observed in a small animal model. Raman spectroscopy is a non-destructive label-free optical spectroscopy technique that has been widely used for molecular analysis of bone tissue (156), soft connective tissue (157) and tissue engineering scaffolds (144). The diffuse nature of near-infrared light (785-1000 nm wavelength) in connective tissue and porous tissue engineering scaffolds makes diffuse Raman spectroscopy, such as SORS, ideally suited for probing the biomolecular processes deeper into materials, during regeneration of connective tissue in vivo. SORS is a type of diffuse Raman spectroscopy that can measure molecular information deeper into materials. SORS has been used for characterization of bone tissue, ex-vivo and in vivo, in animals and humans (158; 159; 160; 101). While most SORS configurations are based on fiber optical probes, digital micro-mirror devices (DMDs) have been proposed recently to offer a flexible approach to optimize the

spatial offsets (147), and have been applied to detect hydroxyapatite (HA) in phantom samples mimicking transcutaneous SORS measurements of bone (116; 161). In the context of bone regeneration in large animal models, SORS studies using 3D-printed polymer scaffolds and HA have shown that HA can be detected even at depths beyond 10 mm at concentrations 10 times lower than in mature bone (116).

While detailed information regarding the mineral phase of bone can be obtained by measuring the intense bands of HA (e.g. 960 cm^{-1} band), the information regarding the extracellular matrix, which is the focus of this study, is more challenging to extract because of the weaker and overlapping bands. Collagen type 1 makes up close to 30% of healthy mature bone and is vitally important in conveying it's structural properties (161; 162). Collagen is also the first structural component of bone to be formed during bone defect healing (22). Thus, the ability of SORS to measure the molecular processes at the early stages of bone regeneration would expand the usefulness of bone healing studies in in vivo models.

Here, we used a series of phantoms to mimic the development of the extracellular matrix (i.e. increase in collagen concentration over time) and then the mineralization as previously described in a healing bone defect in a rat calvarial model. The phantoms were designed to follow the expected time course changes in collagen and HA concentrations reported in the literature (22; 163). Using these phantoms, a multivariate model based on SORS spectra was developed to estimate the concentration of collagen. Next, we applied the SORS model to quantify the concentration of collagen when mixtures of collagen and HA, at different concentrations, were implanted in calvarial defects in rat cadavers. We investigated the feasibility of discriminating the collagen concentration changes expected to occur both during the early stages of extracellular remodeling, as well as at the later stages when the Raman bands of collagen overlap with the strong bands corresponding to HA.

5.3   Materials and methods

5.3.1   Spatially-offset Raman spectroscopy (SORS) instrument

The SORS instrument was equipped with a 785 nm wavelength laser (Xtra II, Toptica). A 75 mm focal length 50.4 mm diameter lens was used to focus the laser beam (power 120 mW) on the sample (spot size ~0.3 mm) and to collect the backscattered Raman photons. After passing through a dichroic filter that reflected the elastically scattered photons, the Raman photons were focused with a lens (focal length 75 mm) onto a software-controlled digital micromirror device (DMD) (size 14.4 mm x 8.8 mm, resolution 1920 x 1080 pixels, DLP6500 Texas Instruments). As the DMD was located in a plane conjugate to the sample, it allowed the selection of multiple spatially offset collection points (diameter each 0.1 mm) distributed in a semi-circle centered on the point conjugate to the laser excitation, equivalent to spatial offset values in the range of 0-1.5 mm at 0.5 mm steps (101). A full schematic of the set up can be found in our earlier work (116).The Raman photons reflected by the DMD collection points were collimated by a 200 mm focal length lens then focused onto the entrance slit of a spectrometer (Holospec, Andor) equipped with a deep-depletion back-illuminated CCD (iDus 420, Oxford Instruments). The slit was opened to 4 mm width, as the spectral resolution was defined by the size of the DMD collection points (164; 165). For a selected spatial offset, the SORS spectrum was calculated as the sum of the spectra corresponding to all DMD collection points on the corresponding semi-circle, after aligning and calibrating them along the wavenumber axis (101). Each SORS spectrum was the average of 10 measured spectra, each acquired at 50 seconds integration time. A polynomial baseline (third order) was subtracted to remove the background in the Raman spectra.

5.3.2   Calvarial bone regeneration simulation model

Figure 5.1a describes schematically a simplified pattern of the two main components of bone over time for a healing bone defect in a rat skull using values taken from the literature (22; 165). This pattern was used to select the concentrations of collagen and HA in the phantom samples, as collagen and HA concentrations change during the healing process (Figure 5.1b).
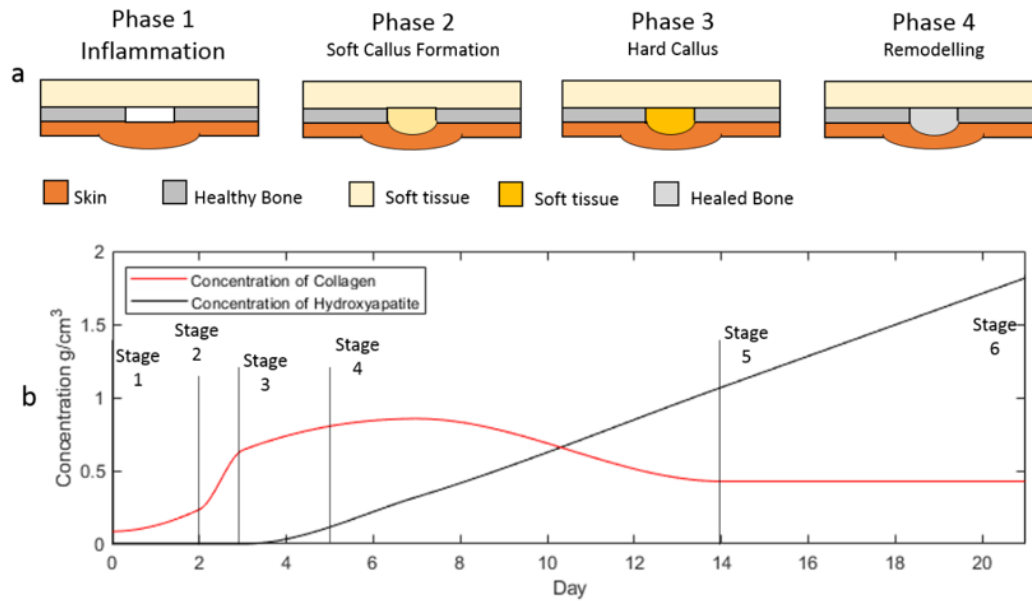
Figure 5.1 A schematic description of the four main phases of a bone critical defect healing (based on (22)16]. b) The time dependence model for collagen (red line) and hydroxyapatite (HA) (black line) concentrations during bone healing [based on (165)]. Stages 1-6 are labelled as the points of main interest in this study and are referenced in Table 1.

After the initial bone damage (day 0), the repair process starts with inflammation around the area. Soft tissue in the form of collagen enters the defect to form the extracellular matrix within the first day or two post-damage. The concentration of collagen continues to increase during the next 4-5 days, as HA diffuses into the formed extracellular matrix and mineralization is initiated. After day 8-9, the density of collagen decreases as the bone mineralizes until the densities of collagen and HA reach the level found in normal bone. For this study, six time-points were selected between the initial condition to the steady state at the end, with concentrations of collagen between 0.085 g/cm^3 and 0.43 g/cm^3. The maximum concentration of collagen was 0.84 g/cm3, corresponding to day 7 (stage 4).

5.3.3 Partial least squares (PLS) model

A prediction model was build using n = 52 phantom samples that spanned the ranges of both collagen and HA concentrations typically encountered during the entire bone regeneration process (as determined in Section 2.2). A PLS model based on the SORS spectra was developed to predict the concentration of collagen in new samples, using the spectral range 800 – 1606 cm^{-1}. The PLS model was evaluated using a leave-one-out bootstrapping method. Four separate PLS models were built, one for each spatial offset (0 mm, 0.5 mm, 1 mm and 1.5

mm). After the training was complete, the models were saved, and no further spectra were added to the training model.
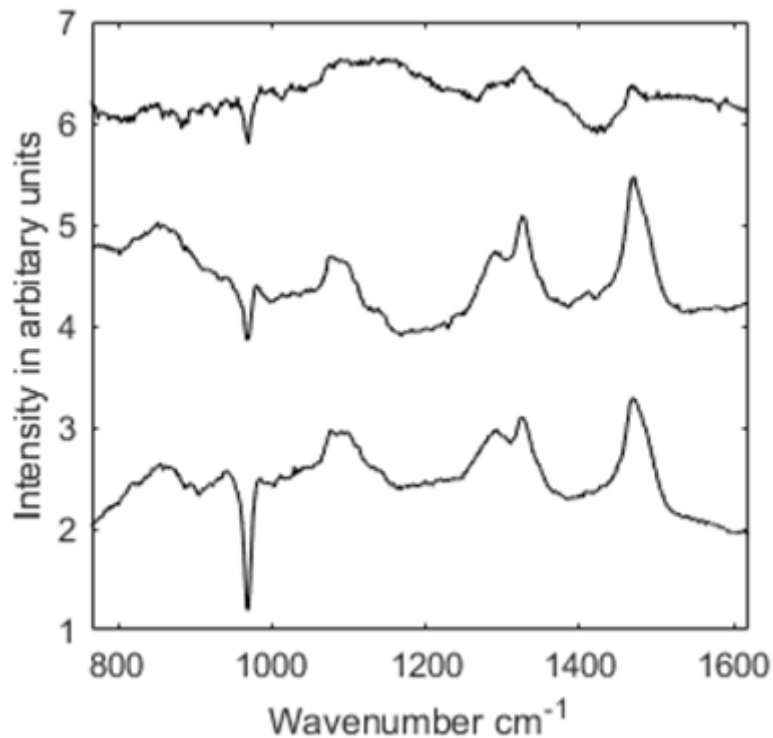
Figure 5.2 The three top components of the pls model for 1mm offset out of 5.

Figure 5.2 shows the top three components for the pls model for the 1mm offset. The HA peak is clearly visible at 960cm^{-1}. Clear biological bands are visible at 1450cm^{-1}, 1100cm^{-1} and 1300cm^{-1}. This combination of clear biological peaks and a strong predictive power implies that the model has captured important data about the data set.

The most effective models, found to correspond to spatial offsets 1 mm and 1.5 mm, were used in conjunction to form an improved model, whereby the collagen concentration was calculated as the mean of the values predicted by the two models.

Stage	Day	Collagen Density, g/cm^3	HA Density, g/cm^3
1	0	0.085	0.00
2	2	0.24	0.00
3	3	0.64	0.00
4	7	0.86	0.32
5	14	0.43	1.07
6	21	0.43	1.84

Table 1. Densities of collagen and HA selected to represent different stages during bone healing.

5.3.4 Phantom construction

Figure 5.3a describes schematically the phantom design for the rat model used for developing the PLS model. The skull bone was mimicked by a Teflon sheet 1.5 mm thick with a 6.3 mm diameter defect drilled through it. Teflon was selected as it has similar scattering properties to bone (166) while the main Raman band at 734 cm^{-1} does not overlap with the main bands present in the Raman spectra of the biological materials investigated here. Chicken thigh skin (sourced from local shop) was used as a substitute for the rat skin as the thickness was roughly comparable (~1 mm thick) and more easily sourced. Porcine fat (adipose tissue; also sourced from a local shop) was used to mimic the brain by acting as a bulk scattering material. Fat has a more consistent distribution of material than brain which led to a more stable phantom for repeated measurements.

Collagen and HA plugs were created by packing the correct amount of collagen fleece and HA into a 6.3 mm diameter mold, with a small amount of water to act as a binding agent, and allowed to dry for 48 hours to make sure there was no residual water. For each measurement a single collagen/HA plug was placed into the Teflon defect. The defect was covered with the skin layer. For SORS measurements, the samples were placed on the SORS instrument with the skin side facing the laser, which laser focused on the skin at the position corresponding to the defect center.

5.3.5 Rat cadavers and skull defect

Male Sprague-Dawley rats were purchased from Charles River Ltd, 550 g at time of death, 20 weeks old and sacrificed using a schedule 1 method. All animal studies were conducted in compliance with ethical approval and in accordance with institutional guidelines.

First, the skin was shaved and peeled back from the skull to create a skin flap that could cover the defect. The skull was then drilled with a high speed Dremel rotary tool to minimize cracking or crushing the skull. The defect was drilled just through the skull layer with minimal damage to the brain underneath. The experiment was designed to maximize the similarity between the phantom and the actual skull so the hole was drilled at the center of the skull with a diameter of 6 mm. Collagen and HA plugs were created in the same way as the phantom experiment (Section 2.4) by packing the correct amount of collagen and HA into a 6 mm molds. For each measurement, a single collagen/HA plug was placed into the defect, then the defect was covered with the skin flap.

5.4   Results and Discussion

5.4.1   Investigation on phantom samples: training and validation of the PLS model for prediction of collagen concentration

Figure 5.3a describes schematically the phantoms used in this study to model the rat calvarial model. SORS spectra obtained from these phantom samples were used to train a PLS model that was used for prediction of collagen concentration for collagen:HA plugs inserted in rat cadavers. Figure 5.3b compares the SORS spectra (black lines) measured at 1.5 mm offsets with spectra measured at 0 mm offset, for samples containing increasing concentration of collagen and HA, from the minimum 0.085 g/cm^3 (Stage 1) to 0.86 g/cm^3 (Stages 3-4). For collagen:HA concentrations corresponding to Stage 1 (0.085 g/cm^3 collagen, 0 g/cm^3 HA), the spectrum measured with 0 mm spatial offset is dominated by the bands at 1445 cm^{-1} (assigned to C-H deformation vibrations in lipids and proteins), 1200-1400 cm^{-1} (assigned mainly to Amide III in proteins), 1000-1150 cm^{-1} (assigned to C-C and C-O stretching), 850 and 938 cm^{-1} bands assigned to proline and hydroxyproline in collagen (167). A small band at 1002 cm^{-1}, assigned to phenylalanine, can also be observed (167). These Raman bands are associated to collagen, lipids and other proteins in the skin layer, which is the main contributor to the Raman spectrum.
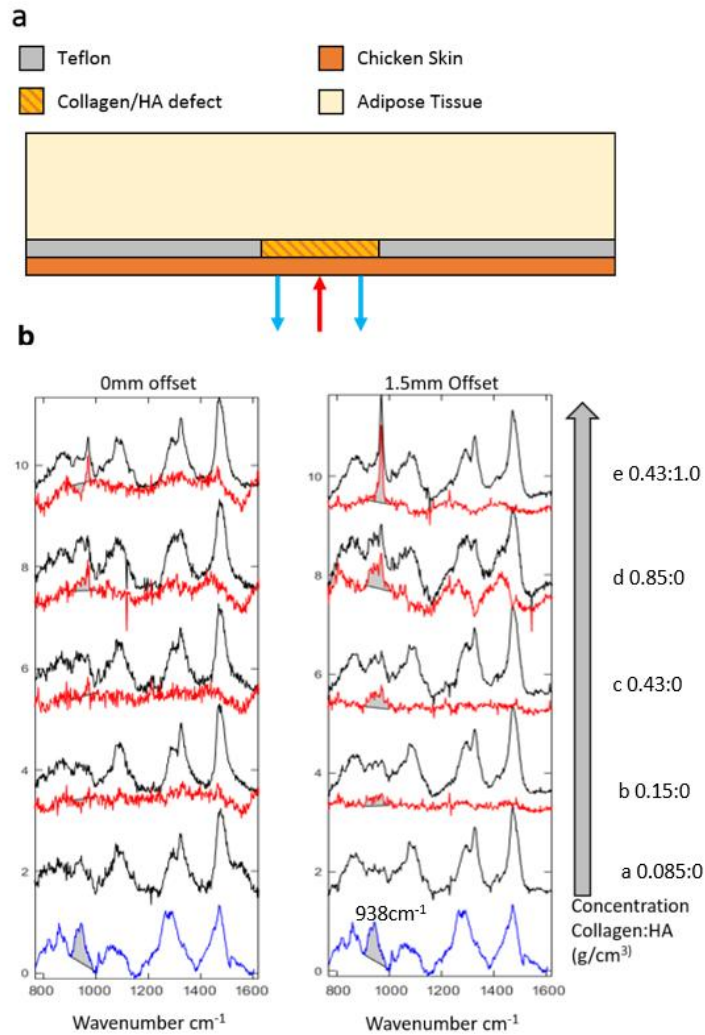
Figure 5.3 a) Schematic description of the phantom samples used to mimic the rat calvarial model. The materials are labelled by colour. The red and blue arrows indicate the laser excitation and Raman photons, respectively. b) Typical SORS spectra acquired for training the PLS model, showing for simplicity only spectra acquired at 0 mm and 1.5 mm spatial offsets. Black lines are the spectra normalized to the 1445cm^{-1} band intensity, the red lines show the spectra difference between the spectra and the 0.085g/cm^3 spectra, the blue line is collagen spectra for reference. The concentrations of collagen and HA are included in brackets.

Figure 5.3b shows a reference SORS spectrum of collagen in blue line (bovine source). Collagen has a number of bands that can be used to identify collagen from other biomolecules: 938 cm^{-1} band assigned to C-C stretch/α-helix band (167), and the 1002 cm^{-1} ring breathing peak. The 1220-1280 cm^{-1} band is also significantly different in shape to the broad 1200-1400cm^{-1} band seen from the skin. These three spectral features are highlighted on the spectra with the grey highlighted sections. Figure 5.3b shows that increasing the concentration of collagen in the defect (spectra b and c) does not change significantly the

spectra measured using a 0 mm spatial offset. This indicates that the spectra are not affected by changes in collagen concentration in the defect region. When HA is added to the defect region (spectrum d), the 960 cm^{-1} phosphate peak becomes the most intense Raman band in the spectrum, while no other significant spectral changes are observed. This shows that when selecting a 0 mm offset, the defect volume does not contribute significantly to the majority of the Raman signal, except for HA 960 cm^{-1} band, which has a much higher Raman scattering cross-section compared to the other components of the phantom sample. Spectral changes reflecting the increase in collagen concentration in the defect ore better observed in the SORS spectra measured using a 1.5 mm offset, at wavenumbers corresponding to collagen Raman bands, in particular 938 cm^{-1} C-C stretch/α-helix band. For the sample corresponding to Stage 4, HA is easily detected by the 960 cm^{-1} band, at similar intensity as for the spectrum measured at 0 mm offset.

Figure 5.4 presents the PLS models trained to predict the collagen concentration in the phantom defect based on the SORS spectra. The PLS model was built from the spectral range 800 -1606 cm^{-1} in order to avoid the Teflon band at 734 cm^{-1} (absent when applying the model on rat cadavers). The data points in Figure 5.4 represent the predicted value of collagen concentration by the leave-one-out bootstrapping. The concentration of collagen ranged from 0 to 1.1 g/cm^3 and the concentration of HA ranged from 0.0 to 2.2 g/cm^3. These collagen and HA blends were selected to cover the full range relevant to bone healing as presented in Figure 5.1.
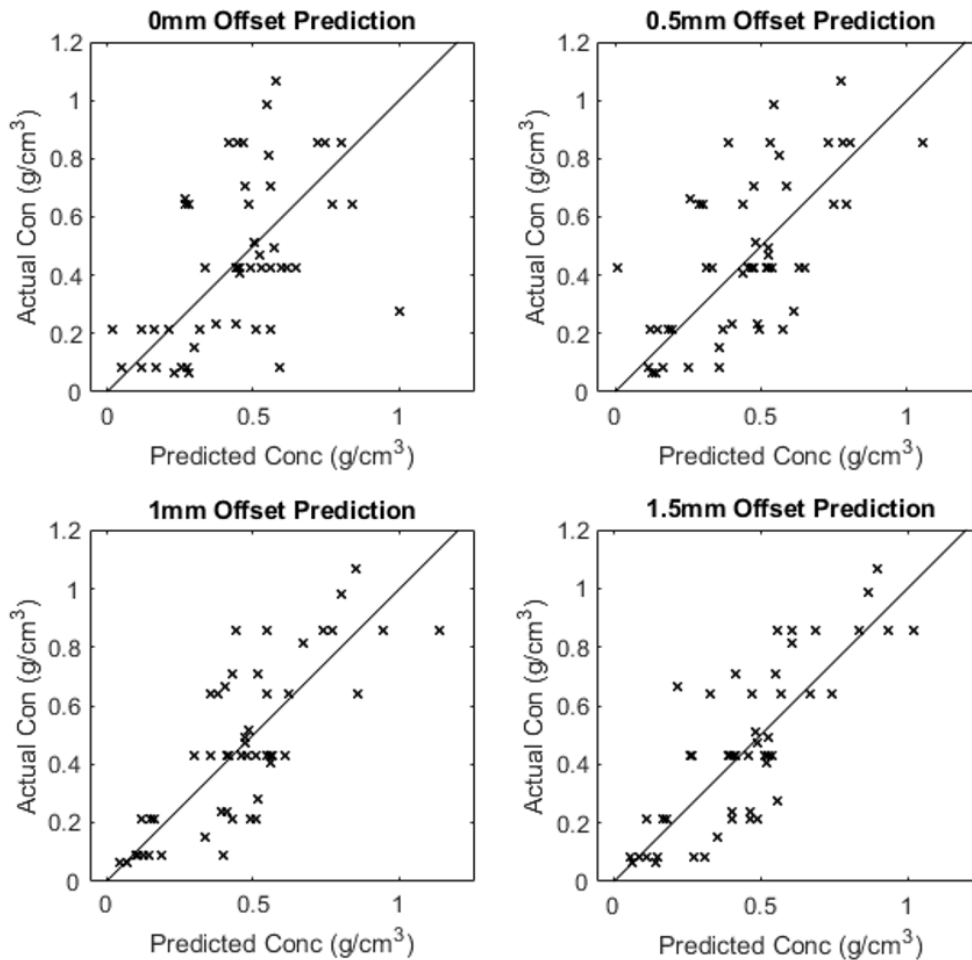
Figure 5.4 The bootstrapped data for each of the offsets for the collagen prediction each cross represents a sample with a known concentration with that concentration plotted against the predicted concentration of the model. The black line is the 1:1 relationship

The results in Figure 5.4 show that the PLS model corresponding to the 0 mm spatial offset has the lowest correlation between the predicted concentration and actual concentration of collagen with a (RMSE) of 0.24 g/cm^3. Increasing the spatial offset provides stronger signal from the collagen concentration and the performance of the prediction models increase from RMSE=0.21 g/cm^3 for 0.5 mm spatial offset, RMSE=0.17 g/cm^3 for 1 mm offset and RMSE=0.16 g/cm^3 for 1.5 mm offset.

Increasing offset has the effect of increasing the amount of signal that is detected from deep within the sample relative to the total signal generated. This means the variation in signal from a change in collagen concentration will have a greater effect on the relevant spectral bands. This increase in signal to background ratio would improve the correlation between concentration and spectra for the PLS model to be trained on. These results show that using

spatial offsets of 1-1.5 mm, it is feasible to detect changes in collagen concentration occurring within the first 2-4 days of bone regeneration (22). Nevertheless, Figure 5.4 also shows that the lowest model performance occurs for concentrations of collagen between ~0.7-0.9 g/cm^3, which corresponds to the later stage of bone regeneration. This region has an RMSE of 0.31 g/cm^3 in the 1.5 mm offset compared to the 0.17 g/cm^3 for the rest of the range. At these stages, in addition to collagen, the samples contain collagen and HA at higher concentration. The intense band at 960 cm^{-1} assigned to HA partially overlaps with the main Raman bands of collagen in the 900-1000 cm^{-1} range, affecting the prediction accuracy. In the building of the PLS model a range of skin thicknesses were used, with a range of approximately 0.5-1.0 mm. This combined with the heterogeneous nature of skin led to an unpredictable variance in the spectral contribution from skin due to the varying concentrations of collagen and fat from the skin itself. In order to build a model that takes into account skin thickness a much larger data set would be needed. As well the samples varying from the minimum to maximum concentration of HA and collagen, they would also have skin thicknesses ranging from thinnest to the thickest. Using a single offset, differentiating between high concentrations deep within the material and low concentrations close to the surface can be difficult so a model that accounts for skin thickness would likely utilize multiple offsets.

In both PLS models corresponding to 1.0 mm and 1.5 mm spatial offsets, there is a stronger prediction accuracy at lower concentrations of collagen. It is possible that this reduced performance at larger concentrations could be linked to a variety of factors. Over the course of a long measurement the collagen fibers absorb moisture from sources such as the skin. Greater concentrations of collagen could increase how much the skin dries out, affecting signal scattering. At high concentrations of collagen and HA the packing of the material into the defect was a limiting factor, as the collagen needed to be packed more densely. The change in optical properties is due to the change in the concentration of scattering material within the defect. This could lead to a concentration dependence of prediction performance. The PLS models were then tested on new phantom samples. For these samples the concentrations of collagen and hydroxyapatite were selected to match specific points of interest along the time course of bone regeneration. These samples were not included in the training dataset. The selected points were demonstrated in Table 1 referencing stages along the healing model demonstrated in Figure 5.1. These stages were selected to investigate the

ability to determine the early deposition of collagen in the sample as well as ongoing soft tissue remodeling.
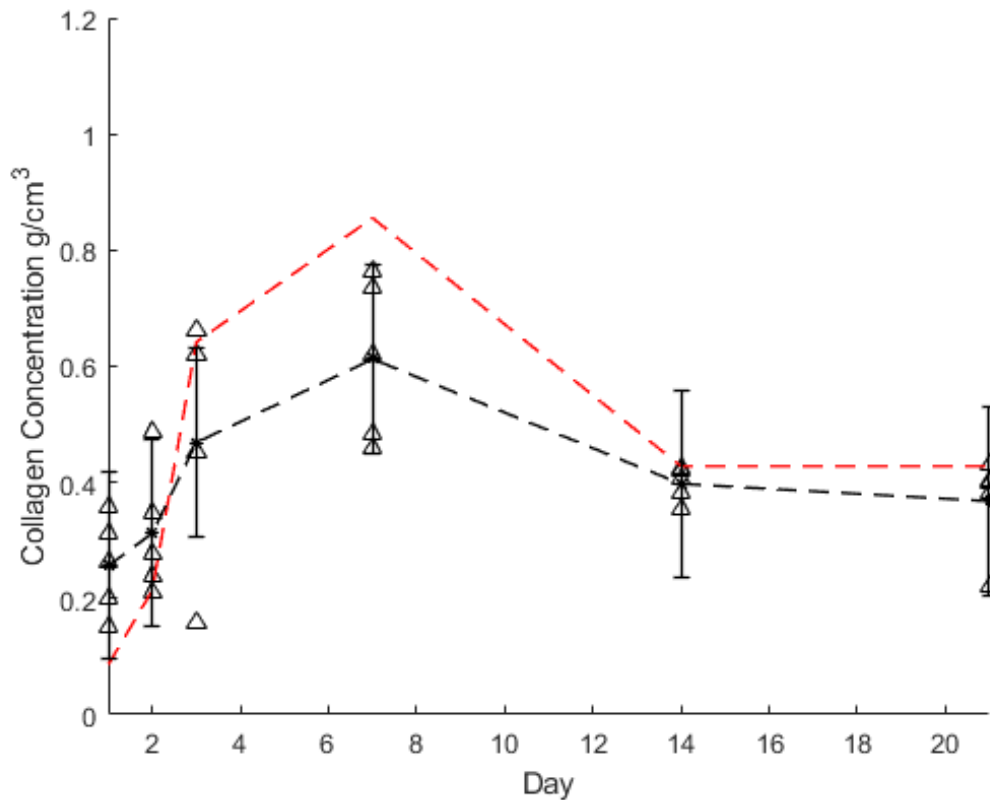
Figure 5.5: Prediction of collagen concentration for a time-course model of bone healing using phantom samples. Black triangles represent the predicted concentrations by the PLS modes (5 different samples), with the black dotted line as a guiding line for the average values. Error bars denote the uncertainties of the prediction model obtained from the boot-strapping evaluation. Red line is a guiding line for the actual collagen concentrations in the sample.

The results in Figure 5.5 show a strong correlation between the actual concentration of collagen in the test samples and the values predicted by the PLS model. The predicted values of the concentration follow the overall profile of the true concentration values and the majority are within the expected uncertainties of the PLS model, with the larger concentrations exhibiting a larger variance. The model over predicts at low collagen concentrations and under predicts high concentrations. The observed variance between the predicted concentrations for different samples is likely to be caused by variations in the thickness of the skin layers, as each sample used a different layer of skin. It is worth noting

that for in vivo measurements on the animal, the SORS spectra will be acquired from the same location therefore variations in skin thickness are less likely to occur within the same animal.

3.2. Quantification of collagen concentration in bone defects in rat cadavers

In order to investigate the feasibility of measuring collagen concentrations directly on animals, prior to live animals, experiments were carried out using rat cadavers. Bone defects were induced in the skulls of the rats and plugs of collagen:HA were inserted, then covered by the skin flaps (Figure 5.6a). The PLS model from Section 3.1 was applied on the SORS spectra measured transcutaneously by focusing the laser spot at the center of the defect location, mimicking in vivo measurements. For each animal, six collagen:HA plugs were used, using concentrations covering all six stages of bone regeneration. In total, three animals were used to evaluate inter-animal variance. Figure 5.6b presents SORS spectra measured from one of the animals covering the first four stages of simulated bone healing taken with a 1.5mm offset. In all SORS spectra, Raman bands associated to collagen can be identified mainly in the 1200-1350 cm^{-1} (amide III bands with specific higher intensity at 1240-1270 cm^{-1} compared to 1300-1350 cm^{-1}) and 850 and 950 cm^{-1}. As the spectra were normalized using the 1445cm^{-1} band, the SORS spectra measured for the samples with lower concentration of collagen (e.g. Stages 1, 2) have lower signal to noise ratio compared to the samples corresponding to Stages 3-5. The Raman band assigned to HA phosphate vibrations at 960 cm^{-1} can be identified in the SORS spectra starting with Stage 4.
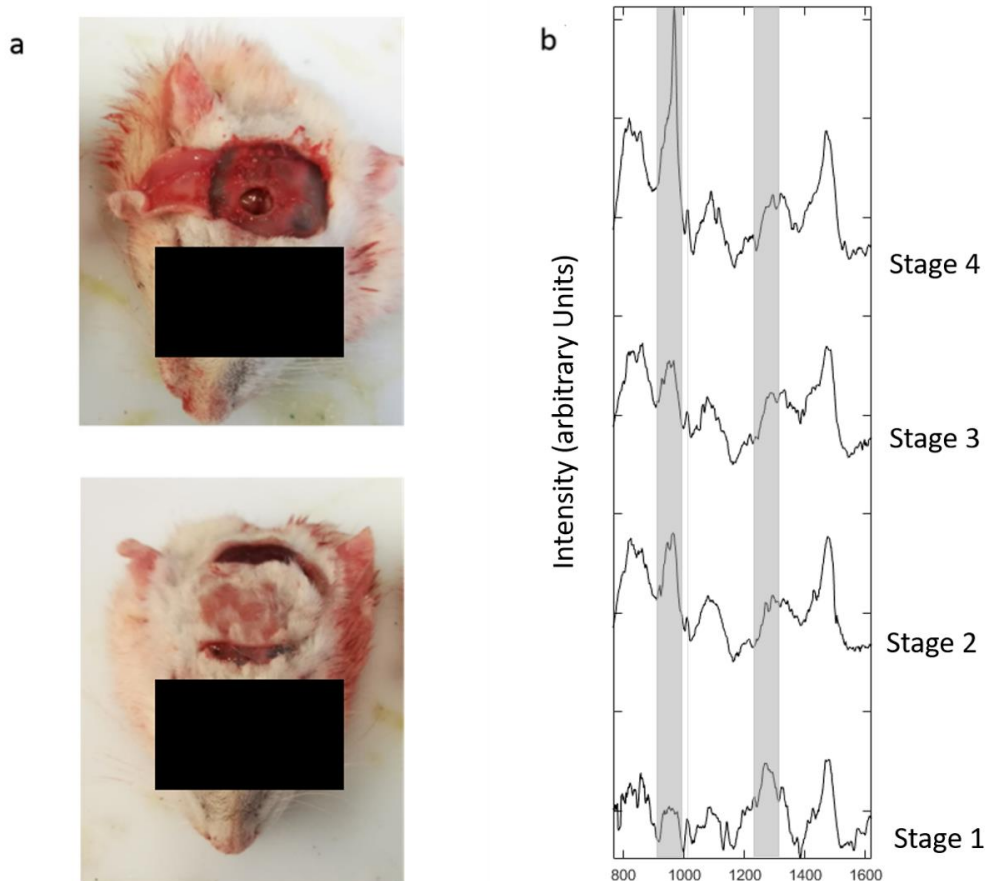
Figure 5.6: a) Photographs of a rat head used in this study, showing the defect drilled in the skull (blue arrow). b) SORS spectra obtained using collagen:HA plugs with concentrations corresponding to Stages 1 to 4 of bone regeneration (1.5 mm spatial offset). Spectra have baseline subtracted. The grey bars denote the spectral features that correlated best with collagen concentration.

Next, the PLS model developed in Section 3 was applied on the SORS spectra measured from the rat cadavers (Figure 6). The results show that, for all three animals used here, the predicted collagen values follow the correct pattern of increasing collagen from Stage 1 to Stage 4, followed by a decrease at Stages 5 and 6 of the prediction. This consistency can also be attributed to the fact that, for each animal, the thickness of the skin covering the collagen:HA plugs remained the same when changing the concentrations of collagen and HA (skin thickness was considered the main source of variance for the phantom samples). Nevertheless, the results in Figure 5.7show that the predicted values of collagen concentration were higher than the real values, by a factor of 2 to 2.5. We speculate that several factors contributed to this over prediction, both caused by differences between the

samples used for training the PLS model and the actual rat samples. Rat skin was found to be significantly thinner than the chicken skin used for training the model, there was also left-over hair on the rat skin and bone tissue surrounding the defect volume instead of Teflon for phantom sample. Furthermore, the cadaver had brain tissue as the scattering medium whereas the phantoms had porcine fat. While multiplying the predicted values of the concentration by a factor of 0.5 could provide an empirical correction, the results show that a preferable improvement in prediction accuracy could be obtained in future studies by training the PLS models with samples based on rat cadavers rather than phantoms.
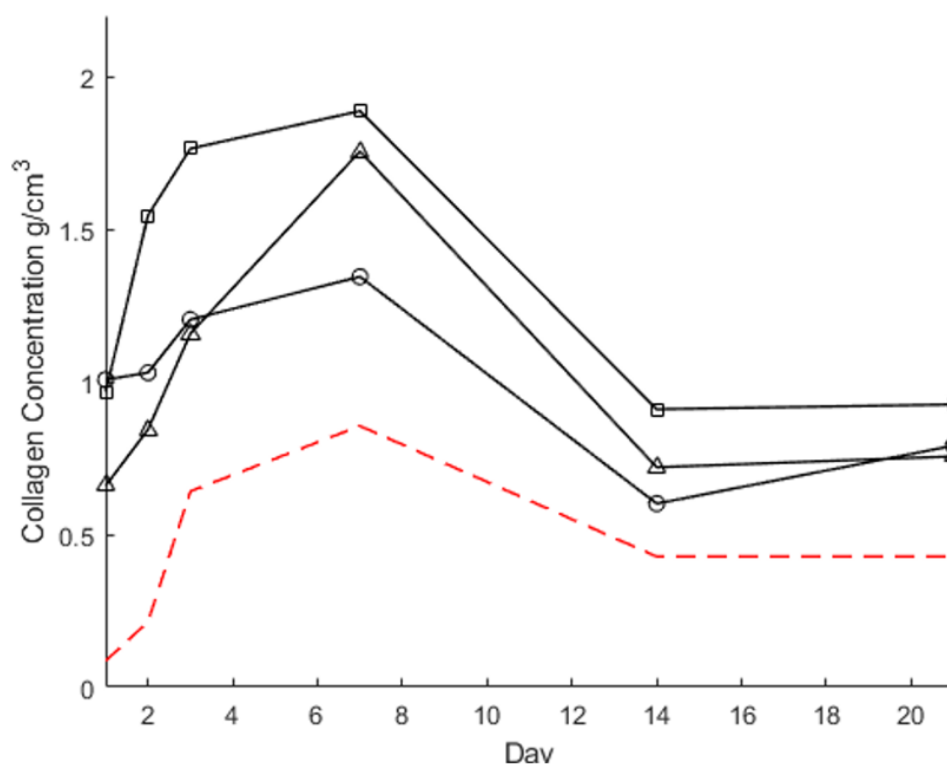
Figure 5.7: Time course model of simulated bone regeneration in a rat skull. Each symbol denotes a different rat skull, and the red line is a guide line for the actual concentration of collagen placed in the sample.

5.5   Conclusions

In this paper we showed that a SORS-based PLS model can be used to create a quantitative prediction model of collagen concentration within a phantom sample mimicking a rat calvarial defect model. The concentrations of collagen were selected to have relevant values to in vivo bone healing (0-0.86g/cm3). The predictive power was $0.16g/cm^{-1}$, and the main source of uncertainty was linked to variations in thickness of the skin layers used.

The PLS model was then used to predict the collagen concentration in collagen:HA plugs inserted in defects induced in the skull of rat cadavers. The PLS model successfully retrieved the overall pattern of collagen concentration across the concentrations simulating all stages of none healing. Nevertheless, the actual concentration values were predicted to be approximately 2-fold higher than the actual values. These over-prediction errors were associated to differences in structure and composition between the phantom samples used for training the PLS model and the actual rat cadaver samples. While the use of phantom samples for training the PLS models provides simplicity and avoids using animals, we assume that the predictive power could be improved if training is carried out on samples as similar as possible to those on which the actual measurements are to be performed.

These feasibility results indicate that SORS could be used in a non-invasive way to measure molecular changes related to bone regeneration in vivo. Such studies could generate unique longitudinal data that will provide a better understanding of the spatial and temporal molecular processes underpinning the repair of bone, that would enable the optimization the physical and chemical properties of scaffolds. The ability to follow the bone healing process on the same animal, with high chemical specificity, will provide higher quality data with ethical and economic benefits from reducing the number of animals used during the research.

6 Chapter 6

Conclusion

6.1 Overview

At the start of the PhD the aim of the project was to develop a DMD-based SORS and apply this new technique the monitoring of bone growth and healing. Building on work by Liao et al (101) the instrument was constructed from scratch and then tested on multiple samples that are highly relevant to bone monitoring samples. Through these studies, multiple improvements to the instrumentation and data analysis techniques were made which impacted and improved the efficacy of DMD-based SORS as a monitoring tool.

6.2 Summary

In Chapter 3 I discussed the instrumentation of the device, the fundamental principles that underpin the method of DMD-based SORS and the validation of the device. In Section 3.4 I demonstrated the ability of the device to separate signal from regions of interest of different geometries at depths up to 6 mm. This demonstrated the feasibility of my DMD-based SORS approach as a method for measuring biological materials within a bulk material. The results also showed that the collection pattern on the DMD can be changed quickly and easily in software according to current needs (Section 3.2).

In Chapter 4 I investigated the feasibly of using DMD-based SORS to monitor the mineralisation of bone defects in large bones. I showed that through 4 mm of porcine skin and fat it was possible to detect samples of hydroxyapatite (HA) with concentrations as low as 0.18 g/cm^3, which is approximately 10% of the density found in healthy bone, and samples with mineral density of 0.61g/cm^3 were detectable at depths up to 14 mm below the surface (Section 4.3). This was a clear demonstration of the capabilities of DMD-based SORS as a method for the monitoring of bone defects.

Having demonstrated the capacity to detect hydroxyapatite at biologically relevant concentrations at depths up to 14mm, the project moved its focus to characterisation of the extracellular matrix and organic molecules in bone (collagen). While HA in bone has been measured by other groups using SORS, measurement of collagen concentration within bone is much challenging. The concentration and Raman scattering cross section of collagen are significantly lower that that of HA. Furthermore, collagen has many similar spectral features

with other components of biological tissue such as fats and other proteins as illustrated in Figure 5.2.

Collagen deposition happens earlier in the regrowth of bone than mineralisation, so the target of this study was to investigate monitoring a greater portion of the regrowth. Using a partial least-squares (PLS) method trained on a phantom sample, I was able to create a prediction model that could predict the concentration of the collagen within a defect with a root mean square error of $0.16g/cm^3$ which is less than 20% of the maximum concentration found in healthy bone. This method was applied to rat cadavers where it successfully predicted the overall concentration profile. Nevertheless, systematic errors likely caused by differences between training and test samples led to approximately 2-fold higher predicted values compared than actual values.

The work done within these chapters showed that DMD-based SORS is a flexible tool that allowed measurements of both the mineral and soft tissue components of bone. This ranges from the growth of the extracellular matrix in the early stages of bone healing to the possibility of long-term monitoring of the mineralisation of large bone defects deep beneath thick skin and fat layers.

6.3   Key novel aspects of the instrumentation

6.3.1   What did the device do that was novel?

The major benefit of DMD-based SORS is that any collection point that is available on the DMD is an offset that can be collected from the surface of a sample. The other most common forms of SORS device are iSORS and SORS fibre probes. iSORS relies on a ring illumination with a single detection point at the centre. While this configuration increases laser power at the surface without increasing the laser power density, DMD-based SORS compensates with multiple detectors which leads to the total Raman signal collected to be similar (Section 3.2.1). Another benefit of multiple individual collection points is that spatial information is retained. While in DMD-based SORS each individual spectrum has information about the material between the excitation/collection point, ring-illuminated iSORS has only one collection point that is the summation of all the paths between the excitation and collection points.

The DMD-based SORS approach also allows the user to take measurements of multiple offsets at the same time (Section 3.2.2). Fibre optic probes do not suffer from the same

efficiency losses that DMD-based SORS does, however, once a probe is built there is only one configuration. The flexibility of DMD-based SORS is again the major strength of this type of system.

I would argue that any research group looking to build diffuse Raman systems that are optimised for specific uses would benefit from building a DMD-based system to use as a test bench for the excitation and collection patterns. It excels particularly in its ability to adapt to a new sample geometry with software changes. The only hardware change that may be required is to replace the objective lens with another of different focal length to change the range of offsets available.

6.3.2   Possible improvements to the DMD-base SORS methodology and instrumentation

1.1.1.1   *Shorten beam path length.*

Equation 3.4 shows that the overlap distance between the projected light from the objective lens, f_0, to the DMD lens, f_1, is proportional to the negative of the path length between the two lenses. Equation 3.5 and Figure 3.4 further demonstrate the increased signal losses caused by increasing path lens between these two lenses. During the construction of the device used for the experimental work of the thesis there were significant constraints on the geometry of the instrument which led to the choice of the 1000 mm path length. Figure 3.4a shows that for larger offsets, in one case of a 4mm offset with a 100 mm focal lens, reducing the path length from 1000 mm to 400 mm could more than double the overlap of the projected signal with the DMD lens; this would have a proportionate effect on the signal throughput of the system. This improvement alone would increase the signal to noise of the larger by a factor of two or more.

1.1.1.2   *Improvements that can be made with regards to the DMD selection.*

The DMD is the focus of a DMD-based SORS device and there are a few improvements that could be made to the size, configuration, and efficiency of the DMD.

A larger DMD could be used to increase the maximum range of offsets. This allows increasing maximum offsets at the sample or using shorter focal length objective lenses to achieve the same offsets. The benefits of the short focal length objective lens are the improved numerical aperture that will lead to significantly more Raman signal being collected from the sample surface. In Figure 3.5 and Table 3.1, it is demonstrated that a

shorter focal length lens leads to a higher signal throughput of the device when not at the maximum limit of its achievable offset.

Throughout this project a DLP6500 (Texas instruments) DMD was used. This DMD has a nominal window transmission efficiency of 97% though the design is for visible range. In the 785 – 900nm range that was the focus of the thesis other experimental work showed its efficiency to be much closer to 20%. Significant improvements in the DMD marketplace have been made and it is now possible to procure reasonably priced DMDs which are designed for the near-infra red region. The DLP4500NIR has a window transmission efficiency of 96% in the 700-2000nm range which would make a considerable improvement to the amount of signal that is reflected from the DMD onto the spectrometer, possibly increasing Raman signal collected by as much as three-fold.

When these improvements are considered there is significant improvement possible for DMD-based SORS instruments. By combining the signal throughput improvements that could be made by each of these improvements it may be possible to achieve a cumulative improvement in the signal collected by up to an order of magnitude at the larger offsets.

1.1.1.3 *Expanding the flexibility of DMD-based SORS by expanding the software control to the excitation laser point*

The ability to program the collection point dynamically creates a huge amount of flexibility for Raman signal collection. To build on this, the next step could be to add the ability to change the excitation point using software. By using a programmable microscope stage it is already possible to scan across the surface of a sample as with conventional Raman microscopy, this has already been done for a surface-enhanced SORS system. Since the entire imaging plane is always projected onto the DMD this does not change the relative position of the excitation point to the DMD.

By placing galvo-scanner mirrors in the excitation beam path it is possible to control the exact placement of the excitation point on the surface of the sample. A potential benefit of this method of combined control over excitation and collection points is to combine the potential benefits of iSORS with SORS. A major limiting factor in Raman signal acquisition in human and animal studies is the maximum safe limit of power density at the sample surface. Using galvo–mirror scanners to control the beam it would be possible to scan

rapidly over a small area of the sample surface. This would have the effect of spreading the power over a larger area reducing the power density to a safe level. This can then be combined with many collection points to improve total signal even further.

The final possible improvement that the galvo-scanners could bring is the ability to rapidly test configurations of excitation and detection geometries. This would allow the creation of a much more powerful tool for finding optimal configurations of excitation and collection point that would improve both signal contrast and signal to noise ratio. This capacity would open the use of DMD-base SORS not just as a tool for the implementation of spatially offset Raman spectroscopy but also as a powerful system for testing the configuration of collection and excitation points in fibre probes or iSORS.

1.1.1.4   *Combining offsets to improve prediction accuracy*

One method that improved the prediction accuracy of the model that takes advantage of the strengths of DMD-based SORS was the combination of the prediction model from multiple offsets to create a more accurate prediction model than any of the individual models alone. A basic form of this was implemented in Chapter 5 where the mean value of multiple prediction models was used. DMD-based SORS is uniquely placed as a method for collecting SORS signals in this way as it is possible to dynamically choose the collection point configurations as discussed in Chapter 3.2.4. DMD-based SORS can be used to collect multiple offsets concurrently so that a number of offsets may be combined with a single measurement.

6.4   Future work

While combining multiple separate models can help to increase prediction accuracy this does not consider the interrelationship between the different offsets chosen. Future work could include the combination of spectral features from multiple offsets to take advantage of correlations between the information with ratios of signal strength at different depths.

To improve the capacity of DMD-based SORS as a tool for monitoring of bone defects there needs to be a significant improvement in both signal contrast and signal to noise ratio. While improvements to the instrumentation have already been suggested these do not address the overlapping of spectra features that makes monitoring the collagen within a bone defect so difficult.

To gain a greater understanding of the distribution of excitation light and Raman signal within a sample I propose further work should utilise both experimental data and simulation. To follow is a description of the principles underlying these ideas of combining simulation and experimental data to optimise the geometric configurations of the excitation and detection points.

6.4.1 Improve signal contrast/ signal to noise using modelling.

NIRFAST utilises a finite element method (FEM) (168) that models photon propagation, the forward problem, with diffusion theory and then recovers the optical properties, the inverse problem, at each FEM node.

A key factor in chemical prediction in SORS is the spectra contrast, defined as the ratio of Raman photons collected that originated from a particular region of interest within the sample (ROI) relative to the Raman photons originated from outside the ROI.

$$Signal\ Contrast\ = \frac{Signal_{ROI}}{Signal_{Ref}} \qquad [6.1]$$

where $Signal_{ROI}$ is the signal generated within the region of interest that reaches the detector and $Signal_{ref}$ is the signal generated within the rest of the entire sample.

As well as signal contrast the other key factor in a Raman measurement is the signal to noise ratio (SNR). This is defined by us as

$$SNR\ = \frac{I_{ROI}}{\delta_{Background}} \qquad [6.2]$$

where $\delta_{Background}$ is the standard deviation of the background of the signal. This can be calculated by taking the standard deviation of a region of spectral that has no spectra features. In the case where the limiting spectral noise source is source noise the noise can be approximated to

$$Noise = \sqrt{Signal_{Tot}} \qquad\qquad [6.3]$$

where $Signal_{Tot}$ is the sum of the signal from the region of interest and the signal from the bulk material. This means that signal to noise ratio can be estimated within the software by:

$$SNR = \frac{Signal_{ROI}}{\sqrt{Signal_{Tot}}} \qquad\qquad [6.4]$$

Signal contrast is therefore affected by the geometry of the excitation and detection points while signal to noise ratio is affected by both the geometry and integration time. This means that the importance of signal contrast and signal to noise ratio can be balanced against one another depending on the spectral features of the materials and the integration time constraints that may be present.

6.4.2 Simulating and validating the optimisation approach for a simple sample

To demonstrate the principle of optimisation for a simple sample I designed a simple sample that would be relevant to the previous work done in this thesis. This design was a 30 x 30 x 30 mm cube of Teflon with a single defect that was 3 mm radius, 1.5 mm thick, and 1.5 mm below the surface (Figure 6.1a-b). The defect was filled with Trans-stilbene powder to generate a strong signal. The simulation software allows for multiple excitation and detection points to be simulated so two excitation points at -1mm and 0mm offset were simulated, each paired with 17 detectors from -8 mm to 8 mm offset with 1 mm intervals.
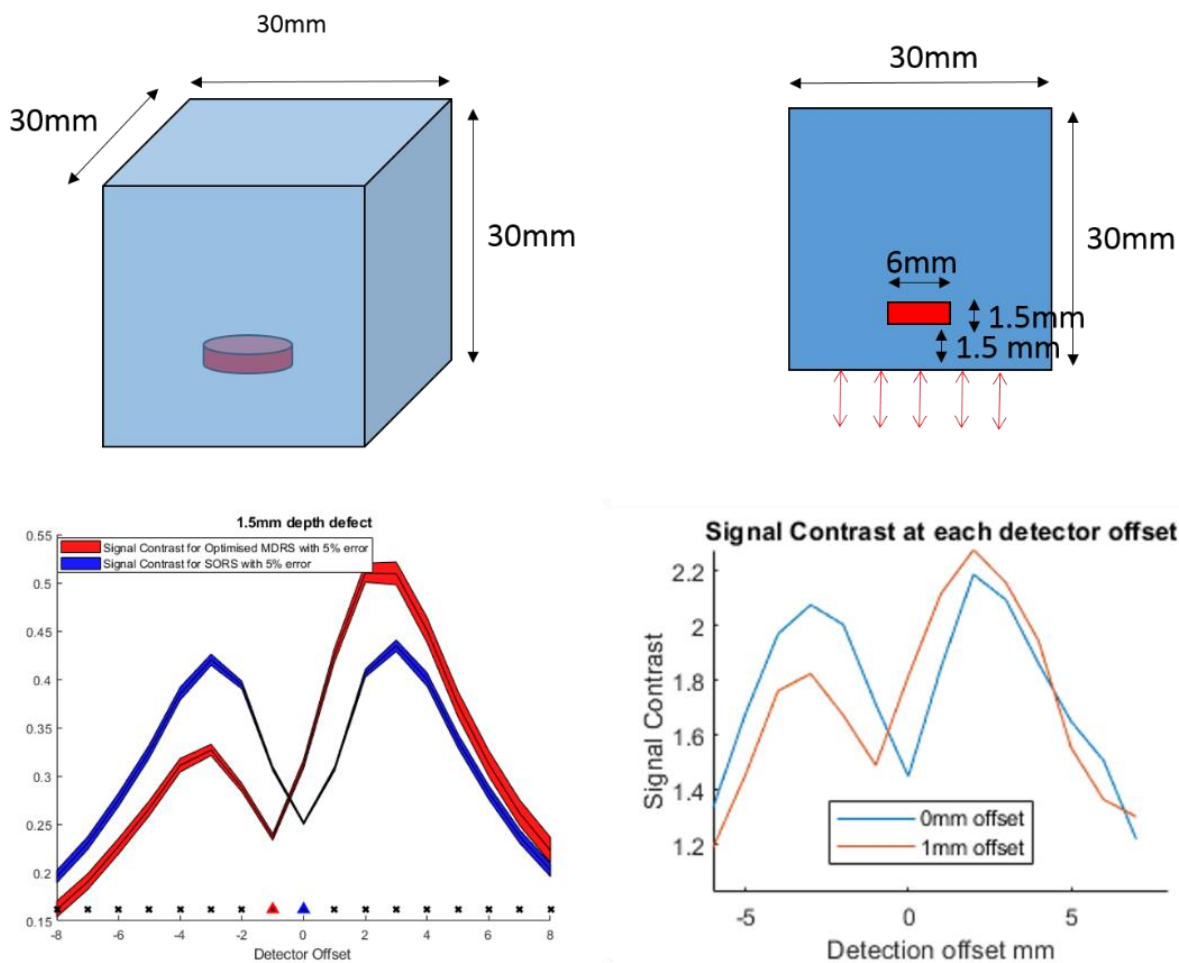
Figure 6.1 a) A three-dimensional representation of the simulated block where blue is Teflon and red is Trans-stilbene defect. b) A two-dimensional cross-section of the simulated block, the arrows denote the surface which is used to excitation and collection. c) The results of the NIRFast simulation measuring signal contrast at multiple detectors offset for two excitation points. The black crosses are the position of the detectors from the centre of the sample, the blue triangle is central excitation point and the red triangle is the -1 mm offset excitation point. The coloured area above and below the black lines show the 5% error lines generated by varying the scattering coefficients by 5% and recalculating. d) The experimental results validating the simulation; the blue line is the symmetrical SORS configuration, and the red line is the -1 mm excitation offset.

To simulate the Teflon block an estimation of the scattering coefficients as taken from previous work with NIRFast simulated plastics. Signal contrast was defined such that I_{ref} was the area under the 734cm^{-1} and I_{ROI} was the area under the 1000 cm^{-1} peak from the Tran-stilbene. The signal contrast was then calculated at each detector for the two different excitation points and plotted against the detector offset as shown in Figure 6.1c. In

order to account for the possible error in scattering coefficients the simulation was run with values for the scattering coefficients ±5% and these error bars were plotted on the graph as the area above and below the line.

Comparing the simulation, Figure 6.1c, to the experimental data, Figure 6.1d, there is a strong similarity between the two graphs. In both cases the 0mm excitation plot is symmetrical within error. Both 0 mm excitation plots have a minimum at the centre and a maximum signal contrast value at 3 mm detector offset. In both the -1mm excitation offset cases the asymmetry leads to an improvement in signal contrast at the detector offsets opposite to the excitation offset. This maximum value is close to 2-3 mm for both plots.

The point of this pilot study was not to quantify the possible improvements but rather to demonstrate two points. Firstly, that simulation software has the capacity to be used to simulate SORS measurements to fasciculate data driven decision-making regarding excitation and detection point geometries without the need for many experimentations on all geometry's samples. The qualitative similarity between Figure 6.1c and Figure 6.1d shows that the use of NIRFast has the potential to fulfil this role if scattering coefficients can be estimated.

The second goal of the proof of concept was to show that circular SORS with a central excitation point may not be optimal for all configurations. In situations where signal contrast has a greater importance than signal to noise it may be beneficial to find different configurations of excitation and detection points. Figure 6.1c and d showed that placing the excitation point asymmetrically on the sample can lead to improved signal contrast.

SORS typically utilises a greater surface area of collection or detection by using a ring of excitation/collection points. Our simple simulation of points in a straight line did not take this into account. There is potential for geometric improvements in the combination of excitation and collection points across the 2D surface of a sample. Using simulation would allow for all these configurations to be investigated and quantified.

 By combining the simulation with a DMD-based SORS device, configurations found with simulation to be quickly validated experimentally. This will likely be a powerful tool for creating future SORS systems, particularly sample specific probes which cannot be modified once built.

7 Bibliography

1. *The epidemiology of fractures in England.* **Donaldson, L.J., Reckless, I.P., Scholes, S., Mindell, J.S. and Shelton, N.J.** 2, s.l. : Journal of Epidemiology & Community Health, 2008, Vol. 62.

2. **Osteoporosis, Office of the Surgeon General (US). Bone Health and.** The Frequency of Bone Disease. 2004.

3. *Predicting the severity of motor vehicle accident injuries using models of ordered multiple choice.* **O'donnell, C.J. and Connor, D.H.** 6, s.l. : Accident Analysis & Prevention, 1996, Vol. 28.

4. **Cheng, S.Y., Levy, A.R., Lefaivre, K.A., Guy, P., Kuramoto, L. and Sobolev, B.,.** Geographic trends in incidence of hip fractures: a comprehensive literature review. *Osteoporosis International.* 22, 2011, Vol. 10.

5. **Leslie, W.D., Rubin, M.R., Schwartz, A.V. and Kanis, J.A.,.** Type 2 diabetes and bone. *Journal of Bone and Mineral Research.* 27, 2012, Vol. 11.

6. **Weitzmann, M.N. and Pacifici, R.** Estrogen deficiency and bone loss: an inflammatory tale. *Journal of clinical investigation.* 116, 2006, Vol. 5.

7. **Hu, S., Zhou, Y., Zhao, Y., Xu, Y., Zhang, F., Gu, N., Ma, J., Reynolds, M.A., Xia, Y. and Xu, H.H.,.** . Enhanced bone regeneration and visual monitoring via superparamagnetic iron oxide nanoparticle scaffold in rats. *Journal of tissue engineering and regenerative medicine.* 12, 2018, Vol. 4.

8. **Afsarimanesh, N., Mukhopadhyay, S.C. and Kruger, M.,.** Sensing technologies for monitoring of bone-health: A review. *Sensors and Actuators A: Physical.* 274, 2018.

9. **Ren, L., Yu, K. and Tan, Y.** Monitoring and assessing the degradation rate of magnesium-based artificial bone in vitro using a wireless magnetoelastic sensor. *Sensors.* 18, 2018, Vol. 9.

10. **Kanis, J.A., Harvey, N.C., Cooper, C., Johansson, H., Odén, A. and McCloskey, E.V.,.** A systematic review of intervention thresholds based on FRAX. *Archives of osteoprorsis .* 11, 2016, Vol. 1.

11. **Wen, Y., Xun, S., Haoye, M., Baichuan, S., Peng, C., Xuejian, L., Kaihong, Z., Xuan, Y., Jiang, P. and Shibi, L.,.** 3D printed porous ceramic scaffolds for bone tissue engineering: a review. *Biomaterials science.* 5, 2017, Vol. 9.

12. **Wang, M.,.** Composite scaffolds for bone tissue engineering. . *American Journal of Biochemistry and Biotechnology.* 2006.

13. **Wang, D., Gilbert, J.R., Zhang, X., Zhao, B., Ker, D.F.E. and Cooper, G.M.** Calvarial versus long bone: implications for tailoring skeletal tissue engineering. *Tissue Engineering Part B: Reviews,.* 26, 2020, Vol. 1.

14. **Kumar, P.,.** Closed plaster treatment of severe compound injuries–A report and revisit. *Apollo Medicine.* 11, 2014, Vol. 2.

15. **Cooper, G.M., Mooney, M.P., Gosain, A.K., Campbell, P.G., Losee, J.E. and Huard, J.** Testing the "critical-size" in calvarial bone defects: revisiting the concept of a critical-sized defect (CSD). *Plastic and reconstructive surgery.* 125, 2010, Vol. 6.

16. **Schemitsch, E.H.,.** . Size matters: defining critical in bone defect size!. . *Journal of orthopaedic trauma,.* 31, 2017.

17. **Strube, P., Sentuerk, U., Riha, T., Kaspar, K., Mueller, M., Kasper, G., Matziolis, G., Duda, G.N. and Perka, C.** Influence of age and mechanical stability on bone defect healing: age reverses mechanical effects. *Bone.* 42, 2008, Vol. 4.

18. **Peterson, B., Zhang, J., Iglesias, R., Kabo, M., Hedrick, M., Benhaim, P. and Lieberman, J.R.** Healing of critically sized femoral defects, using genetically modified mesenchymal stem cells from human adipose tissue. *Tissue engineering.* 11, 2005, Vols. 1-2.

19. **Follet, Hélène, Georges Boivin, C. Rumelhart, and P. J. Meunier.** The degree of mineralization is a determinant of bone strength: a study on human calcanei. *Bone.* 34, 2004, Vol. 5.

20. **Wachter, N.J., Krischak, G.D., Mentzel, M., Sarkar, M.R., Ebinger, T., Kinzl, L., Claes, L. and Augat, P.** Correlation of bone mineral density with strength and microstructural parameters of cortical bone in vitro. . *Bone,.* 31, 2002, Vol. 1.

21. **Sodek, K.L., Tupy, J.H., Sodek, J. and Grynpas, M.D.,.** Relationships between bone protein and mineral in developing porcine long bone and calvaria. *Bone.* 26, 2000, Vol. 2.

22. **Pivonka, P. and Dunstan, C.R.** Role of mathematical modeling in bone fracture healing. *BoneKEy.* 1, 2012. .

23. **Spiegel, P.K.** The first clinical X-ray made in America--100 years. *American journal of roentgenology.* 164, 1995, Vol. 1.

24. *Optimizing the x-ray photon energy for digital radiographic imaging systems.* **Huda, Walter, et al.** 2002, SPIE procedings , Vol. 4682.

25. *Attenuation Coefficients of Various Body Tissues, Fluids, and Lesion at Photon Energies of 18 to 13 KeV.* **Michael E. Phelps, Edward J. Hoffman, Michel M. Ter-Pogossian.** s.l. : Radiology, 1975, Vol. 117.

26. **Aviv, J.E.,.** Prospective, randomized outcome study of endoscopy versus modified barium swallow in patients with dysphagia. . *The Laryngoscope,.* 110, 2000, Vol. 4.

27. **Wells, I.T.P., Raju, V.M., Rowberry, B.K., Johns, S., Freeman, S.J. and Wells, I.P.,.** Digital tomosynthesis—a new lease of life for the intravenous urogram?. . *The British journal of radiology.* 84, 2011, Vol. 1001.

28. *Risk-Benefit Analysis of X-Ray Exposure Associated with Lung Cancer Screening in the Italung-CT Trial.* **Mario Mascalchi1, Giacomo Belli2, Marco Zappa3, Giulia Picozzi1, Massimo Falchini1, Riccardo Della Nave1, Germana Allescia1, Andrea Masi4, Andrea Lopes Pegna5, Natale Villari1 and Eugenio Paci.** s.l. : American Journal of Roentgenology, 2006, Vol. 187.

29. *Diagnostic X-ray and ultrasound exposure and risk of childhood cancer.* **X-O Shu, F Jin, MS Linet, W Zheng, J Clemens, J Mills & Y-T Gao.** s.l. : British Journal of CAncer, 1994, Vol. 70.

30. *Radiation exposure to medical staff in interventional and cardiac radiology.* **E Vañó, L González, E Guibelalde, J M Fernández, and J I Ten.** s.l. : The british Institute of Radiology, 1998, Vol. 71.

31. **Lee, J.K.** *Computed body tomography with MRI correlation.* s.l. : Lippincott Williams & Wilkins.

32. *Effective Doses in Radiology and Diagnostic Nuclear Medicine: A Catalog.* **FA, Mettler.** s.l. : Radiology, 2008, Vol. 248.

33. *A biodegradable antibiotic-impregnated scaffold to prevent osteomyelitis in a contaminated in vivo bone defect model.* **Jane S. McLaren, Leslie J. White, Helen Cox, Warda Ashraf, Cheryl V. Rahman, Gordon William Blunn, Allen E Goodship, Robin A. Quirk, Kevin M. Shakesheff, Roger Bayston, Brigitte E Scammell.** s.l. : European cells & materials, 2014.

34. *Ovine Model for Critical-Size Tibial Segmental Defects.* **Chris Christou, Rema A Oliver, Matthew H Pelletier, William R Walsh.** s.l. : Comp Med, 2014, Vol. 64.

35. **Rzeszowska-Wolny, J., Przybyszewski, W.M. and Widel, M.,.** Ionizing radiation-induced bystander effects, potential targets for modulation of radiotherapy. *European journal of pharmacology,.* 625, 2009, Vols. 1-3.

36. **Pietrobelli, A.N.G.E.L.O., Formica, C., Wang, Z.I.M.I.A.N. and Heymsfield, S.B.** Dual-energy X-ray absorptiometry body composition model: review of physical concepts. *American Journal of Physiology-Endocrinology And Metabolism, .* 271, 1996, Vol. 6.

37. **Nana, A., Slater, G.J., Stewart, A.D. and Burke, L.M.,.** Methodology review: using dual-energy X-ray absorptiometry (DXA) for the assessment of body composition in athletes and active people. *International journal of sport nutrition and exercise metabolism .* 25, 2015, Vol. 2.

38. **Hoogbergen, M.M., Rijnders, W., VAN DONGEN, A.J., Anema, P.C., VAN RIJK, P.P., Spauwen, P.H. and Kauer, J.M.** The long-term effects of force-transmission in an injured

wrist, measured with dual-energy X-ray absorphometry: a case report. . *Clinical nuclear medicine.* 25, 2000, Vol. 2.

39. *Radiation exposure in X-ray-based imaging techniques used in osteoporosis.* **John Damilakis, Judith E. Adams, Giuseppe Guglielmi, and Thomas M. Link.** 11, s.l. : European Radiology, 2010, Vol. 20.

40. **Steinbach, L.S. and Smith, D.K.** MRI of the wrist. *Clinical imaging.* 24, 2000, Vol. 5.

41. **Huellner, M.W., Bürkert, A., Strobel, K., Lago, M.D.S.P., Werner, L., Hug, U., von Wartburg, U., Seifert, B. and Veit-Haibach, P.** Imaging non-specific wrist pain: interobserver agreement and diagnostic accuracy of SPECT/CT, MRI, CT, bone scan and plain radiographs. *PloS one .* 8, 2013, Vol. 12.

42. **Claes, L., Recknagel, S. and Ignatius, A.** Fracture healing under healthy and inflammatory conditions. *Nature Reviews Rheumatology.* 8, 2012, Vol. 3.

43. **Saito, M. and Marumo, K.M.S.K.M.** Collagen cross-links as a determinant of bone quality: a possible explanation for bone fragility in aging, osteoporosis, and diabetes mellitus. *Osteoporosis international, .* 21, 2010, Vol. 2.

44. **McLaren, J.S., White, L.J., Cox, H.C., Ashraf, W., Rahman, C.V., Blunn, G.W., Goodship, A.E., Quirk, R.A., Shakesheff, K.M., Bayston, R. and Scammell, B.E.** A biodegradable antibiotic-impregnated scaffold to prevent osteomyelitis in a contaminated in vivo bone defect model. *European Cells and Materials.* 27, 2014.

45. **Naghieh, S., Ravari, M.K., Badrossamay, M., Foroozmehr, E. and Kadkhodaei, M.,.** Numerical investigation of the mechanical properties of the additive manufactured bone scaffolds fabricated by FDM: the effect of layer penetration and post-heating. . *Journal of the mechanical behavior of biomedical materials,.* 59, 2016.

46. **Duarte, P.M., Neto, J.B.C., Gonçalves, P.F., Sallum, E.A. and Nociti Jr, F.H.,.** Estrogen deficiency affects bone healing around titanium implants: a histometric study in rats. *Implant dentistry.* 12, 2003, Vol. 4.

47. **Phelps, M.E., Hoffman, E.J. and Ter-Pogossian, M.M.,.** Attenuation coefficients of various body tissues, fluids, and lesions at photon energies of 18 to 136 keV. *Radiology.* 117, 1975, Vol. 3.

48. **Lian, J.B. and Stein, G.S.** Development of the osteoblast phenotype: molecular mechanisms mediating osteoblast growth and differentiation. *The Iowa orthopaedic journal.* 15, 1995.

49. **Goulet, J.A., Senunas, L.E., DeSilva, G.L. and Greenfield, M.L.V.** Autogenous iliac crest bone graft: complications and functional assessment. . *Clinical Orthopaedics and Related Research.* 339, 1997.

50. **Albrektsson, T. and Johansson.** Osteoinduction, osteoconduction and osseointegration. *European spine journal.* 10, 2001, Vol. 2.

51. **Flint, P.W., Corio, R.L. and Cummings, C.W.,.** Comparison of soft tissue response in rabbits following laryngeal implantation with hydroxylapatite, silicone rubber, and Teflon. *Annals of Otology, Rhinology & Laryngology,.* 106, 1997, Vol. 5.

52. **Lee, Ji-Hyun, Chang-Sung Kim, Kyung-Hee Choi, Ui-Won Jung, Jeong-Ho Yun, Seong-Ho Choi, and Kyoo-Sung Cho.** The induction of bone formation in rat calvarial defects and subcutaneous tissues by recombinant human BMP-2, produced in Escherichia coli. *Biomaterials.* 31, 2010, Vol. 13.

53. **Lee, J.H., Kim, C.S., Choi, K.H., Jung, U.W., Yun, J.H., Choi, S.H. and Cho, K.S.,.** The induction of bone formation in rat calvarial defects and subcutaneous tissues by recombinant human BMP-2, produced in Escherichia coli. *Biomaterials.* 31, 2010, Vol. 13.

54. **DeBruijn, J.D., Van Den Brink, I., Mendes, S., Dekker, R., Bovell, Y.P. and Van Blitterswijk, C.A.** Bone induction by implants coated with cultured osteogenic bone marrow cells. *Advances in dental research,.* 13, 1999, Vol. 1.

55. **van de Vijfeijken, S.E., Münker, T.J., Spijker, R., Karssemakers, L.H., Vandertop, W.P., Becking, A.G., Ubbink, D.T., Becking, A.G., Dubois, L., Karssemakers, L.H.E. and Milstein, D.M.J.** Autologous bone is inferior to alloplastic cranioplasties: safety of autograft and allograft materials for cranioplasties, a systematic review. *World neurosurgery.* 117, 2018.

56. **Sen, M.K. and Miclau, T.** Autologous iliac crest bone graft: should it still be the gold standard for treating nonunions? *Injury.* 38, 2007, Vol. 1.

57. **Sohn, H.S. and Oh, J.K.** Review of bone graft and bone substitutes with an emphasis on fracture surgeries. *Biomatterials research.* 23, 2019, Vol. 1.

58. **Campana, V., Milano, G.I.U.S.E.P.P.E., Pagano, E., Barba, M., Cicione, C., Salonna, G., Lattanzi, W. and Logroscino, G.** Bone substitutes in orthopaedic surgery: from basic science to clinical practice. . *Journal of Materials Science: Materials in Medicine, .* 25, 2014, Vol. 10.

59. **Hammoudeh, Jeffrey A., Artur Fahradyan, Daniel J. Gould, Fan Liang, Thomas Imahiyerobo, Leo Urbinelli, JoAnna T. Nguyen, William Magee, Stephen Yen, and Mark M. Urata.** A comparative analysis of recombinant human bone morphogenetic protein-2 with a demineralized bone matrix versus iliac crest bone graft for secondary alveolar bone grafts in patients with cleft lip and palate: review of 501 cases. *Plastic and reconstructive surgery .* 140, 2017, Vol. 2.

60. **Saha, A.K., Samaddar, S., Kumar, A., Chakraborty, A. and Deb, B.** A Comparative Study of Orbital Blow Out Fracture Repair, Using Autogenous Bone Graft and Alloplastic Materials. *Indian Journal of Otolaryngology and Head & Neck Surgery.* 71, 2019, Vol. 4.

61. **Lyons, F.G., Al-Munajjed, A.A., Kieran, S.M., Toner, M.E., Murphy, C.M., Duffy, G.P. and O'Brien, F.J.** he healing of bony defects by cell-free collagen-based scaffolds compared to stem cell-seeded tissue engineered constructs. *Biomaterials.* 31, 2010, Vol. 5.

62. **Do Amaral, R.J., Zayed, N., Pascu, E.I., Cavanagh, B., Hobbs, C., Santarella, F., Simpson, C.R., Murphy, C.M., Sridharan, R., González-Vázquez, A. and O'sullivan, B.,.** Functionalising

collagen-based scaffolds with platelet-rich plasma for enhanced skin wound healing potential. *Frontiers in bioengineering and biotechnology,.* 7, 2019.

63. **Yang, Y., Yang, S., Wang, Y., Yu, Z., Ao, H., Zhang, H., Qin, L., Guillaume, O., Eglin, D., Richards, R.G. and Tang, T.** Anti-infective efficacy, cytocompatibility and biocompatibility of a 3D-printed osteoconductive composite scaffold functionalized with quaternized chitosan. *Acta biomaterialia.* 46, 2016.

64. **McLaren, J.S., White, L.J., Cox, H.C., Ashraf, W., Rahman, C.V., Blunn, G.W., Goodship, A.E., Quirk, R.A., Shakesheff, K.M., Bayston, R. and Scammell, B.E.,.** A biodegradable antibiotic-impregnated scaffold to prevent osteomyelitis in a contaminated in vivo bone defect model. *European Cells and MAterials.* 27, 2014.

65. **Shor, L., Güçeri, S., Wen, X., Gandhi, M. and Sun, W.** Fabrication of three-dimensional polycaprolactone/hydroxyapatite tissue scaffolds and osteoblast-scaffold interactions in vitro. *Biomaterials.* 28, 2007, Vol. 35.

66. **Hollister, S.J.** Porous scaffold design for tissue engineering. *Nature materials.* 4, 2005, Vol. 7.

67. **Hing, K.A., Wilson, L.F. and Buckland, T.,.** Comparative performance of three ceramic bone graft substitutes. *The Spine Journal.* 7, 2007, Vol. 4.

68. **Liu, Y., Lim, J. and Teoh, S.H.,.** Development of clinically relevant scaffolds for vascularised bone tissue engineering. . *Biotechnology advances,.* 31, 2013, Vol. 5.

69. **Eliasson, C. and Matousek, P.,.** Noninvasive authentication of pharmaceutical products through packaging using spatially offset Raman spectroscopy. *Analytical Chemistry.* 79, 2007, Vol. 4.

70. *Raman spectroscopy: techniques and applications in the life sciences.* **Shipp, D.W., Sinjab, F. and Notingher, I.** 2, 2017, Advances in Optics and Photonics, Vol. 9, pp. 315-428.

71. **Smith, E. and Dent.** *Modern Raman spectroscopy: a practical approach.* s.l. : ohn Wiley & Sons., 2019.

72. *A review of the theory and application of coherent anti-Stokes Raman spectroscopy (CARS).* **Tolles, W.M., Nibler, J.W., McDonald, J.R. and Harvey, A.B.,.** 4, 1977, Applied Spectroscopy, Vol. 31, pp. 253-271.

73. **Jackson, J.D.** *Classical electrodynamics.* s.l. : John Wiley & Sons., 2007.

74. *Contrastive analysis of the Raman spectra of polychlorinated benzene: hexachlorobenzene and benzene.* **Zhang, X., Zhou, Q., Huang, Y., Li, Z. and Zhang, Z.** 2, 2011, Sensors, Vol. 11, pp. 11510-11515.

75. *Performance comparisons of conventional and line-focused surface Raman spectrometers.* **Ramsey, J., Ranganathan, S., McCreery, R.L. and Zhao, J.** 6, 2001, Applied Spectroscopy, Vol. 55, pp. 767-773.

76. **Demtröder, W., 2014.** *Laser spectroscopy 1: basic principles. Springer.* s.l. : Springer, 2014.

77. **Mayerhöfer, T.G. and Popp, J.** Quantitative Evaluation of Infrared Absorbance Spectra– Lorentz Profile versus Lorentz Oscillator. *ChemPhysChem,.* 20, Vol. 20, 1.

78. *Critical-depth Raman spectroscopy enables home-use non-invasive glucose monitoring.* **Lundsgaard-Nielsen, S.M., Pors, A., Banke, S.O., Henriksen, J.E., Hepp, D.K. and Weber, A.,.** 5, 2018, PloS one, Vol. 13, p. 0197134.

79. *3D confocal Raman imaging of endothelial cells and vascular wall: perspectives in analytical spectroscopy of biomedical research.* **Majzner, K., Kaczor, A., Kachamakova-Trojanowska, N., Fedorowicz, A., Chlopicki, S. and Baranska, M., 2013.** 2, 2013, Analyst, Vol. 138, pp. 603-610.

80. *Spatially offset Raman microspectroscopy of highly scattering tissue: theory and experiment.* **Di, Z., Hokr, B.H., Cai, H., Wang, K., Yakovlev, V.V., Sokolov, A.V. and Scully, M.O.,.** 2015, Journal of Modern Optics, pp. 97-101.

81. *Surface-enhanced, spatially offset Raman spectroscopy (SESORS) in tissue analogues.* **Asiala, S.M., Shand, N.C., Faulds, K. and Graham, D.,.** 30, 2017, ACS applied materials & interfaces, Vol. 9, pp. 25488-25494.

82. *Spatially offset Raman spectroscopy (SORS) for the analysis and detection of packaged pharmaceuticals and concealed drugs.* **Olds, W.J., Jaatinen, E., Fredericks, P., Cletus, B., Panayiotou, H. and Izake, E.L.** 1-3, 2011, Forensic science international, Vol. 212, pp. 69-77.

83. *Highly efficient spatially offset Raman spectroscopy to profile molecular composition in bone.* **Cui, H., Glidle, A. and Cooper, J.M.** 2020, IEEE Access, Vol. 8, pp. 62905-62911.

84. **Keller, M.D., Majumder, S.K. and Mahadevan-Jansen, A.** Spatially offset Raman spectroscopy of layered soft tissues. *Optics letters.* 34, 2009., Vol. 7.

85. *Spatially Offset and Transmission Raman Spectroscopy for Determination of Depth of Inclusion in Turbid Matrix.* **Mosca, S., Dey, P., Tabish, T.A., Palombo, F., Stone, N. and Matousek, P.** 14, 2019, Analytical chemistry, Vol. 91, pp. 8994-9000.

86. *Contributions of Raman spectroscopy to the understanding of bone strength.* **Mandair, G.S. and Morris, M.D.** 2015, BoneKEy reports, Vol. 4.

87. *The associations between mineral crystallinity and the mechanical properties of human cortical bone.* **Yerramshetty JS, Akkus O.** 2008, Bone, Vol. 42, pp. 476-482.

88. *Complementary information on in vitro.* **Kazanci M, Fratzl P, Klaushofer K, Paschalis EP.** 2006, Calcif Tissue Int, Vol. 79, pp. 354-359.

89. *Carbonate assignment and calibration in the raman.* **Awonusi A, Morris MD, Tecklenburg MMJ.** 2007, Calcif Tissue Int, Vol. 81, pp. 46-52.

90. *Spatially Offset Raman Spectroscopy for photon migration investigations in long bone.* **Sowoidnich, K., Churchwell, J.H., Buckley, K., Kerns, J.G., Goodship, A.E., Parker, A.W. and Matousek, P.,.** 2015, European Conference on Biomedical Optics, p. 954009.

91. *Ultrastructural changes accompanying the mechanical deformation of bone tissue: A Raman imaging study.* **arden A, Rajachar RM, Morris MD, Kohn DH.** 2003, Calcif Tissue Int, Vol. 72, pp. 166-175.

92. *Spectroscopic characterization of collagen cross-links in bone.* **Awonusi A, Morris MD, Tecklenburg MMJ.** 81, Calcif Tissue Int, pp. 46-52.

93. *Age-related changes in reducible crosslinks of human dental pulp collagen. .* **Nielsen, C.J., Bentley, J.P. and Marshall, F.J.,.** 1983, Archives of Oral Biology,, pp. 759-64.

94. *Highly efficient spatially offset Raman spectroscopy to profile molecular composition in bone. .* **Cui, H., Glidle, A. and Cooper, J.M.,.** 2020, IEEE Access, pp. 62905-62911.

95. *Measurement of abnormal bone composition in vivo using noninvasive Raman spectroscopy.* **Buckley, K., Kerns, J., Gikas, P.D., Birch, H., Vinton, J., Keen, R., Parker, A.W., Matousek, P. and Goodship, A.,.** 2014, IBMS BoneKEy, pp. 1-3.

96. *Sensitivity of spatially offset Raman spectroscopy (SORS) to subcortical bone tissue.* **Feng, G., Ochoa, M., Maher, J.R., Awad, H.A. and Berger, A.J.,.** 8, 2017, Journal of biophotonics, Vol. 10, pp. 990-996.

97. *Overconstrained library-based fitting method reveals age-and disease-related differences in transcutaneous Raman spectra of murine bones. .* **Maher, J.R., Inzana, J.A., Awad, H.A. and Berger, A.J.,.** 7, 2031, Journal of biomedical, Vol. 18, p. 077001.

98. *Contributions of Raman spectroscopy to the understanding of bone strength.* **Mandair, G.S. and Morris, M.D.,.** 20115, BoneKEy reoirts, p. 4.

99. *Noninvasive Raman tomographic imaging of canine bone tissue.* **Schulmerich, M.V., Cole, J.H., Dooley, K.A., Morris, M.D., Kreider, J., Goldstein, S.A., Srinivasan, S. and Pogue, B.W.,.** 2008, Journal of biomedical optics, p. 020506.

100. *Next-generation Raman tomography instrument for non-invasive in vivo bone imaging. .* **Demers, J.L.H., Esmonde-White, F.W., Esmonde-White, K.A., Morris, M.D. and Pogue, B.W.,.** 2015, Biomedical optice express, pp. 793-806.

101. *DMD-based software-configurable spatially-offset Raman spectroscopy for spectral depth-profiling of optically turbid samples.* **Liao, Z., Sinjab, F., Gibson, G., Padgett, M. and Notingher, I.** 12, 2016, Optics express,, Vol. 24, pp. 12701-12712.

102. *Noninvasive Raman Spectroscopy of Human Tissue In Vivo.* **PAVEL MATOUSEK, * EDWARD R. C. DRAPER, ALLEN E. GOODSHIP, IAN P. CLARK,.** 2006, Applied spectroscopy,, pp. 1341-1347.

103. *Time-resolved spatially offset Raman spectroscopy for depth analysis of diffusely scattering layers.* **Petterson, I.E.I., Dvořák, P., Buijs, J.B., Gooijer, C. and Ariese, F.,.** 2010, Analyst, pp. 3255-3259.

104. *Decomposition of in vivo spatially offset Raman spectroscopy data using multivariate analysis techniques.* **Buckley, K., Kerns, J.G., Parker, A.W., Goodship, A.E. and Matousek, P.** 2014, Journal of Raman Spectroscopy, pp. 188-192.

105. *Prediction of sublayer depth in turbid media using spatially offset Raman spectroscopy.* **MacLeod, N.A., Goodship, A., Parker, A.W. and Matousek, P.** 2008, Analytical CHemistry, pp. 8146-8152.

106. *Numerical simulations of subsurface probing in diffusely scattering media using spatially offset Raman spectroscopy. .* **Matousek, P., Morris, M.D., Everall, N., Clark, I.P., Towrie, M., Draper, E., Goodship, A. and Parker, A.W.,.** 2005, Applied spectroscopy, pp. 1485-1492.

107. *Spatially offset Raman spectroscopy for photon migration studies in bones with different mineralization levels.* **Sowoidnich, K., Churchwell, J.H., Buckley, K., Goodship, A.E., Parker, A.W. and Matousek, P.,.** 17, 2017, Analyst, Vol. 142, pp. 3219-3226.

108. *Noninvasive Raman spectroscopy of rat tibiae: approach to in vivo assessment of bone quality.* **Okagbare, P.I., Morris, M.D., Begun, D., Goldstein, S.A. and Tecklenburg, M.** 2012, Journal of biomedical optics,, p. 090502.

109. *Multichannel diffuse optical Raman tomography for bone characterization in vivo: a phantom.* **Demers, J.L.H., Davis, S.C., Pogue, B.W. and Morris, M.D.,.** 2012, Biomedical optics express,, pp. 2299-2305.

110. *Spatially offset Raman spectroscopy for in vivo bone strength prediction.* **Shu, C., Chen, K., Lynch, M., Maher, J.R., Awad, H.A. and Berger, A.J.,.** 10, 2018, Biomedical optics, Vol. 9, pp. 4781-91.

111. *Soft-tissue spectral subtraction improves transcutaneous Raman estimates of murine bone strength in vivo.* **Chen, K., Massie, C. and Berger, A.J.,.** 2020, Journal of Biophotonics, p. 202000256.

112. *Mixture analysis using reverse searching and non-negative least squares.* **Zhang, Z.M., Chen, X.Q., Lu, H.M., Liang, Y.Z., Fan, W., Xu, D., Zhou, J., Ye, F. and Yang, Z.Y.** 2014, Chemometrics and Intelligent Laboratory Systems, Vol. 137, pp. 10-20.

113. **Wróbel, M.S., Jedrzejewska-Szczerska, M., Galla, S., Piechowski, L., Sawczak, M., Popov, A.P., Bykov, A.V., Tuchin, V.V. and Cenian.** Use of optical skin phantoms for preclinical evaluation of laser efficiency for skin lesion therapy. *Journal of biomedical optics.* 20, 2015, Vol. 8.

114. **Lai, P., Xu, X. and Wang, L.V.,.** Dependence of optical scattering from Intralipid in gelatin-gel based tissue-mimicking phantoms on mixing temperature and time. *Journal of biomedical optics.* 19, 2014, Vol. 3.

115. **Pogue, B.W. and Patterson, M.S.** Review of tissue simulating phantoms for optical spectroscopy, imaging and dosimetry. *Journal of biomedical optics.* 11, 2006, Vol. 4.

116. **Dooley, M., Prasopthum, A., Liao, Z., Sinjab, F., McLaren, J., Rose, F.R., Yang, J. and Notingher, I.** Spatially-offset Raman spectroscopy for monitoring mineralization of bone tissue engineering scaffolds: feasibility study based on phantom samples. *Biomedical optics express.* 10, 2019, Vol. 4.

117. **Okagbare, P.I., Morris, M.D., Begun, D., Goldstein, S.A. and Tecklenburg, M.** Noninvasive Raman spectroscopy of rat tibiae: approach to in vivo assessment of bone quality. *Journal of biomedical optics.* 17, 2012, Vol. 9.

118. **Dooley, M., McLaren, J., Rose, F.R. and Notingher, I.,.** Investigating the feasibility of spatially offset Raman spectroscopy for in-vivo monitoring of bone healing in rat calvarial defect models. *Journal of Biophotonics.* 13, 2020, Vol. 10.

119. **Ghita, A., Matousek, P. and Stone, N.** Exploring the effect of laser excitation wavelength on signal recovery with deep tissue transmission Raman spectroscopy. . *Analyst.* 141, 2016, Vol. 20.

120. **Grabtchak, S., Montgomery, L.G. and Whelan, W.M.,.** Optical absorption and scattering properties of bulk porcine muscle phantoms from interstitial radiance measurements in 650–900 nm range. *Physics in Medicine & Biology.* 59, 2014, Vol. 10.

121. **Andor.** iDus 420 series Spec Document.

122. **Griffen, J., Owen, A. and Matousek, P.** Comprehensive quantification of tablets with multiple active pharmaceutical ingredients using transmission Raman spectroscopy—A proof of concept study. *Journal of pharmaceutical and biomedical analysis.* 115, 20115.

123. **Vardaki, M.Z., Atkins, C.G., Schulze, H.G., Devine, D.V., Serrano, K., Blades, M.W. and Turner, R.F.B.,.** Raman spectroscopy of stored red blood cell concentrate within sealed transfusion blood bags. . *Analyst.* 143, 2018, Vol. 24.

124. **Dimitriou, R., Jones, E., McGonagle, D. and Giannoudis,.** Bone regeneration: current concepts and future directions. *BMC medicine,.* 9, 2011, Vol. 1.

125. **Stevens, M.M.** Biomaterials for bone tissue engineering. *Materials today.* 11, 2008, Vol. 5.

126. **Niemeyer, P., Fechner, K., Milz, S., Richter, W., Suedkamp, N.P., Mehlhorn, A.T., Pearce, S. and Kasten, P.** Comparison of mesenchymal stem cells from bone marrow and adipose tissue for bone regeneration in a critical size defect of the sheep tibia and the influence of platelet-rich plasma. *Biomaterials.* 31, 2010, Vol. 13.

127. **Bosch, C., Melsen, B. and Vargervik, K.** Importance of the critical-size bone defect in testing bone-regenerating materials. *The Journal of craniofacial surgery.* 9, 1998, Vol. 4.

128. **Caliaperoumal, G., Souyet, M., Bensidhoum, M., Petite, H. and Anagnostou, F.** Type 2 diabetes impairs angiogenesis and osteogenesis in calvarial defects:MicroCT study in ZDF rats. *Bone.* 112, 2018.

129. **Diab, T., Condon, K.W., Burr, D.B. and Vashishth, D.** Age-related change in the damage morphology of human cortical bone and its role in bone fragility. *Bone.* 38, 2006, Vol. 3.

130. **Karmakar, S., Kay, J. and Gravallese, E.M.** Bone damage in rheumatoid arthritis: mechanistic insights and approaches to prevention. *Rheumatic Disease Clinics.* 36, 2010, Vol. 2.

131. **Govender, S., Csimma, C., Genant, H.K., Valentin-Opran, A., Amit, Y., Arbel, R., Aro, H., Atar, D., Bishay, M., Börner, M.G. and Chiron, P.** Recombinant human bone morphogenetic protein-2 for treatment of open tibial fractures: a prospective, controlled, randomized study of four hundred and fifty patients. *JBJS.* 84, 2002, Vol. 12.

132. **Bouxsein, M.L., Boyd, S.K., Christiansen, B.A., Guldberg, R.E., Jepsen, K.J. and Müller, R.,.** Guidelines for assessment of bone microstructure in rodents using micro–computed tomography. *Journal of bone and mineral research,.* 25, 2010, Vol. 7.

133. **Stock, S.R., Blackburn, D., Gradassi, M. and Simon, H.G.** Bone formation during forelimb regeneration: a microtomography (microCT) analysis. . *evelopmental dynamics: an official publication of the American Association of Anatomists,.* 226, 2003, Vol. 2.

134. **Boerckel, J.D., Kolambkar, Y.M., Dupont, K.M., Uhrig, B.A., Phelps, E.A., Stevens, H.Y., García, A.J. and Guldberg, R.E.** Effects of protein dose and delivery system on BMP-mediated bone regeneration. . *Biomaterials.* 32, 2011, Vol. 22.

135. **Lienemann, P.S., Metzger, S., Kiveliö, A.S., Blanc, A., Papageorgiou, P., Astolfo, A., Pinzer, B.R., Cinelli, P., Weber, F.E., Schibli, R. and Béhé, M.,.** Longitudinal in vivo evaluation of bone regeneration by combined measurement of multi-pinhole SPECT and micro-CT for tissue engineering. *Scientific reports.* 5, 2015, Vol. 1.

136. *Raman spectroscopy: techniques and applications in the life sciences.* **Shipp D, Sinjab F,Notingher I.** 2017, Advances in Optics and Photonics, p. 315.

137. **Okagbare, P.I., Esmonde-White, F.W., Goldstein, S.A. and Morris, M.D.,.** Development of non-invasive Raman spectroscopy for in vivo evaluation of bone graft osseointegration in a rat model. . *Analyst.* 135, 2010, Vol. 12.

138. **Penel, G., Delfosse, C., Descamps, M. and Leroy, G.,.** Composition of bone and apatitic biomaterials as revealed by intravital Raman microspectroscopy. *Bone.* 36, 2005, Vol. 5.

139. *Noninvasive Raman spectroscopy of human tissue in vivo.* **Matousek, P., Draper, E.R., Goodship, A.E., Clark, I.P., Ronayne, K.L. and Parker, A.W.,.** 2006, Applied spectroscopy, pp. 758-763.

140. **Notingher, I., Jones, J.R., Verrier, S., Bisson, I., Embanga, P., Edwards, P., Polak, J.M. and Hench, L.L.** Application of FTIR and Raman spectroscopy to characterisation of bioactive materials and living cells. *Spectroscopy.* 17, 2003, Vol. 2.

141. **Palmer, L.C., Newcomb, C.J., Kaltz, S.R., Spoerke, E.D. and Stupp, S.I.,.** Biomimetic systems for hydroxyapatite mineralization inspired by bone and enamel. *Chemical reviews,.* 108, 2008, Vol. 11.

142. **Jo, S., Kang, S.M., Park, S.A., Kim, W.D., Kwak, J. and Lee, H.,.** Enhanced adhesion of preosteoblasts inside 3 D PCL scaffolds by polydopamine coating and mineralization. *Macromolecular bioscience.* 13, 2013, Vol. 10.

143. **Hartman, O., Zhang, C., Adams, E.L., Farach-Carson, M.C., Petrelli, N.J., Chase, B.D. and Rabolt, J.F.** Biofunctionalization of electrospun PCL-based scaffolds with perlecan domain IV peptide to create a 3-D pharmacokinetic cancer model. *Biomaterials.* 31, 2010.

144. **Notingher, I., Boccaccini, A.R., Jones, J., Maquet, V. and Hench, L.L.** Application of Raman microspectroscopy to the characterisation of bioactive materials. *Materials characterization.* 49, 2002, Vol. 3.

145. **Matousek, P., Clark, I.P., Draper, E.R., Morris, M.D., Goodship, A.E., Everall, N., Towrie, M., Finney, W.F. and Parker, A.W.** Subsurface probing in diffusely scattering media using spatially offset Raman spectroscopy. *Applied spectroscopy,.* 59, 2005, Vol. 4.

146. **Buckley, K., Kerns, J.G., Parker, A.W., Goodship, A.E. and Matousek, P.,.** Decomposition of in vivo spatially offset Raman spectroscopy data using multivariate analysis techniques. *Journal of Raman Spectroscopy.* 45, 2014, Vol. 2.

147. **Liao, Z., Sinjab, F., Nommeots-Nomm, A., Jones, J., Ruiz-Cantu, L., Yang, J., Rose, F. and Notingher, I.,.** Feasibility of spatially offset raman spectroscopy for in vitro and in vivo monitoring mineralization of bone tissue engineering scaffolds. *Analytical CHemistry.* 89, 2017, Vol. 1.

148. **Rizzi, S.C., Heath, D.J., Coombes, A.G.A., Bock, N., Textor, M. and Downes, S.** Biodegradable polymer/hydroxyapatite composites: surface analysis and initial attachment of human osteoblasts. *Journal of Biomedical Materials Research: An Official Journal of The Society for Biomaterials, The Japanese Society for Biomaterials, and The Australian Society for Biomaterials and the Korean Society for Biomaterials.* 55, 2001, Vol. 4.

149. **Aerssens, J., Boonen, S., Lowet, G. and Dequeker, J.** nterspecies differences in bone composition, density, and quality: potential implications for in vivo bone research. *Endocrinology.* 139, 1998, Vol. 2.

150. **Markides, H., McLaren, J.S., Telling, N.D., Alom, N., E'atelaf, A., Oreffo, R.O., Zannettino, A., Scammell, B.E., White, L.J. and El Haj, A.J., 2018.** Translation of remote control regenerative technologies for bone repair. *NPJ Regenerative medicine.* 3, 2018, Vol. 1.

151. **Larraona-Puy, M., Ghita, A., Zoladek, A.B., Perkins, W., Varma, S., Leach, I.H., Koloydenko, A., Williams, H. and Notingher, I.** Development of Raman microspectroscopy for automated detection and imaging of basal cell carcinoma. . *Journal of biomedical optics.* 14, 2009, Vol. 5.

152. **Kong, K., Rowlands, C.J., Varma, S., Perkins, W., Leach, I.H., Koloydenko, A.A., Williams, H.C. and Notingher, I.,.** Diagnosis of tumors during tissue-conserving surgery with integrated autofluorescence and Raman scattering microscopy. *Proceedings of the National Academy of Sciences.* 110, 2013, Vol. 38.

153. **Bansal, G. J.** Digital radiography. A comparison with modern conventional imaging. *Postgraduate medical journal.* 82.969, 2006.

154. **Rezwan, K., Chen, Q.Z., Blaker, J.J. and Boccaccini, A.R.** Biodegradable and bioactive porous polymer/inorganic composite scaffolds for bone tissue engineering. . *Biomaterials.* 27, 2006, Vol. 18.

155. **Umoh, J.U., Sampaio, A.V., Welch, I., Pitelka, V., Goldberg, H.A., Underhill, T.M. and Holdsworth, D.W.** In vivo micro-CT analysis of bone remodeling in a rat calvarial defect model. *Physics in Medicine & Biology.* 54, 2009, Vol. 7.

156. **Morris, M.D. and Mandair, G.S.** Raman assessment of bone quality. *Clinical Orthopaedics and Related Research.* 469, 2011, Vol. 8.

157. **Esmonde-White, K.** Raman spectroscopy of soft musculoskeletal tissues. *Applied spectroscopy.* 68, 2014, Vol. 11.

158. **Matousek, P. and Stone, N.,.** Recent advances in the development of Raman spectroscopy for deep non-invasive medical diagnosis. *Journal of biophotonics.* 6, 2013, Vol. 1.

159. **Sowoidnich, K., Churchwell, J.H., Buckley, K., Goodship, A.E., Parker, A.W. and Matousek, P.** Spatially offset Raman spectroscopy for photon migration studies in bones with different mineralization levels. . *Analyst.* 142, 2017, Vol. 17.

160. **Matousek, P. and Stone, N.,.** Development of deep subsurface Raman spectroscopy for medical diagnosis and disease monitoring. . *Chemical Society Reviews,.* 45, 2016, Vol. 7.

161. **Martin, R.B. and Boardman, D.L.** The effects of collagen fiber orientation, porosity, density, and mineralization on bovine cortical bone bending properties. *Journal of biomechanics.* 26, 1993, Vol. 9.

162. **CARTER, D.R. and Spengler, D.M.** Mechanical properties and composition of cortical bone. *Clinical Orthopaedics and Related Research.* 135, 1978.

163. **Kisiel, M., Klar, A.S., Martino, M.M., Ventura, M. and Hilborn, J.** Evaluation of injectable constructs for bone repair with a subperiosteal cranial model in the rat. *PLoS One.* 8, 2013, Vol. 8.

164. **Sinjab, F., Awuah, D., Gibson, G., Padgett, M., Ghaemmaghami, A.M. and Notingher, I.,.** Holographic optical trapping Raman micro-spectroscopy for non-invasive measurement and manipulation of live cells. *Optics express.* 26, 2018, Vol. 19.

165. **Ghiasi, M.S., Chen, J., Vaziri, A., Rodriguez, E.K. and Nazarian, A.,.** Bone fracture healing in mechanobiological modeling: A review of principles and methods. *Bone Report.* 6, 2017.

166. **Demers, J.L.H., Davis, S.C., Pogue, B.W. and Morris, M.D.,.** Multichannel diffuse optical Raman tomography for bone characterization in vivo: a phantom study. . *Biomedical optics express.* 3, 2012, Vol. 9.

167. **Movasaghi, Z., Rehman, S. and Rehman, I.U., 2007.** Raman spectroscopy of biological tissues. *Applied Spectroscopy Reviews,.* 42, 2007, Vol. 5.

168. **Dehghani, H., Eames, M.E., Yalavarthy, P.K., Davis, S.C., Srinivasan, S., Carpenter, C.M., Pogue, B.W. and Paulsen, K.D.,.** Near infrared optical tomography using NIRFAST: Algorithm for numerical model and image reconstruction. . *Communications.* 2009. .

169. *In VivoMicroCT Monitoring of Osteomyelitis in a Rat Model.* **Vincent A. Stadelmann, Inga Potapova, Karin Camenisch, Dirk Nehrbass,R. Geoff Richards, and T. Fintan Moriarty.** s.l. : BioMed Research International, 2014, Vol. 2015.

170. *Costs, charges, and revenues for hospital diagnostic imaging procedures: differences by modality and hospital characteristics.* **Sistrom, C.L. and McKay, N.L.** 6, s.l. : Journal of the American College of Radiology, , 2005, Vol. 2.

171. *Costing in radiology and health care: rationale, relativity, rudiments, and realities.* **Rubin, G.D.** 2, s.l. : Radiology, 2017, Vol. 282.

172. **Mahadevan-Jansen, A., Keller, M.D. and Kelley, M.C.,.** *Spatially offset raman spectroscopy of layered soft tissues and applications of same. 9289130 B2* US, 22 March 2016.

173. *Raman spectroscopy and electronic microscopy structural studies of Caucasian and Afro human hair.* **Dias, Jordana and Edwards, Howell and De Oliveira, Luiz Fernando.**

174. **Boerckel, J.D., Kolambkar, Y.M., Dupont, K.M., Uhrig, B.A., Phelps, E.A., Stevens, H.Y., García, A.J. and Guldberg, R.E.,.** Effects of protein dose and delivery system on BMP-mediated bone regeneration. . *Biomaterials.* 32, 2011, Vol. 22.

175. **instuments, Texas.** DLP6500 0.65 1080p MVSP Type A DMD. s.l. : ti.com, OCtober 2014.

176. **Instuments, Texas.** DLP4500NIR .45 WXGA Near-Infrared DMD. s.l. : Texas Instuments, 2019.

177. *Surface enhanced spatially offset Raman spectroscopic (SESORS) imaging–the next dimension.* **Stone, N., Kerssens, M., Lloyd, G.R., Faulds, K., Graham, D. and Matousek, P.** 4, 2011, Chemical Science, Vol. 2, pp. 776-780.

8   Table of Figures